Potential reference sites for MSA validation in Africa, Southern Europe, and the Middle East. Green: MSA fulfils GCOS requirements at least partly. Red: GCOS requirements are not met. Grey: No MSA data available for analysis. See section 5.4 for more detail.

Validation of the
EUMETSAT
Geostationary Surface Albedo
Climate Data Record -2-

(ALBEDOVAL-2)

Final

report

Berlin, 2 October 2015

Validation of the EUMETSAT Geostationary Surface Albedo

Climate Data Record -2-

(ALBEDOVAL-2)

Final report

Document control sheet	
Project	Validation of the EUMETSAT Geostationary Surface Albedo Climate Data Record -2- (ALBEDOVAL-2)
Client	EUMETSAT Eumetsat Allee 1 64295 Darmstadt http://www.eumetsat.int
Main contractor	Informus GmbH Belziger Str. 44 10823 Berlin, Germany http://www.informus.de
Title	Final report
Pages	109
Status	Released
Authors	Frank Fell, Ralf Bennartz, Alexander Loew
Distribution	ALBEDOVAL-2 consortium, EUMETSAT Report and GSA Validation Database are available from ops@eumetsat.int
Version control	2015-08-10 1.0: Initial version 2015-10-02 1.1: EUMETSATs comments on initial version considered
URLs	All URLs in this report have been successfully tested on 2015-09-30

List of acronyms

Acronym	Explanation
0DEG	MVIRI 0 degree observation geometry
AERONET	AErosol RObotic NETwork
AOD	Aerosol optical depth
ASDC	Atmospheric Science Data Center
ASTER	Advanced Spaceborne Thermal Emission and Reflection Radiometer
ASTM	American Society for Testing and Materials
AVHRR	Advanced Very High Resolution Radiometer
BELMANIP	BEnchmark Land Multisite ANalysis and Intercomparison of Products
BHR	Bi-hemispherical reflectance
BRDF	Bi-directional reflectance distribution function
BRF	Bi-directional reflectance factor
BSA	Black sky albedo
BSRN	Baseline Surface Radiation Network
CCI	Climate Change Inititive (ESA)
CDR	Climate data record
DHR	Directional hemispherical reflectance
ESA	European Space Agency
EUMETSAT	European Organisation for the Use of Meteorological Satellites
FAO	Food and Agriculture Organization of the United Nations
GCOS	Global Climate Observing System
GLASS	Global Land Surface Satellite
GMS	Geostationary Meteorological Satellite (Japan)
GOES	Geostationary Operational Environmental Satellite (US)
GSA	Geostationary Surface Albedo
GSAVALDB	GSA Validation Database
HDRF	Hemispherical-directional reflectance factor
IMS	Interactive Multisensor Snow and Ice Mapping System
IODC	Indian Ocean data coverage
JMA	Japan Meteorological Agency
JSON	JavaScript Object Notation
LAGS	Land surface albedo from geostationary satellites
LC	Land cover
LTER	Long Term Ecological Research Network
LUT	Look-up table
MFG	Meteosat First Generation
MISR	The Multi-angle Imaging SpectroRadiometer
MODIS	Moderate Resolution Imaging Spectroradiometer
MSA	Meteosat Surface Albedo
MTSAT	Multifunctional Transport Satellites

Acronym	Explanation
MVIRI	Meteosat Visible and Infra-Red Imager
NCDC	National Climatic Data Center
NDVI	Normalised difference vegetation index
NOAA	National Oceanic and Atmospheric Administration
OE	Optimal estimation
OLIVE	On Line Interactive Validation Exercise
OPAC	Optical Properties of Aerosols and Clouds
RPV	Rahman-Pinty-Verstraete (surface BRF model)
SAF	Satellite Applications Facility
SCOPE-CM	Sustained, Co-Ordinated Processing of Environmental Satellite Data for Climate Monitoring
SPOT	Satellite pour l'Observation de la Terre
SSP	Sub-satellite point
SWIR	Shortwave infrared (part of the spectrum)
TOA	Top of atmosphere
VIS	Visible (part of the spectrum)
WSA	White sky albedo
WMO	World Meteorological Organization

Executive summary

A first independent evaluation of the Meteosat Surface Albedo (MSA) took place in 2011 and 2012 through the ALBEDOVAL-1 project and provided the following main results:

➢ *Unidentified clouds constitute the main challenge to MSA overall quality as they may regionally lead to systematic errors in absolute values and trends of the retrieved surface albedo.*

➢ *Further quality issues arise from anisotropy effects and MSA's inability to provide information over bright snow covered areas.*

➢ *Nevertheless, MSA shows good temporal stability meeting the requirements of the Global Climate Observing System (GCOS) for a number of investigated desert sites.*

➢ *Due to its independence from many other surface albedo retrieval approaches and its ability to provide quasi-global albedo values over several decades, MSA is considered a potentially highly valuable climate data record and measures were recommended to improve its quality.*

A follow-on project, ALBEDOVAL-2, was set up in 2014 to deepen the understanding of the MSA performance. It is based on further examination of MSA products at selected reference sites meeting strict homogeneity requirements. ALBEDOVAL-2 yielded the following main results:

➢ *An online database of surface reference areas has been established, covering more than 2000 sites worldwide. Statistical parameters have been produced for each site, including homogeneity measures and land cover information, allowing to select site subsets for specific analyses.*

➢ *Cloud contamination has been confirmed as being the major challenge to MSA quality. Efforts are already under way to address this issue and improvements are expected with a future MSA release [Lattanzio et al., 2015].*

➢ *An assessment of the MSA-retrieved anisotropy characterisation has been performed for selected surface sites. Cross talk between the retrieved anisotropy parameters has been observed, directly affecting the derived black- and white-sky surface albedos.*

➢ *Bright snow covered surfaces are currently filtered out by MSA cloud screening leading to significant gaps in MSA temporal coverage over large areas in the northern hemisphere. This in turn may induce systematic errors when e.g. calculating annual albedo averages.*

➢ *Snow covered surfaces require a specific spectral-to-broadband conversion as their spectral reflectance differs significantly from that of other land surfaces types, leading to significant overestimation when applying standard conversion factors [Loew and Govaerts, 2010].*

➢ *The long-term temporal stability of MSA has been analysed for different surface conditions and a number of sites matching the respective GCOS criteria have been identified.*

➢ *A comparison with the AVHRR-based GLASS surface albedo has been performed for the pre-MODIS era prior to the year 2000, often showing good agreement for robust statistical parameters little affected by cloud contamination.*

Table of contents

List of tables

List of figures

1. **Introduction**

1.1 **Thematic context**

Observations from geostationary satellites allow for the retrieval of surface albedo information that complements surface albedo retrievals from polar orbiting instruments. The main advantage of geostationary observations consists in the high temporal resolution, which increases the likelihood for observations under cloud-free observation conditions. In addition, geostationary observations cover over long periods (e.g. Meteosat observations are available since 1982), which makes them important information sources for climate studies.

The *Geostationary Surface Albedo* (GSA) algorithm retrieves surface albedo in a single broad visible band from observations acquired by instruments on board geostationary satellites *[Pinty et al., 2000-A]*. It relies on a sophisticated algorithm for the retrieval of surface albedo and aerosol load accounting for the anisotropy of the surface based on daily accumulation of VIS band data and fast cloud detection method *[Pinty et al., 2000-B]*.

The GSA algorithm has been applied to the visible (VIS) channel of the *Meteosat Visible and InfraRed Imager* (MVIRI) *[Lattanzio et al., 2006]* to provide the EUMETSAT *Meteosat Surface Albedo* (MSA). This includes a method for the estimation of the radiometric error and the propagation of this error in the retrieval scheme that specifically accounts for the differences in the performance of the various radiometers on board the Meteosat series *[Govaerts and Lattanzio, 2007]*. In the following, the term GSA is used when referring to general aspects of the method, while the term MSA is applied when analysing data products.

A first independent evaluation of the MSA product took place in 2011 and 2012 through the ALBEDOVAL-1 project, which provided the following main results:

➢ Unidentified clouds constitute the main challenge to MSA overall quality as this may regionally lead to systematic errors in both absolute values and trends of the retrieved surface albedo.

➢ Further quality issues arise from anisotropy effects and MSA's inability to provide information over bright snow covered areas.

➢ Nevertheless, MSA shows good temporal stability meeting the requirements of the *Global Climate Observing System* (GCOS) for a number of investigated desert sites.

➢ Due to its independence from many other surface albedo retrieval approaches and its ability to provide quasi-global albedo values over several decades, MSA was rated as a potentially highly valuable climate data record and measures were recommended to improve its quality.

More details on the outcome of the ALBEDOVAL-1 activities as well as the recommendations provided to increase value and usability of MSA for potential users can be found in *Fell et al. [2012]*.

A follow-on project, ALBEDOVAL-2, was set up in 2014 to further elaborate on a number of important aspects that were not or not sufficiently covered in ALBEDOVAL-1 and to such deepen the understanding of the MSA performance.

Within the new SCOPE-CM (*Sustained, Co-Ordinated Processing of Environmental Satellite Data for Climate Monitoring*) project LAGS (*Land surface albedo from geostationary satellites*)[1], EUMETSAT leads the further development and implementation of the GSA algorithm for NOAA-NCDC's *Geostationary Environmental Satellite System* (GOES), as well as for JMA's *Geostationary Meteorological Satellites* (GMS) and *Multifunctional Transport Satellites* (MTSAT). Where applicable, the analyses performed in the context of ALBEDOVAL-2 therefore comprise the whole GeoRing, by which we mean an ensemble of geostationary satellites covering the globe almost entirely between 60°N and 60°S.
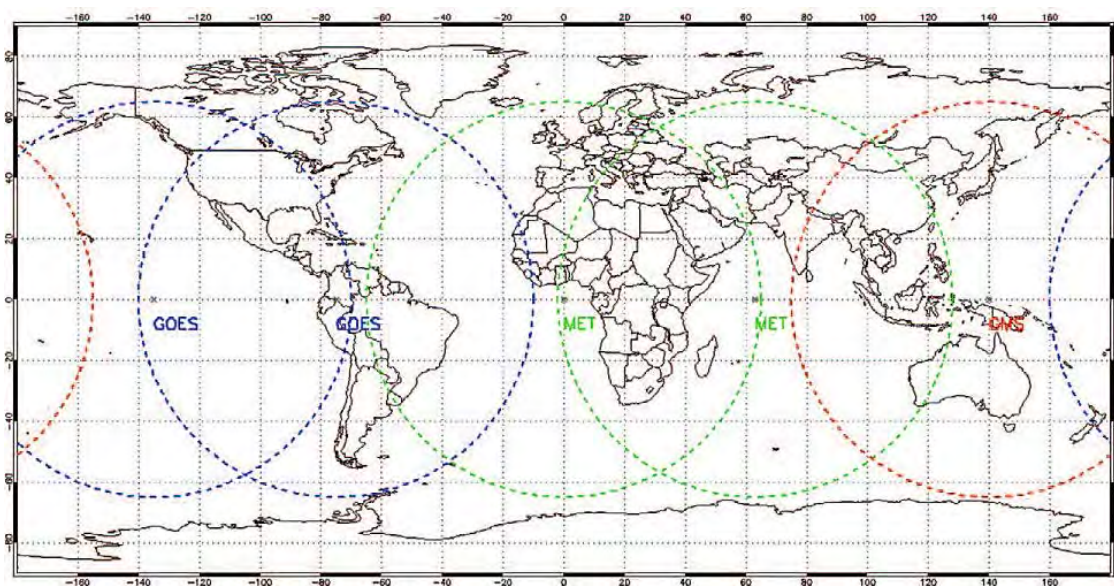
Figure 1: Candidate geostationary satellites for applying the GSA algorithm. From west to east: GOES-10 (west), GOES-8 (east), Meteosat-7, Meteosat-5 (IODC), and GMS-5 *[Lattanzio et al., 2013]*.

1.2   Aims and objectives

The main aims of the ALBEDOVAL-2 project were to

- ➢ identify and characterise reference sites to support GSA analyses worldwide,
- ➢ assess the impact of surface anisotropy on MSA performance,
- ➢ assess the performance of MSA above snow covered surfaces,
- ➢ further analyse the MSA long-term stability for different surface conditions.

Each aim was addressed by individual task(s) addressed in this report through dedicated sections. Based on the findings, a number of recommendations have been devised for the generation of a re-processed MSA dataset.

---

[1] http://www.scope-cm.org/projects/scm-03/

1.3   Document structure

This report documents the outcome of the ALBDOVAL-2 activities. We herein do not provide the theoretical foundations of surface albedo retrieval or a description of the MSA product. Those can be found in the MSA Algorithm Theoretical Basis Document *[EUMETSAT, 2014-A]* and the references provided therein.

Intentionally left blank

2. Identification of GSA reference sites (Task 1)

2.1 Expected outcome

The expected outcome [of Task 1] is the definition of criteria for reference target selection and a catalogue of surface reference targets for all geostationary satellite platforms, including target characterisation and application areas.

2.2 Method

To be useful for surface albedo validation, a site needs to fulfil different requirements. First, the site should be representative of a larger area, thus the spatial heterogeneity of the site should be small within the minimum mapping unit of a particular data product or observing instrument. Second, reference albedo measurements should be available with quantified representativeness *[Roman et al., 2009]*. Such surface albedo measurements are available only for a limited number of sites over the globe. However, spatially representative sites which are known to show a stable albedo signal over time can be also very useful to characterize the long-term temporal stability of a dataset.

The following approach was therefore implemented:

1. Identify potential validation sites based on existing network infrastructures.

2. Characterize the spatial homogeneity of these sites using ancillary information.

3. Define criteria for GSA validation sites.

4. Select sites with potential GSA validation capabilities.

Mainly two studies have been devoted so far to the identification of spatially homogenous sites specifically for the evaluation of satellite surface albedo observations. *Baret et al. [2006]* identified homogeneous sites from available in situ measurement networks for the validation of surface albedo data. These sites are referred to as BELMANIP (*BEnchmark Land Multisite ANalysis and Intercomparison of Products*) sites. The BELMANIP sites have been supplemented by homogeneous reference sites which were identified using the ESA GlobCover[2] dataset. This combined dataset (BELMANIP-2) is used in the CEOS Cal/Val OLIVE (*On Line Interactive Validation Exercise*) tool which was developed to provide a framework for validating satellite products of terrestrial variables.

There exist a number of operational terrestrial measurement networks to monitor a variety of climatologically relevant variables (energy budgets, carbon fluxes, atmospheric aerosols, …) and their individual sites have often been considered to be representative of a larger surrounding area. However, none of the existing networks has been tailored for the evaluation of the geostationary surface albedo. They rather allow for the evaluation of products from polar orbiting sensors with

---

2

spatial resolutions better than 1 km² as well as lower variability in the instantaneous field of view and diurnal cycle as compared to geostationary sensors.
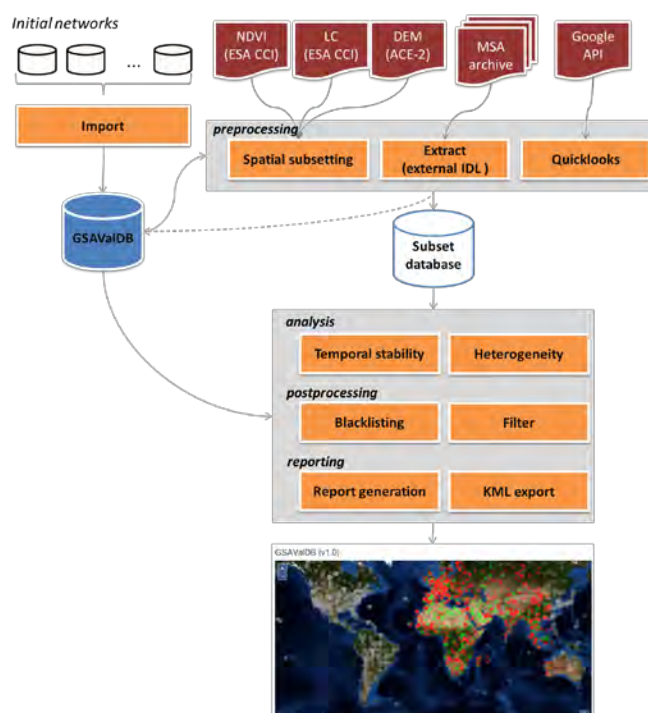
Figure 2: General workflow to identify potential GSA validation reference sites, characterize them using MSA data and ancillary information, and report final results.

The evaluation of the GSA needs to consider additional factors, which are unique to geostationary observations. These include:

- ➢ generally lower geometric resolution,
- ➢ varying geometric resolution for different biomes,
- ➢ variations in the diurnal cycle and their effect on terrain induced shadowing,
- ➢ geometric uncertainties due to navigation uncertainties,
- ➢ anisotropic effects due to diurnal cycles.

This leads to stringent requirements on a number of characteristics to make a reference site suitable for GSA evaluation:

- ➢ *Spatial homogeneity:* Due to the generally coarser spatial resolution of geostationary instruments with additional navigation uncertainties, the spatial homogeneity of the reference site is important. It can be quantified by a number of proxies, derived e.g. from vegetation and land cover information.

- ➢ *Topographic homogeneity:* Topography can have a substantial effect (e.g. shadowing) on the diurnal measurements of surface reflected directional radiances, which are the basic input into the generation of the GSA product.

> ➢ In an optimum case, the set of reference sites would also both cover the range of possible albedo values (meaning that dark as well as bright reference sites are available) and cover over a range of different biomes, taking into account different vegetation phenology.

The overall workflow of generating the *GSA Validation Database* (GSAVALDB) and usage of ancillary information for the characterization of identified potential reference sites is illustrated in Figure 2.

2.3 Data

2.3.1 Potential reference sites

In order to identify potential reference sites, terrestrial measurement networks were analysed (Table 1). This first set of potential reference sites was then screened to identify gaps in terms of geographical location, biome coverage, albedo values, or lack of sites with a potential to gain insight into specific GSA issues. Additional 48 sites were subsequently identified (the ALBEDOVAL-2 network) by expert knowledge to fill the gaps, resulting in a total of 2220 potential reference sites worldwide.

Table 1: Terrestrial reference networks considered within ALBEDOVAL-2.

Network	Reference / Remark	# of sites
FLUXNET	http://fluxnet.ornl.gov/	252
BSRN	http://www.bsrn.awi.de/	63
AERONET	http://aeronet.gsfc.nasa.gov/	1176
BELMANIP-2	http://calvalportal.ceos.org/web/olive/site-description	558
CEOS LandNet sites	http://calvalportal.ceos.org/ceos-landnet-sites	8
EOS core sites	http://landval.gsfc.nasa.gov/coresite_gen.html	41
Surfrad	http://www.esrl.noaa.gov/gmd/grad/surfrad/index.html	7
LTER	http://lternet.edu/	27
ALBEDOVAL-1	Incl. SAFARI2000, http://daac.ornl.gov/S2K/safari.shtml	40
ALBEDOVAL-2	Further sites identified by expert knowledge	48
Total		**2220**
Total final	After removal of duplicates	**2186**

Some sites are part of several networks; these duplicates were removed, resulting in a total of 2186 sites in the GSA validation site raw database graphically represented in Figure 3. For some stations (e.g. MONGU) duplicates where identified, but they differed largely in the coordinates provided. It was not clear whether these sites correspond to different locations or if there are inconsistencies in the specified coordinates. In such cases, the duplicates remained in the database and were given unique keys (e.g. MONGU, MONGU1, MONGU2).

2.3.2 Elevation data

Topographic information is based on the ACE-2[3] digital elevation model, providing global elevation data at a resolution of three arc seconds (~90 m).

---

[3] http://tethys.eaprs.cse.dmu.ac.uk/ACE2/

Validation sites: $N=2186$
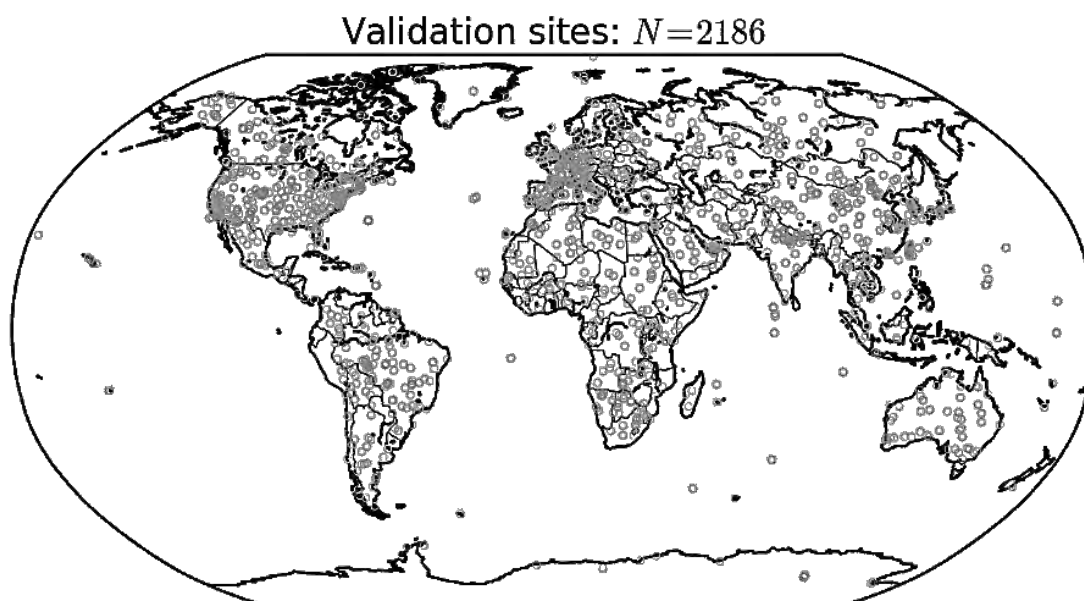
Figure 3: Potential albedo validation sites identified from the networks summarized in Table 1. Selected sites are shown in Figure 11.

2.3.3 Land cover data

High resolution (300 m) land cover information was obtained from the ESA *Climate Change Initiative* (ESA CCI) Land Cover project[4], providing global coverage for 22 land cover classes which are partly refined into further subclasses (Figure 4).

Value	Label	Color
0	No Data	
10	Cropland, rainfed	
11	Herbaceous cover	
12	Tree or shrub cover	
20	Cropland, irrigated or post-flooding	
30	Mosaic cropland (>50%) / natural vegetation (tree, shrub, herbaceous	
40	Mosaic natural vegetation (tree, shrub, herbaceous cover) (>50%) /	
50	Tree cover, broadleaved, evergreen, closed to open (>15%)	
60	Tree cover, broadleaved, deciduous, closed to open (>15%)	
61	Tree cover, broadleaved, deciduous, closed (>40%)	
62	Tree cover, broadleaved, deciduous, open (15-40%)	
70	Tree cover, needleleaved, evergreen, closed to open (>15%)	
71	Tree cover, needleleaved, evergreen, closed (>40%)	
72	Tree cover, needleleaved, evergreen, open (15-40%)	
80	Tree cover, needleleaved, deciduous, closed to open (>15%)	
81	Tree cover, needleleaved, deciduous, closed (>40%)	
82	Tree cover, needleleaved, deciduous, open (15-40%)	
90	Tree cover, mixed leaf type (broadleaved and needleleaved)	

Value	Label	Color
100	Mosaic tree and shrub (>50%) / herbaceous cover (<50%)	
110	Mosaic herbaceous cover (>50%) / tree and shrub (<50%)	
120	Shrubland	
121	Evergreen shrubland	
122	Deciduous shrubland	
130	Grassland	
140	Lichens and mosses	
150	Sparse vegetation (tree, shrub, herbaceous cover) (<15%)	
152	Sparse shrub (<15%)	
153	Sparse herbaceous cover (<15%)	
160	Tree cover, flooded, fresh or brakish water	
170	Tree cover, flooded, saline water	
180	Shrub or herbaceous cover, flooded, fresh/saline/brakish water	
190	Urban areas	
200	Bare areas	
201	Consolidated bare areas	
202	Unconsolidated bare areas	
210	Water bodies	
220	Permanent snow and ice	

Figure 4: Legend of the CCI LC maps, based on the FAO Land Cover Classification System[5] (LCCS). Source: http://maps.elie.ucl.ac.be/CCI/viewer/download/CCI-LC_Maps_Legend.pdf.

2.3.4 Vegetation, snow and fire dynamics

The ESA CCI Land Cover dataset provides ancillary information on vegetation, snow and fire dynamics:

---

[4] http://www.esa-landcover-cci.org/

[5] http://www.fao.org/docrep/003/x0596e/x0596e00.HTM

- The *Normalized Difference Vegetation Index* (NDVI) is a good proxy for the abundance and seasonality of vegetation.

  o The CCI land cover dataset provides information on the mean seasonality of the NDVI with a temporal resolution of eight days at pixel level, derived from SPOT VEGETATION[6] data for the period 1998 – 2012.

  o Maps of minimum and maximum NDVI were calculated from these data and NDVI subsets were extracted around each site, similar to the land cover data.

- In addition, the ESA CCI data provides information on the snow and fire seasonality at pixel level. The probability for snow and fire occurrence is provided for 8-day periods.

2.4 Characterization of surface sites

2.4.1 Topographic homogeneity

The topographic height z of an area of approx. 50×50 km² surrounding each site was extracted from the ACE-2 dataset for further analysis. An example is shown in Figure 5 (top) for the site BLACK_FOREST_AMF. Statistical topographic parameters were then calculated for circular areas around the centre coordinate with radii of 1 km , 2 km, 5 km, 10 km, and 20 km to characterize its vertical and horizontal homogeneity. Given an area $A(r)$, defined by the radius r, and the number of pixels with that area $N(r)$, the following topographic parameters were estimated:

$$Mean\ height\ [m]:\ \bar{z}(r) = \frac{1}{N(r)} \sum_{i=1}^{N(r)} z_i \tag{1}$$

$$Height\ standard\ deviation\ [m]:\ \sigma(r) = \sqrt{\frac{1}{N(r)-1} \sum_{i=1}^{N(r)} (z_i - \bar{z})^2} \tag{2}$$

$$Height\ range\ [m]:\ \Delta z(r) = P_{95}\big(A(r)\big) - P_{05}\big(A(r)\big) \tag{3}$$

$$Omnidirectional\ semivariogram\ of\ elevation:\ \gamma(h) = \frac{1}{2} \frac{1}{N(h)} \sum_{i=1}^{N(h)} \big(z(x_i + h) - z(x_i)\big)^2 \tag{4}$$

The height range Δz is estimated herein as the difference between the 95% and 5% percentiles of the heights within area A. The omnidirectional semi-variogram describes the degree of spatial dependence of a parameter. It is calculated here assuming an isotropic height field.

---

[6] http://www.spot-vegetation.cm/index.html
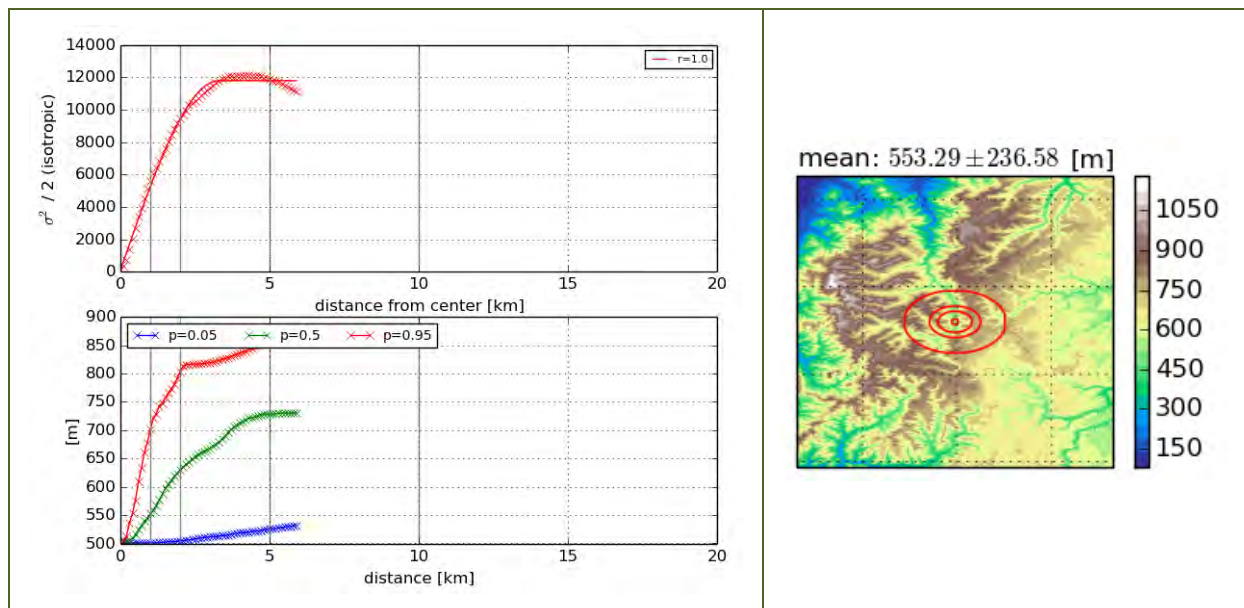
Figure 5: Topographic characterization at the example of site BLACK_FOREST_AMF. Right: topography around the site location; upper left: semi-variance for different lags, where r is the correlation coefficient between the empirical semi-variogram and a theoretical model; lower left: 5%, 50% and 95% percentiles of height values at different lags, indicating height range.

2.4.2 Land cover homogeneity

For each site, the ESA CCI land cover information was extracted for the same area (50×50 km²) as used for the topographic homogeneity analysis (Figure 6).
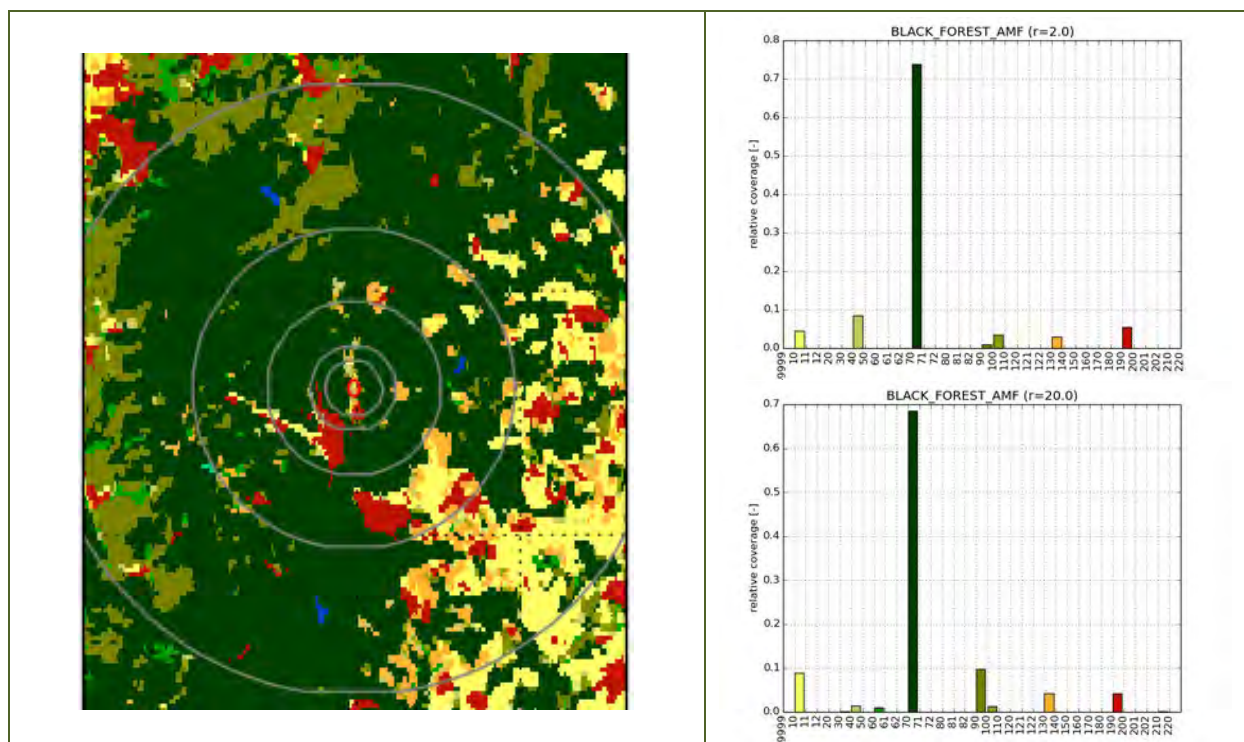
Figure 6: Land cover (left) map for site BLACK_FOREST_AMF and derived statistics within radii of 2 km (right, top) and 20 km (right, bottom), See Figure 4 for the definition of the land cover labels.

The following parameters were calculated:

- ➢ Fractions of land cover classes within distances of 1 km, 2 km, 5 km, 10 km, and 20 km from the centre coordinate,

- ➢ Dominant land cover type within the same distances,

- ➢ Distance to closest urban area [km],

Distance to open water bodies [km].

2.4.3 Vegetation homogeneity

The NDVI is a good proxy for the abundance and seasonality of vegetation. Suitable GSA validation sites would be rather stable in time, thus showing a low seasonality of vegetation, and would also show a small horizontal variability of vegetation density.

The NDVI-related spatial homogeneity was characterized using the following parameters (Figure 7):

- ➢ Range between the 5% and 95% percentiles of the NDVI minimum (NDVI_MIN) derived from the CCI Land Cover mean NDVI seasonality (see section 2.3.4) at distances of 1 km, 2 km, 5 km, 10 km, and 20 km,

- ➢ Same as before, but for the maximum of the NDVI (NDVI_MAX),

- ➢ Slope and intercept of a linear regression on the semi-variogram at scales of 2 km and 5 km as a proxy for the change of the variogram with increasing distance.
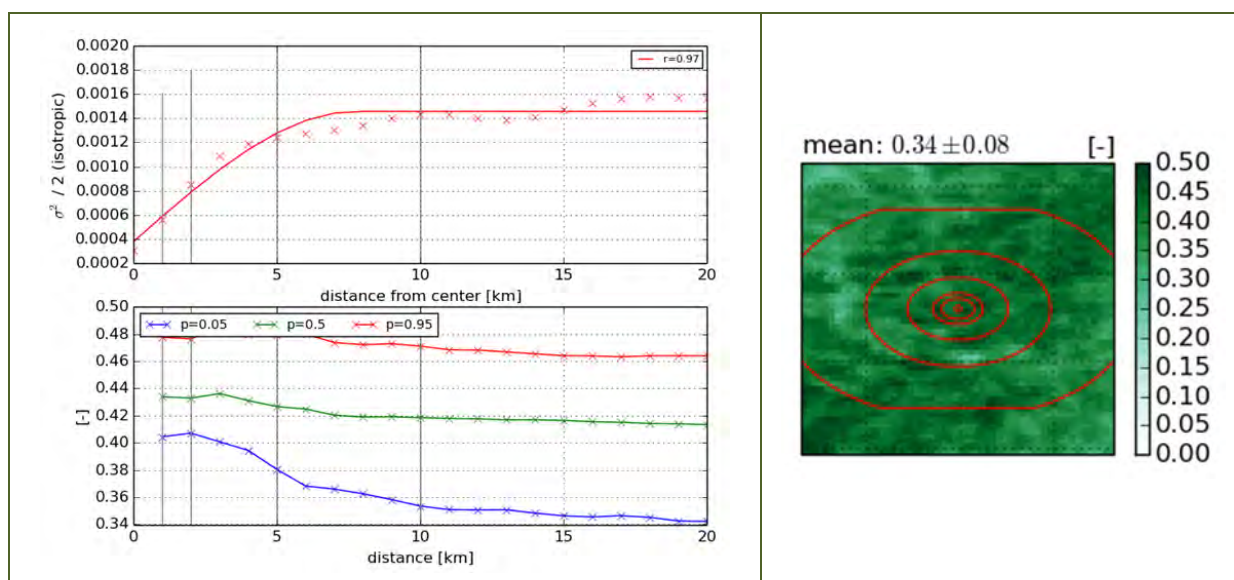
Figure 7: NDVI_MIN subset for site BLACK_FOREST_AMF and estimated statistical parameters.

2.4.4 Disturbances

Snow cover as well as disturbances like fire render the validation of surface albedo data products more difficult. The GSA Validation Database therefore contains also information on the probability of snow and fire occurrence. This information was derived from the land cover condition information of the ESA CCI land cover product.

The following disturbance parameters were derived for each site:

> *Snow affected (true/false)*: True in the case that snow occurs at least once at any time during the year.

> *Snow probability*: Likelihood of snow occurrence within eight day periods derived from a multi-annual analysis as $P_{snow}(t) = \frac{\sum_{i=1}^{N} has\ snow(t)}{N}$, where N is the number of years (Figure 8).

> *Fire affected (true/false)*: True in the case that fire occurs at least once at any time during the year.

> *Fire probability*: Likelihood of fire occurrence within eight day periods derived from a multiannual analysis as $P_{fire}(t) = \frac{\sum_{i=1}^{N} has\ fire(t)}{N}$, where N is the number of years. The image for fire looks similar to Figure 8. As fires do not occur for the BLACK_FOREST_AMF site, no example is given.
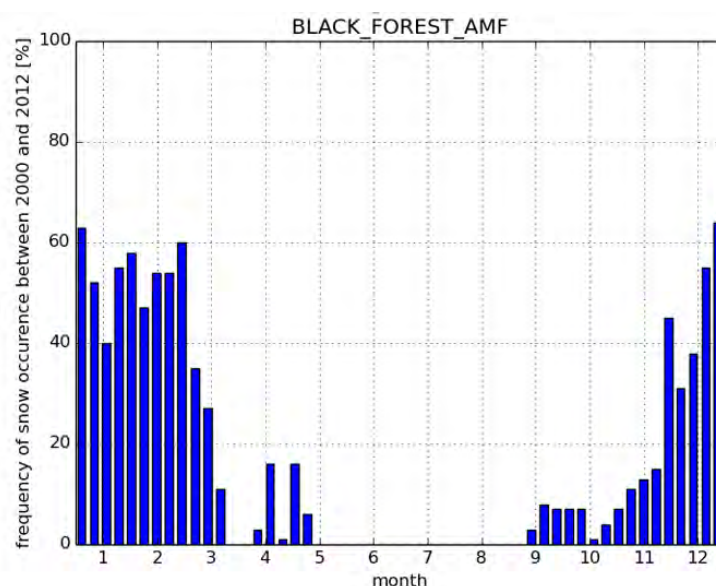
Figure 8: Example of frequency of snow occurrence for site BLACK_FOREST_AMF.

2.5   Results

2.5.1   Criteria for pre-selection of reference sites

To pre-select sites with a potential for GSA validation, the criteria defined in section 2.4 were applied, using the thresholds specified and motivated in Table 2.

Table 2: Criteria for identifying potential reference sites in the GSA Validation Database.

Parameter	Threshold	Purpose
Latitude	ABS (lat) < 60°	Ensure coverage within geostationary domain.
Blacklisted	False	Do not consider "blacklisted" stations.
Land cover		

Parameter	Threshold	Purpose
Distance to open water bodies [km]	10	Avoid open water bodies and their changing reflectance behaviour with viewing geometry.
Distance to urban areas [km]	Not applied yet	Avoid urban areas with their highly varying surface albedo and likely larger aerosol optical depth.[7]
Minimum fraction of majority land cover type at 2 <u>and</u> 20 km distance	70%	Avoid areas with heterogeneous land cover.
Topography		
Vertical range [m] within a distance of 2 km	< 100 m	Avoid areas with significant terrain variability close to a site.
NDVI		
NDVI (p95, 5 km) – NDVI (p05, 5 km) < x (see Figure 7, bottom).	x = 0.1	Avoid areas with highly variable NDVI within a radius of 5km from a site. Applied to NDVI_MAX and NDVI_MIN.

2.5.2 GSA Validation Database (GSAVALDB)

The GSA Validation Database comprises all identified potential reference sites (see section 2.3.1). Version 1.0 of the database comprises a total of 2186 sites (see Figure 3). Each site is characterized by a unique identifier. The database itself is provided in two simple text based formats, which can be easily processed[8].

JavaScript Object Notation (JSON):
JSON *[ECMA, 2013]* allows for storage of hierarchical data on any type in a simple text format. JSON is a text format that is completely language independent but uses familiar programming conventions. It can easily parsed by libraries available in different programming languages (http://www.json.org). These properties make JSON an ideal data-interchange language. An example is given in Figure 9.

```
{
    "DIRECT_78": {
        "files": {
            "directory": "../data/msa_subsets/",
            "gsa_subset_000": "000/DIRECT_78.000deg.sav",
            "gimms_subset": null,
            "gsa_subset_iodc": "iodc/DIRECT_78.057_or_063deg.sav"
        },
        "GSA_cover": {
            "0DEG": false,
            "DEG0_zenith_angle": -99999.0,
            "IODC_zenith_angle": 74.71507510802662,
            "IODC": true
        },
        "topography": {
```
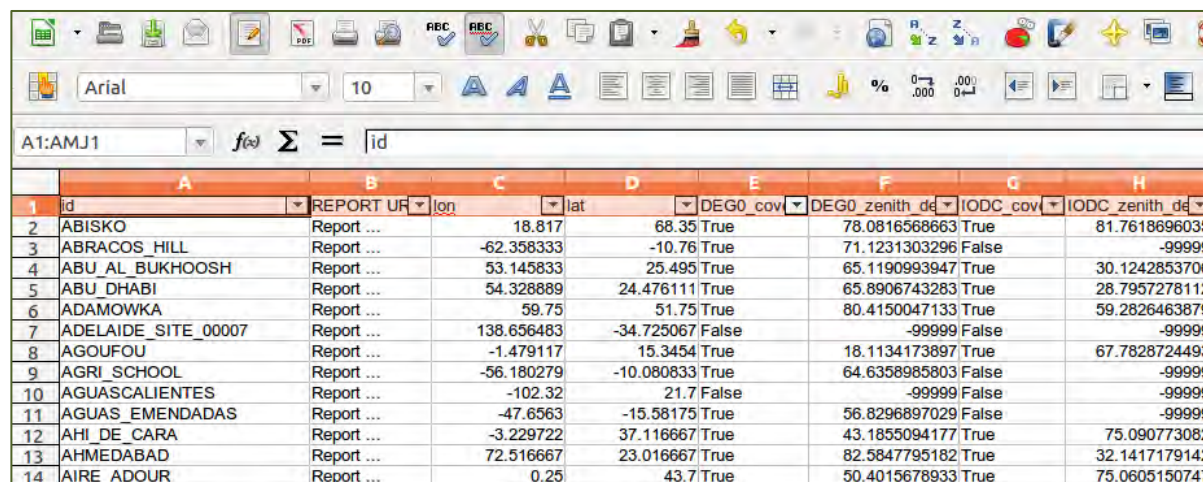
Figure 9: Example of the GSA Validation Database in JSON format.

---

[7] However, large urban areas might serve as albedo reference site due to their temporal stability. The criterion is therefore currently not used.

[8] Please contact EUMETSAT at ops@eumetsat.int to get access to the GSAVALDB.

Character Separated Value (CSV):

CSV is used as an additional output to facilitate direct import into spreadsheet or other analysis software. The individual data fields are stored using TAB separation (Figure 10).

	A	B	C	D	E	F	G	H
1	id	REPORT UR	lon	lat	DEG0_cov	DEG0_zenith_de	IODC_cov	IODC_zenith_de
2	ABISKO	Report ...	18.817	68.35	True	78.0816568663	True	81.7618696035
3	ABRACOS_HILL	Report ...	-62.358333	-10.76	True	71.1231303296	False	-99999
4	ABU_AL_BUKHOOSH	Report ...	53.145833	25.495	True	65.1190993947	True	30.1242853706
5	ABU_DHABI	Report ...	54.328889	24.476111	True	65.8906743283	True	28.7957278112
6	ADAMOWKA	Report ...	59.75	51.75	True	80.4150047133	True	59.2826463879
7	ADELAIDE_SITE_00007	Report ...	138.656483	-34.725067	False	-99999	False	-99999
8	AGOUFOU	Report ...	-1.479117	15.3454	True	18.1134173897	True	67.7828724493
9	AGRI_SCHOOL	Report ...	-56.180279	-10.080833	True	64.6358985803	False	-99999
10	AGUASCALIENTES	Report ...	-102.32	21.7	False	-99999	False	-99999
11	AGUAS_EMENDADAS	Report ...	-47.6563	-15.58175	True	56.8296897029	False	-99999
12	AHI_DE_CARA	Report ...	-3.229722	37.116667	True	43.1855094177	True	75.090773082
13	AHMEDABAD	Report ...	72.516667	23.016667	True	82.5847795182	True	32.1417179142
14	AIRE_ADOUR	Report ...	0.25	43.7	True	50.4015678933	True	75.0605150747

Figure 10: Example of GSA Validation Database in CSV format loaded into a standard spreadsheet program.

To filter sites which are in principle suitable for mesoscale surface albedo stability analysis, the criteria defined in section 2.4 were applied to the parameters extracted from the ancillary data for each site. Several tests are applied. As a site might pass a test for some of the metrics while failing for others, the total number of passed tests is stored in the database as well. This enables the user to easily filter the database in accordance to the number of successful tests and assign own mechanisms to select suitable stations thereafter.

Each site is characterised through a comprehensive report. The report is based on a flexible HTML template, which allows to easily adapting the output format. The advantage of using HTML is that a user can browse through site-specific information without need for any additional software. Information on all sites is merged into a single static HTML directory, which allows to easily transferring the data. A summary page with all processed stations is provided, indicating whether a particular site is matching the GCOS criteria or not. The summary page also contains further information about the spatial site coverage.

2.5.3 Overview of pre-selected sites

A total of 652 sites (Figure 11, left) were identified to fulfil all seven criteria defined in Table 2, covering a large portion of the globe. Figure 11 (right) shows the number of identified stations per 10° latitude band with maximum in the 30° N - 40° N latitude band. Relatively few sites were identified for latitudes larger than 50°. Identifying more boreal zone targets would be beneficial for the validation of surface albedo (and other) data products derived from polar orbiting satellites.
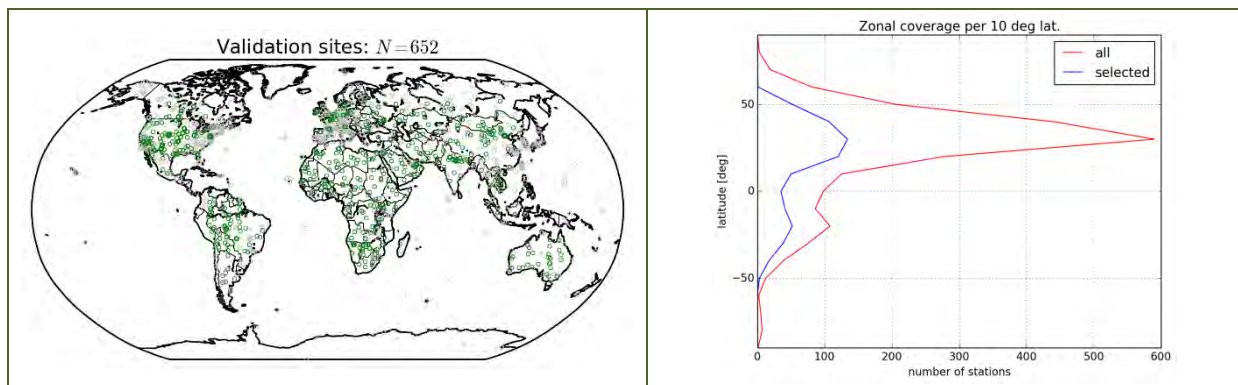
Figure 11: Selected GSA validation sites fulfilling the defined criteria (left) and zonal distribution in 10° latitude bands for all stations and selected stations (right).

The selected sites encompass a large variety of different land cover types. Figure 12 shows the number of stations for all sites contained in GSAVALDB as well as the selected GSA validation sites. The dominant land cover types of the GSA validation sites are cropland, grassland and bare areas. The different sites also cover a wide range of surface albedo conditions.
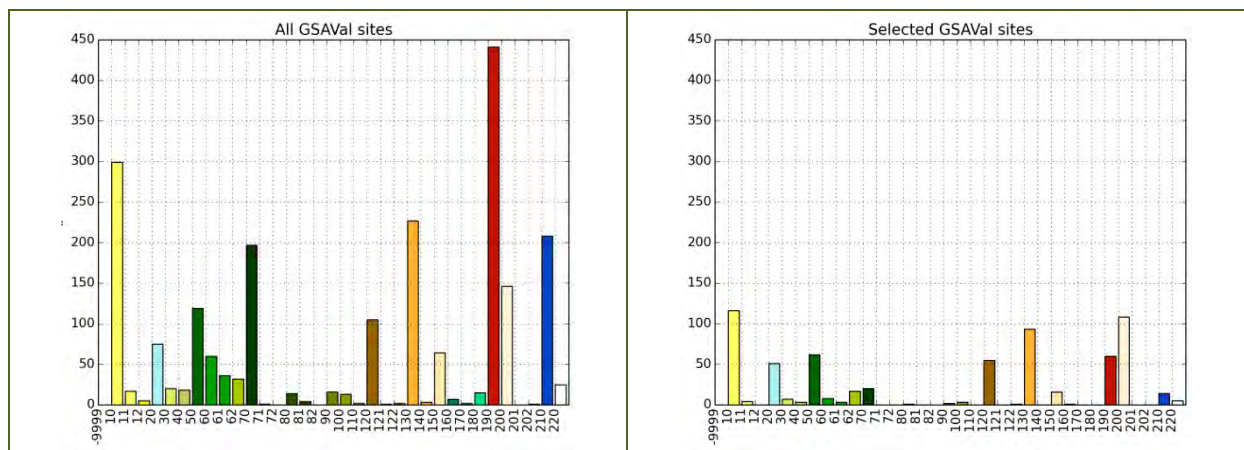
Figure 12: Land cover types of all sites identified (left) and selected sites (right). See Figure 4 for an explanation of the land cover labels.

Figure 13 shows the frequency of the albedo values covered by the entire GSAVal sites as well as those identified by applying the filter criteria. The selected GSA validation sites cover a wide range of latitudes, land cover types and surface conditions and are therefore expected to provide a comprehensive subset of surface conditions suitable for the evaluation of GSA data products.
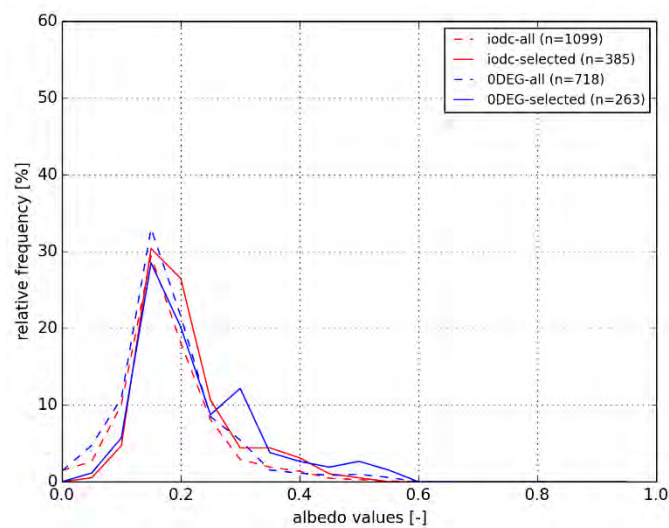
Figure 13: Histogram of surface albedo values covered by the GSAVal database (dashed lines: all sites, solid lines: filtered sites).

2.6 Conclusions and recommendations

The GSA Validation Database established in the frame of ALBEDOVAL-2 provides the currently most comprehensive characterization of potential sites for surface albedo validation. We would therefore recommend making it available to the research community by the following means:

➢ publication of a scientific article, documenting the GSAVALDB methodology,

➢ publication of the GSAVALDB on a website (possibly together with CEOS LPV group),

➢ publication of the processing framework developed through ALBEDOVAL-2.

Further enhancements of the GSA Validation Database could include:

➢ enhancing format and design of the site reports,

➢ implementing a flexible interface that allows for the integration and cross-comparison of MSA data with other surface albedo data products,

➢ establishing an on-demand processing facility to generate site reports for arbitrary coordinates. This would allow external users to characterise their "own" reference sites.

3. Anisotropy effects (Task 2 and Task 3)

3.1 Expected outcome

The expected outcome [of Task 2] is an improved characterisation of anisotropy effects in the GSA data record and the assessment of the underlying BRF model. The expected outcome [of Task 3] an assessment of the GSA method to estimate BHR_ISO and DHR_30.

3.2 Theoretical background

3.2.1 BRF, BRDF, incident and reflected radiation

The bidirectional reflectance factor (BRF) and the bidirectional reflectance distribution function (BRDF) are related as follows:

$$BRF: \rho(\theta_i, \phi_i, \theta_r, \phi_r) \,,$$
$$BRDF: {}^{1}\!/_{\pi} \times BRF \,. \tag{5}$$

Here, θ and ϕ refer to zenith and azimuth angles, respectively, and the subscripts *i* and *r* denote the cases of incident and reflected light. The above notation is consistent with *EUMETSAT [2014-A]* and is also used throughout this document. In the formulation used here, a factor of $1/\pi$ needs to precede various integrals. With this definition, for a collimated beam $I_0^\downarrow(\theta_{i0}, \phi_{i0})$ incident on the surface, the upwelling radiance $I^\uparrow(\theta_r, \phi_r)$ becomes:

$$I^\uparrow(\theta_r, \phi_r) = {}^{1}\!/_{\pi} \; \rho(\theta_{i0}, \phi_{i0}, \theta_r, \phi_r) \, I_0^\downarrow(\theta_{i0}, \phi_{i0}) \; \cos\theta_i \,. \tag{6}$$

Note, that $\cos\theta_i$ appears for the incoming radiation because for non-zero incidence zenith angles the incident radiation is purely geometrically distributed over a larger area proportional to $1/\cos\theta_i$.

For an arbitrary downwelling radiation field $I^\downarrow(\theta_i, \phi_i)$, one has to integrate over a unit hemisphere over all incident directions to obtain the total intensity for a given reflected direction:

$$I^\uparrow(\theta_r, \phi_r) = {}^{1}\!/_{\pi} \int_0^{2\pi} \int_0^{\pi/2} \rho(\theta_i, \phi_i, \theta_r, \phi_r) \, I^\downarrow(\theta_i, \phi_i) \; \cos\theta_i \, \sin\theta_i \, d\theta_i \, d\phi_i \,. \tag{7}$$

The relation between upwelling flux and upwelling radiance is now:

$$F^\uparrow = \int_0^{2\pi} \int_0^{\pi/2} I^\uparrow(\theta_r, \phi_r) \; \cos\theta_r \, \sin\theta_r \, d\theta_r \, d\phi_r \,. \tag{8}$$

In the most general case, the relation between incident flux and incident radiance is given as:

$$F^\downarrow = \int_0^{2\pi} \int_0^{\pi/2} I^\downarrow(\theta_i, \phi_i) \; \cos\theta_i \, \sin\theta_i \, d\theta_i \, d\phi_i \,. \tag{9}$$

And for the case of a collimated beam:

$$F^\downarrow = \pi\, I_0^\downarrow(\theta_{i0}, \phi_{i0})\, \cos\theta_{i0}\,. \tag{10}$$

The reflectance is always defined as:

$$r = F^\uparrow / F^\downarrow\,. \tag{11}$$

We note here, that in the general case, the reflectance depends explicitly on the incoming light field and its angular distribution as well as on the BRF.

3.2.2 BHR_ISO

The above quantities allow for the calculation of the two quantities BHR_ISO and DHR_30, which are reported in the MSA product. The bi-hemispherical reflectance factor BHR_ISO is the albedo of the surface under idealized 'white sky' conditions, i.e. isotropic distribution of the downwelling light field $I^\downarrow(\theta_i, \phi_i) = I^\downarrow = const$. For this case, we get from Equations (9) and (11):

$$rF^\downarrow = \pi\, I^\downarrow, \tag{12}$$

and from Equations (7) and (8):

$$F^\uparrow = I^\downarrow / \pi \int_0^{2\pi}\int_0^{\pi/2}\int_0^{2\pi}\int_0^{\pi/2} \rho\,(\theta_i, \phi_i, \theta_r, \phi_r)\, \cos\theta_i\, \sin\theta_i\, d\theta_i\, d\phi_i\, \cos\theta_r\, \sin\theta_r\, d\theta_r\, d\phi_r\,, \tag{13}$$

which is just a function of the BRDF and the observation angles. Note the factor of $1/\pi$ cancels with the (trivial) integration over the azimuth of the incident radiation. If, in addition to the incoming light field the surface reflectance is also rotationally invariant, the BRF only will depend on relative azimuth only. In this case the integration over ϕ_r yields another factor of 2π and BHR_ISO becomes:

$$BHR_{ISO} = \frac{F_{ISO}^\uparrow}{F_{ISO}^\downarrow} = 2/\pi \int_0^{2\pi}\int_0^{\pi/2}\int_0^{\pi/2} \rho(\theta_i, \theta_r, \phi)\, \cos\theta_i\, \sin\theta_i\, d\theta_i\, \cos\theta_r\, \sin\theta_r\, d\theta_r\, d\phi\,. \tag{14}$$

BHR_ISO can be interpreted as the ratio of upwelling over downwelling radiative flux under homogeneous illumination conditions. It is therefore sometimes referred to as white sky albedo (WSA). If $\rho = \rho_0 = const$, the above integral yields $BHR\_ISO = \rho_0 = BRF$.

3.2.3 DHR_30

The Directional Hemispherical Reflectance DHR_30 is the reflectance of the surface described by a given BRDF for a collimated beam incident at an angle $\theta_i = 30°$. The relation between incident flux and incident radiance is given by Equation (10). The upwelling flux is:

$$F_{30}^{\uparrow} = {I^{\downarrow}}/{\pi} \int_{0}^{2\pi} \int_{0}^{\pi/2} \int_{0}^{2\pi} \int_{0}^{\pi/2} \rho\,(\theta_i, \phi_i, \theta_r, \phi_r)\,[\pi\,\delta(\theta_i - 30°)\,\delta(\phi_i - \phi_{i0})]$$
$$\times\,\cos\theta_i\,\sin\theta_i\,d\theta_i\,d\phi_i\,\cos\theta_r\,\sin\theta_r\,d\theta_r\,d\phi_r\,. \tag{15}$$

Integrating over the incidence angles and assuming BRF to only depend on relative azimuth yields:

$$F_{30}^{\uparrow} = I^{\downarrow}\,\cos 30°\,\int_{0}^{2\pi} \int_{0}^{\pi/2} \rho\,(30°, \phi_{i0}, \theta_r, \phi_r)\,\cos\theta_r\,\sin\theta_r\,d\theta_r\,d\phi_r\,. \tag{16}$$

We therefore get:

$$DHR_{30} = \frac{F_{30}^{\uparrow}}{F_{30}^{\downarrow}} = \frac{1}{\pi}\int_{0}^{2\pi} \int_{0}^{\pi/2} \rho\,(30°, \phi_{i0}, \theta_r, \phi_r)\,\cos\theta_r\,\sin\theta_r\,d\theta_r\,d\phi_r\,. \tag{17}$$

If $\rho = \rho_0 = const$, the above integral again yields $DHR\_30 = \rho_0$.

3.3 Model description

3.3.1 The Rahman-Pinty-Verstraete (RPV) BRF model

The Rahman-Pinty-Verstraete (RPV) BRF model *[Rahman et al., 1993]* describes the BRF as a function of four parameters:

$$\rho(\theta_i, \theta_r, \phi, k, \rho_0, \Theta) = \rho_0\,M(k, \theta_i, \theta_r)\,F(\Theta, \theta_i, \theta_r, \phi)\,H(\rho_c, \theta_i, \theta_r, \phi)\,, \tag{18}$$

or shorter, suppressing the angular dependencies and only showing the functional parameters:

$$\rho(k, \rho_0, \Theta) = \rho_0\,M(k)\,F(\Theta)\,H(\rho_c)\,. \tag{19}$$

The notation using M, F, and H follows the notation in *EUMETSAT [2014-A]*, see Equation 26, page 32 therein. Note, that the RPV BRF only depends on relative azimuth. Also, the three functions M, F, and H are not normalized, so that ρ_0 cannot be directly interpreted as the average reflectance, although it does control the overall brightness of the surface in general. Furthermore, ρ_c is set constant in the retrieval addressed here, so that the only functions governing the anisotropy are M and F. M and F each depend on only one parameter, k and Θ, which, together with ρ_0 and the aerosol optical depth (AOD) constitute the MSA retrieval parameters *[Pinty et al., 2000-B]*. DHR_30 and BHR_ISO are subsequently calculated from the equations listed above.

3.3.2 The OPAC aerosol scattering database

Developed in 1998, the *Optical Properties of Aerosols and Clouds* (OPAC) dataset contains microphysical and optical properties of water droplets, ice crystals, and aerosol particles at several wavelengths in the solar and terrestrial spectral range *[Hess et al., 1988]*. Optical properties are provided for eight different humidity conditions for water droplets and hygroscopic aerosols. In this study, the optical properties for sulphates, the only hygroscopic aerosol used, are assumed to be in a

condition of 80% relative humidity. For this study, optical properties for two aerosol types are used (clean continental and polluted continental). Polluted continental aerosol has a higher soot fraction and consequently a lower single scattering albedo: 0.88 for the polluted continental versus 0.96 for the clean continental aerosol type.

3.3.3 Fitting MISR to the Meteosat spectral response function

We wish to compare reflectances, so we need to find weights w_i that minimize the root-mean square difference between the Meteosat sensor response function for the VIS channel F_{M5}.[9] and the weighted MISR (*Multi-angle Imaging SpectroRadiometer*) sensor response functions $F_{MMISR,i}$ (see Figure 14) accounting for the relative incoming solar radiation as well. Thus, we need to minimize the function:

$$x^2 = \int \left[S(\lambda) \left(F_{M5}(\lambda) - \sum_{i=1}^{4} w_i \, F_{MISR,i}(\lambda) \right) \right]^2 d\lambda, \tag{20}$$

where $S(\lambda)$ is the TOA spectral solar irradiance. Additionally, we need to constrain the weights so that $\sum w_i = 1$. This was done using a Levenberg-Marquardt minimization. The resulting optimal weights for MISR are given by:

$$w_i = [0.30103156, 0.23567537, 0.18607002, 0.27722306], \tag{21}$$

where the weights refer to the four VIS/NIR MISR channels in order of increasing wavelength. All MISR reflectance plots subsequently shown are based on these coefficients (see e.g. later on in section 3.5.2).

---

[9] This analysis has only been performed for MVIRI on Meteosat 5. Minor differences are expected for the other Meteosats, but this will not affect the overall conclusions.
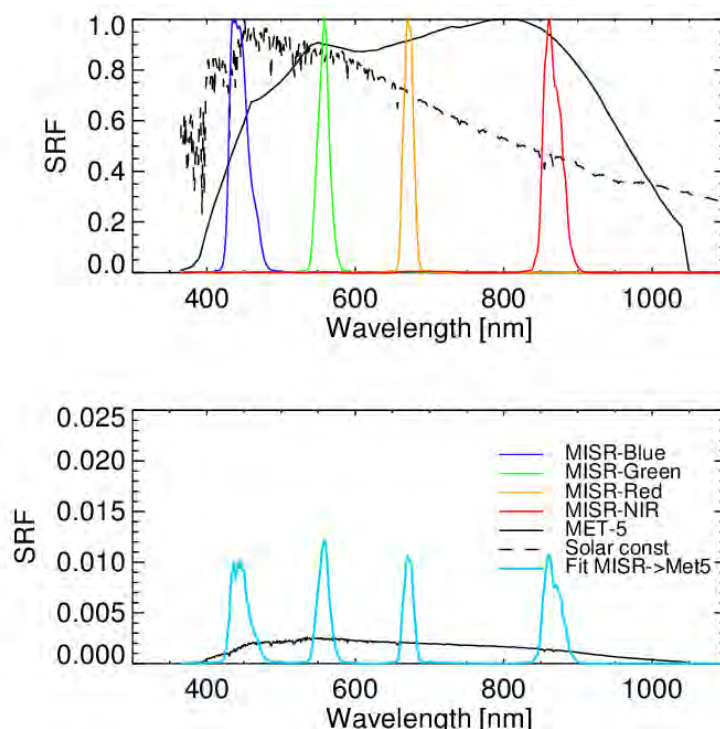
Figure 14: MISR and Meteosat-5 filter functions and solar constant (upper plot) as well as MISR filter functions weighted to best represent the Meteosat-5 filter function (lower plot).

3.4 Observational datasets

3.4.1 MSA data

MSA and auxiliary data were obtained from the operational EUMETSAT archive including all auxiliary datasets for the entire 0DEG and IODC time series. In order to facilitate comparisons of long time series, an IDL routine developed in the context of ALBEDOVAL-1 was adapted to allow for the extraction of time series of all parameters contained in the MSA files. Extraction is done for $n \times n$ windows around an arbitrary reference point within the 0DEG or IODC coverage areas. This routine was further enhanced to also provide all auxiliary information which include, amongst others, the retrieved values of aerosol optical thickness and BRF model parameters. This routine was also used in all other tasks to provide the MSA time series required for task-specific analyses.

3.4.2 MISR data

MISR data *[Diner et al., 1998]* were obtained for selected comparison sites to study the angular dependence of surface albedo. For this study calibrated and geolocated top-of-atmosphere MISR reflectances (Level-1B) data were used in order to provide an observational reference for MSA that is

not influenced by post-processing steps such as atmospheric correction or application of BRDF models. MISR data were obtained from NASA's *Atmospheric Science Data Center* (ASDC).[10]

MISR observes reflected solar radiation at nine different angles between 70.5 degrees forward and 70.5 degrees backwards along the satellite's flight direction. It provides four channels between 443 nm and 865 nm (see Section 3.3.3) and has a spatial resolution of about 300 m. Global coverage is nine days, with repeat coverage between 2 and 9 days depending on latitude.[11]

For each overpass, MISR data consist of a set of different files for each channel and camera as well as auxiliary files for observation angle, navigation, and topography. Obtaining one year of MISR observations for one calibration site requires downloading, subsetting, merging and quality control of about 300 GB of data, which is half the size of the *entire* MSA dataset. For the present study, we used MISR data for the year 2009. The large amount of data to be processed and quality controlled (i.e. cloud screening) allowed to process only a comparably small set of MISR observations. The selection of comparison sites and the cloud screening performed are described in the following sections.

3.4.3 Selection of study sites

Four sites were selected to study anisotropy related effects in the MSA product:

➢ Two sites over homogeneous, bright, and temporarily stable desert surfaces,

➢ two sites over homogeneous, relatively dark, and temporarily stable tropical rain forest.

For each of these two surface types, one site was chosen to have a similar observation zenith angle for both 0DEG and IODC observation geometries and the other site was chosen to maximize the difference between the IODC and 0DEG observation zenith angles (Figure 15).

---

[10] https://eosweb.larc.nasa.gov/project/misr/misr_table

[11] More information on MISR can be found under https://www-misr.jpl.nasa.gov/Mission/misrInstrument/

Figure 15: Selection of sites for the MISR *vs.* MSA comparison. All sites in the GSAVALDB with similar zenith angles for 0DEG and IODC are shown in red. The four selected sites are indicated by boxes (LIBYA, BELMANIP_00155) and blue circles (BOUMBA_BEK, OMANI_DESERT), respectively.

The actual selection of these sites was done using the GSAVALDB described in section 2. Key parameters of the selected sites are summarized in Table 3.

Table 3: Key parameters of the sites selected for the MISR vs. MSA comparison.

Name	Longitude	Latitude	0DEG zenith	IODC zenith M5 (M7)	Surface type
LIBYA	28.5	21.5	40	40 (46)	Desert
OMANI_DESERT	55.5	19.0	65	23 (22)	Desert
BELMANIP_00155	28.19	1.86	32	40 (33)	Rain forest
BOUMBA_BEK	14.61	3.10	17	55 (49)	Rain forest

3.4.4 MISR cloud screening

Cloud screening on MISR data was performed visually for all MISR granules covering the four comparison sites. Figure 16 shows an overview of the MISR granules covering the observation areas. One can see that the two rainforest sites are severely affected by cloud contamination whereas, as expected, the desert sites show much less cloud contamination. In order to establish cloud-free reflectance values for the references sites, a two-step approach was used.

➢ Firstly, each overpass was visually inspected for cloud cover based on the RGB-images shown in Figure 16 below. Overpasses with more than about 20-30% of cloud cover were removed from the analysis.

➢ Secondly, for the remaining overpasses the median site reflectance for each camera and channel was considered as being representative for the scene reflectance at the given camera angle and wavelength. The median was preferred over the mean reflectance in order to minimise bias due to the presence of remaining clouds.
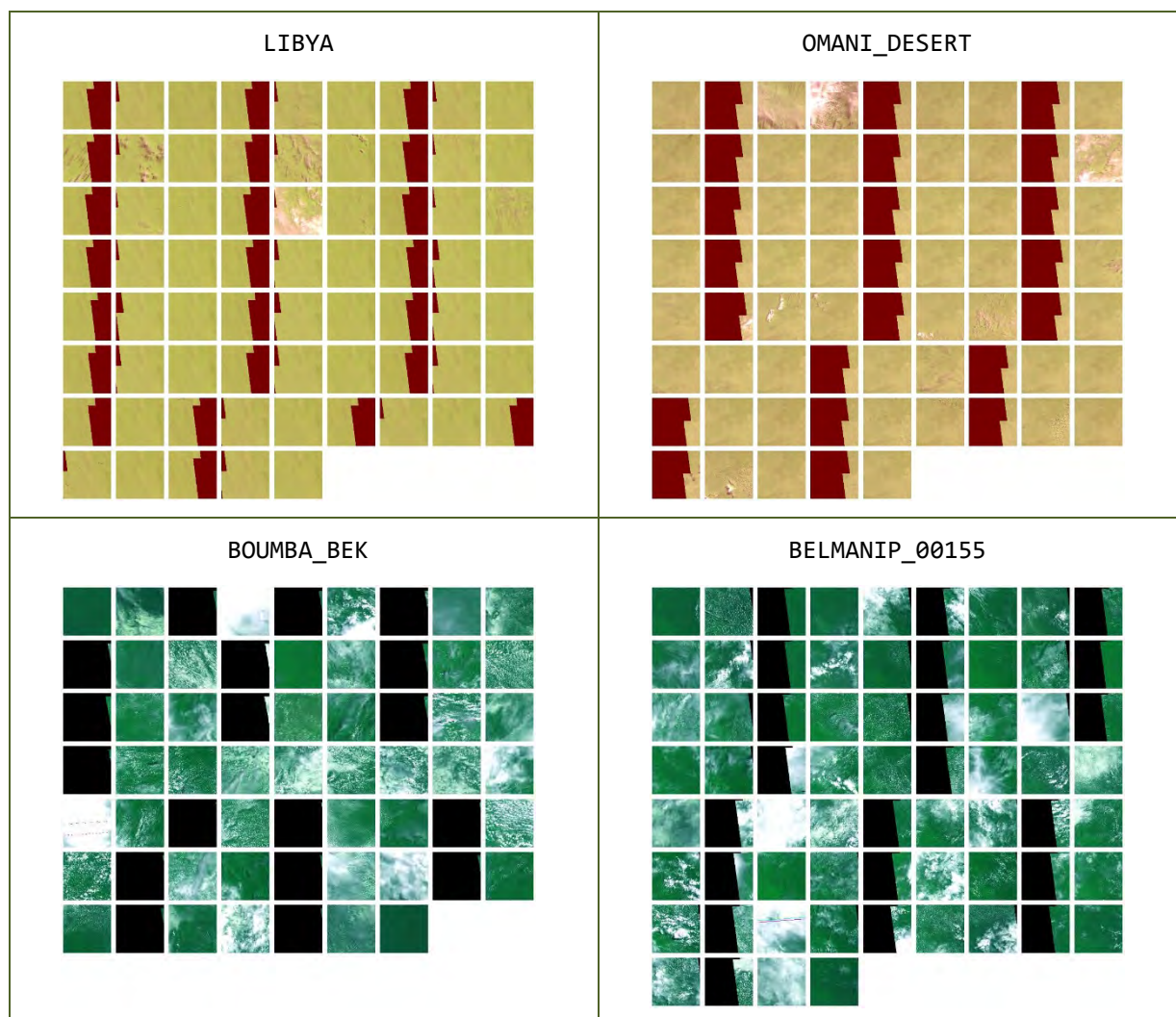
Figure 16: Overview of MISR granules for the four comparison sites. Each granule shows an area of 100x100 km centred at the reference site. Areas with no MISR data are shown in dark red for desert sites and black for the rain forest sites, respectively.

In particular, the two rainforest scenes in Figure 16 highlight the issue with cloud screening over tropical rainforests. There are only very few scenes that are entirely cloud-free, which causes issues with MSA in particular because the MSA resolution is inferior to the MISR resolution. Therefore, clouds of sizes smaller that the MSA resolution will gradually increase the reflectance and bias the observed reflectance towards higher values. For sub-scale clouds, this effect will be gradual and only after a

certain amount of sub-scale cloudiness is exceeded will any screening be able to detect those clouds. This effect is obviously exuberated at higher zenith angles as spatial resolution decreases.

3.5 Results

3.5.1 Characterisation of study sites
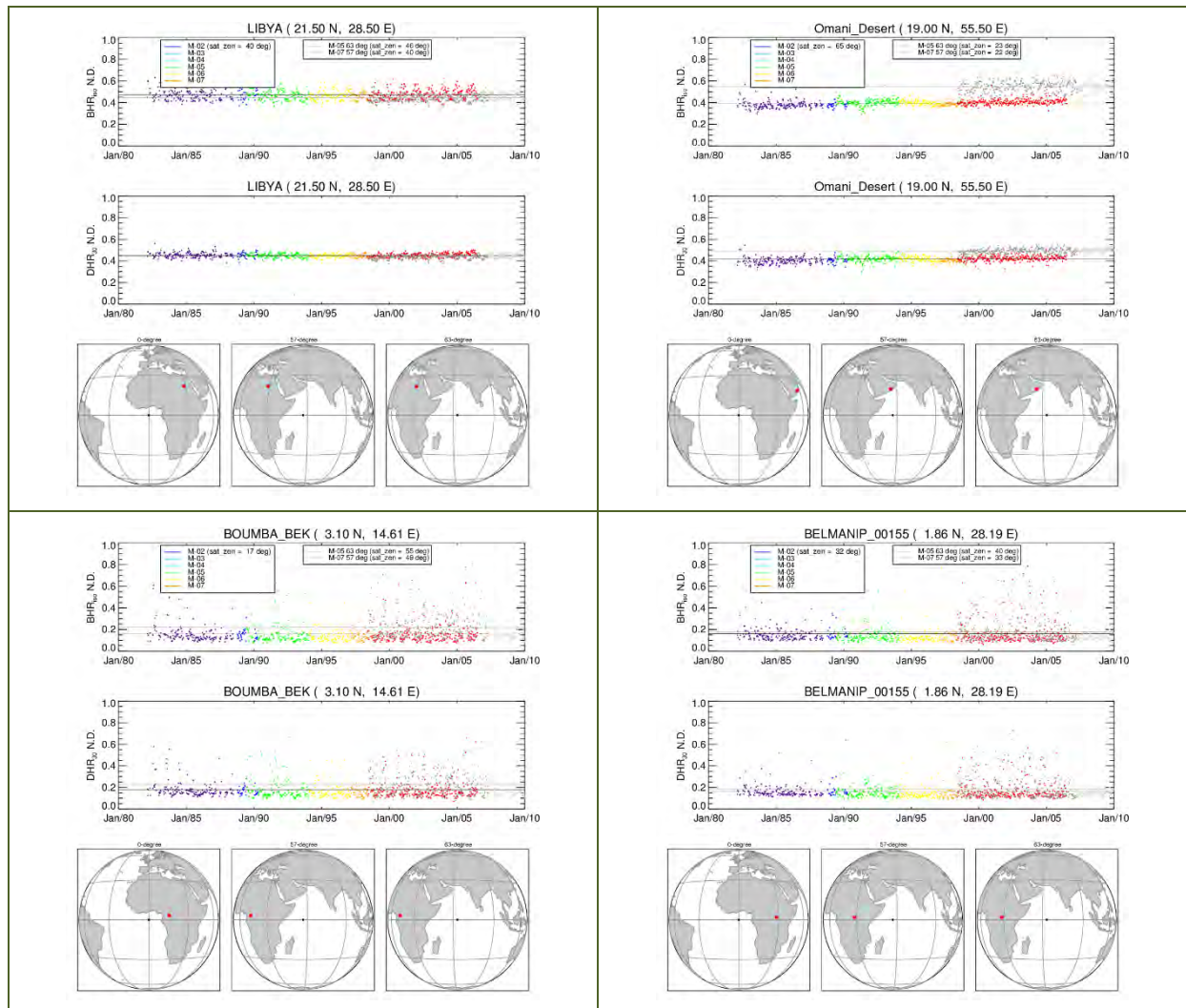
Figure 17: MSA overview for the four selected MISR comparison sites. The upper two panels of each plot show the time series of BHR_ISO and DHR_30 for both IODC and 0DEG. The lower panel shows the location of the respective reference site (red dot) on the three Meteosat coverages (0DEG, IODC 57, IODC 63).

Figure 17 shows the MSA surface albedo for the four sites selected in section 3.4.3. One can identify the following:

➢ All four sites are stable over time. This is in principle an expected result as those sites were selected to represent stable targets.

➢ The two rainforest sites (BOUMBA_BEK and BELMANIP_00155) show large positive outliers over the entire time series representing cloud contamination issues.

> ➢ The two sites with different observation zenith angles under 0DEG and IODC (OMANI_DESERT and BOUMBA_BEK) show systematic differences in their average retrieved albedo.

> ➢ In contrast, the two sites with similar observation zenith angles (LIBYA and BELMANIP_00155) show a good agreement between IODC and 0DEG albedo estimates.

> ➢ The rainforest sites show a lower discrepancy between IODC and 0DEG albedo estimates than the desert sites.

The last three issues were already identified in ALBEDOVAL-1 and partly triggered this investigation.

3.5.2   MISR reflectance plots

Figure 18 summarizes statistics for the MISR data for all four sites. Over the course of the year, the solar zenith angle at observation time varies between about 15 degrees in northern summer and about 45 degrees in northern winter. Since MISR overpasses are at 10:30 am local time, the sun is always in the east in northern summer and in the southeast in northern winter. Zenith angle is lowest near summer solstice for the two desert sites around 20° N and it has two minima for the two equatorial sites (near spring and fall equinox).

For the two desert sites (OMANI_DESERT and LIBYA), the reflectance plots in Figure 18 show a larger spread between different cameras in northern winter, when the sun is at a higher zenith angle and also partly aligned with the north-south traveling direction of the satellite. Conversely, in northern summer the sun is much closer to zenith and illuminating the scene from a direction nearly perpendicular to the satellite movement. In wintertime, the backward cameras also show significantly higher reflectance than the forward cameras, which is generally consistent with a hot spot (reduced visibility of shaded areas). These effects are visible in both desert sites, but are more pronounced for the OMANI_DESERT site than for LIBYA.

The two rainforest sites show reflectances in the order of 0.2, and no clear angular dependence over the course of the year or on solar zenith angle is observed. Especially for BOUMBA_BEK, the dataset is shows significant gaps because many MISR overpasses had to be rejected due to cloud contamination. Spread between the different view angles is in the order of 0.05 up to a maximum of 0.1 in reflectance. Thus, the angular variation in reflected radiance is relatively small for the two the rain forest sites.
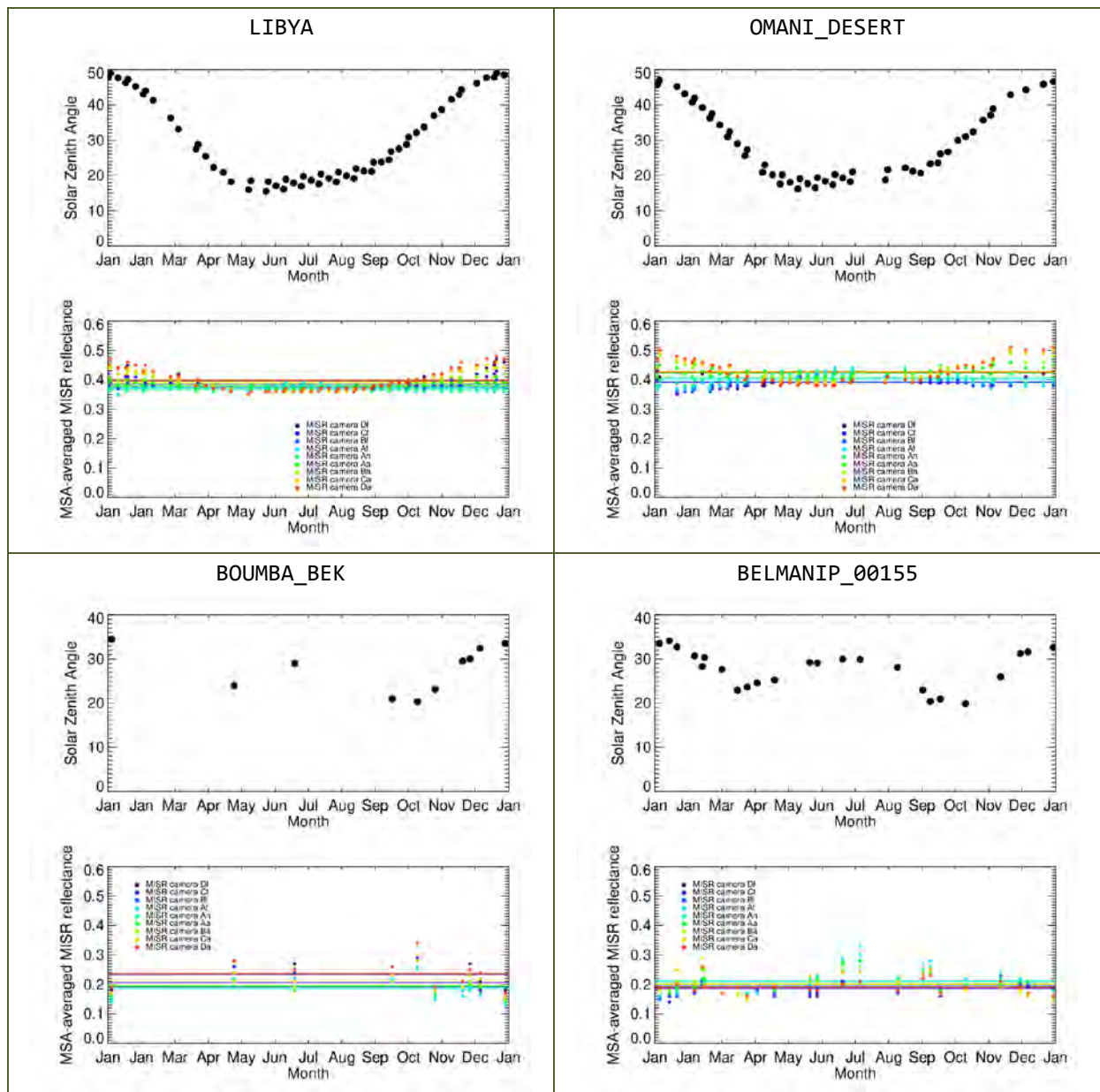
Figure 18: Summary reflectance plots for MISR. Data shown are for the year 2009. In each plot, the upper panel shows the solar zenith angle for all valid MISR overpasses. The lower panel shows the TOA reflectance of the nine MISR cameras for all overpasses. Each point represents the median per camera of an individual MISR overpass. The horizontal lines indicate the mean reflectance over all overpasses for each camera.

3.5.3   Assessing variability in the retrieval of RPV parameters

In this section, MISR reflectances are compared with BRF values derived from MSA. In the framework of these comparisons, it needs to be remembered that MISR reflectances are top of the atmosphere whereas MSA data represent surface reflectances. The differences between these two are partly due to atmospheric scattering, the impact of which is studied in Section 3.5.5.

Understanding the variability of MSA-retrieved albedo requires a deeper look into the retrieved parameters of the RPV-model. Figure 19 to Figure 22 show three-dimensional histograms of all

retrieved parameters colour-coded as a function of BHR_ISO and aerosol optical depth (AOD), respectively, for all four sites under investigation. Ideally, the retrieved RPV-parameters would be constant over time assuming a constant surface. That is, in an ideal world each surface would be characterised by time-invariant reflectance properties described by the RPV-model. In the three-dimensional space spanned by the variables $\Theta, \rho_0,$ and k, this would be represented by just one dot. If retrieval noise is accounted for, this dot would broaden toward a three-dimensional spheroid if the retrieval noise was Gaussian.
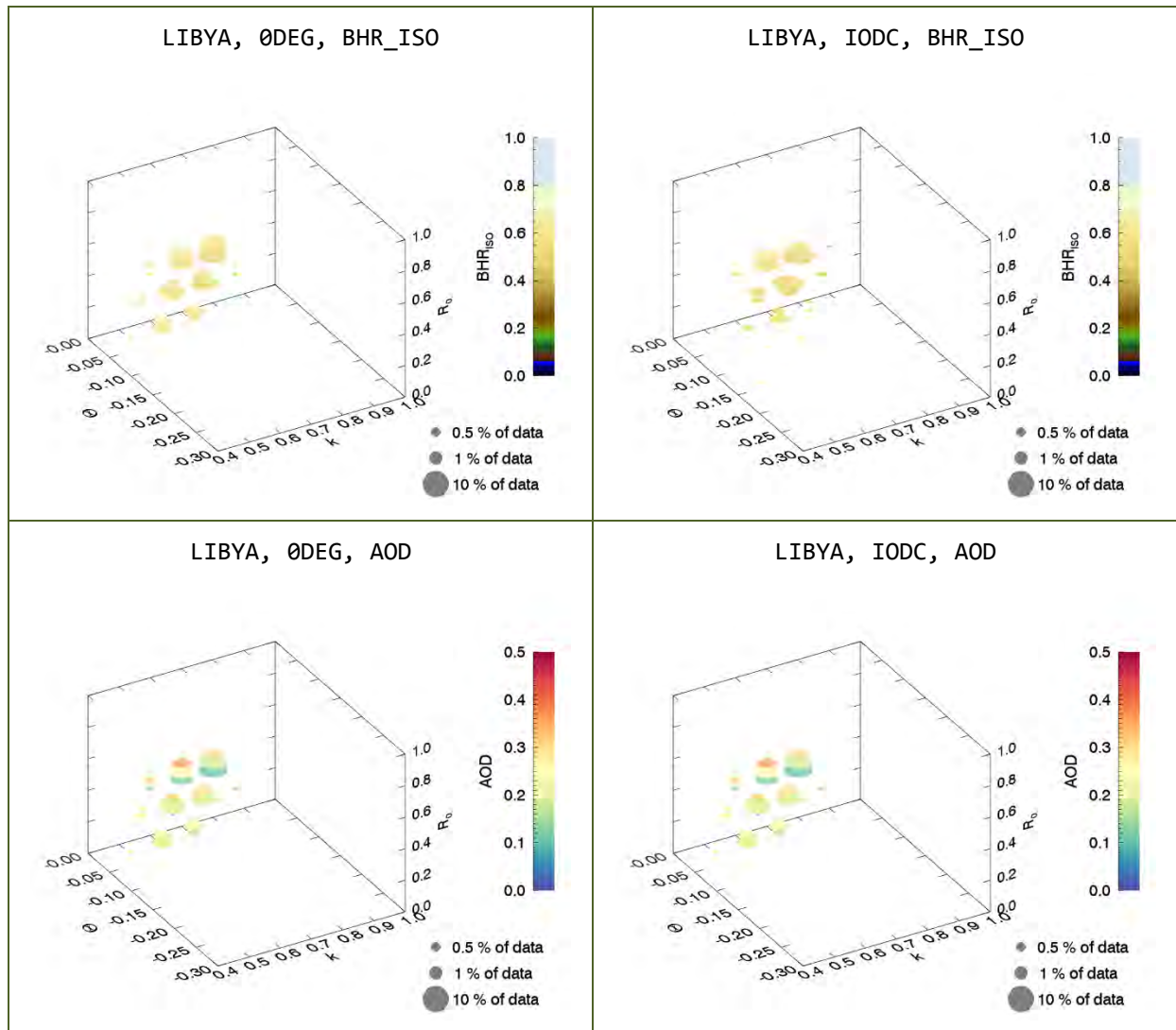
Figure 19: Distribution of the RPV parameters $\Theta, \rho_0,$ and k, for all MSA retrievals performed over the LIBYA site. The size of the circles indicates the fractional occurrence of combination of the three parameters. The colour code in the upper plots represents the corresponding BHR_ISO albedo value. The colour code in the lower plots represents the corresponding average retrieved AOD.

The LIBYA retrievals (Figure 19) come close to this ideal. All retrievals cluster tightly in the one area spanned by the three-dimensional retrieval space. Cross-talk between retrieved aerosol optical thickness and the other retrieved parameters is minimal as can be inferred from the relatively random

distribution of AOD colour codes in the lowermost two panels of Figure 19, indicating independence of the AOD from the other retrieval parameters.

For OMANI_DESERT significant deviations occur between IODC and 0DEG in the position of the most frequent retrieval combinations. This is true especially for the parameter k, which adopts values below 0.6 for all cases for IODC and above 0.6 for 0DEG. Similarly, IODC shows on average higher values for ρ_0. Thus, the retrievals populate two distinctly different subspaces of the three-dimensional retrieval space, mostly separated by different k-values. Aerosol optical thickness, although on average higher for 0DEG, does not show any significant dependencies on any of the retrieved parameters.
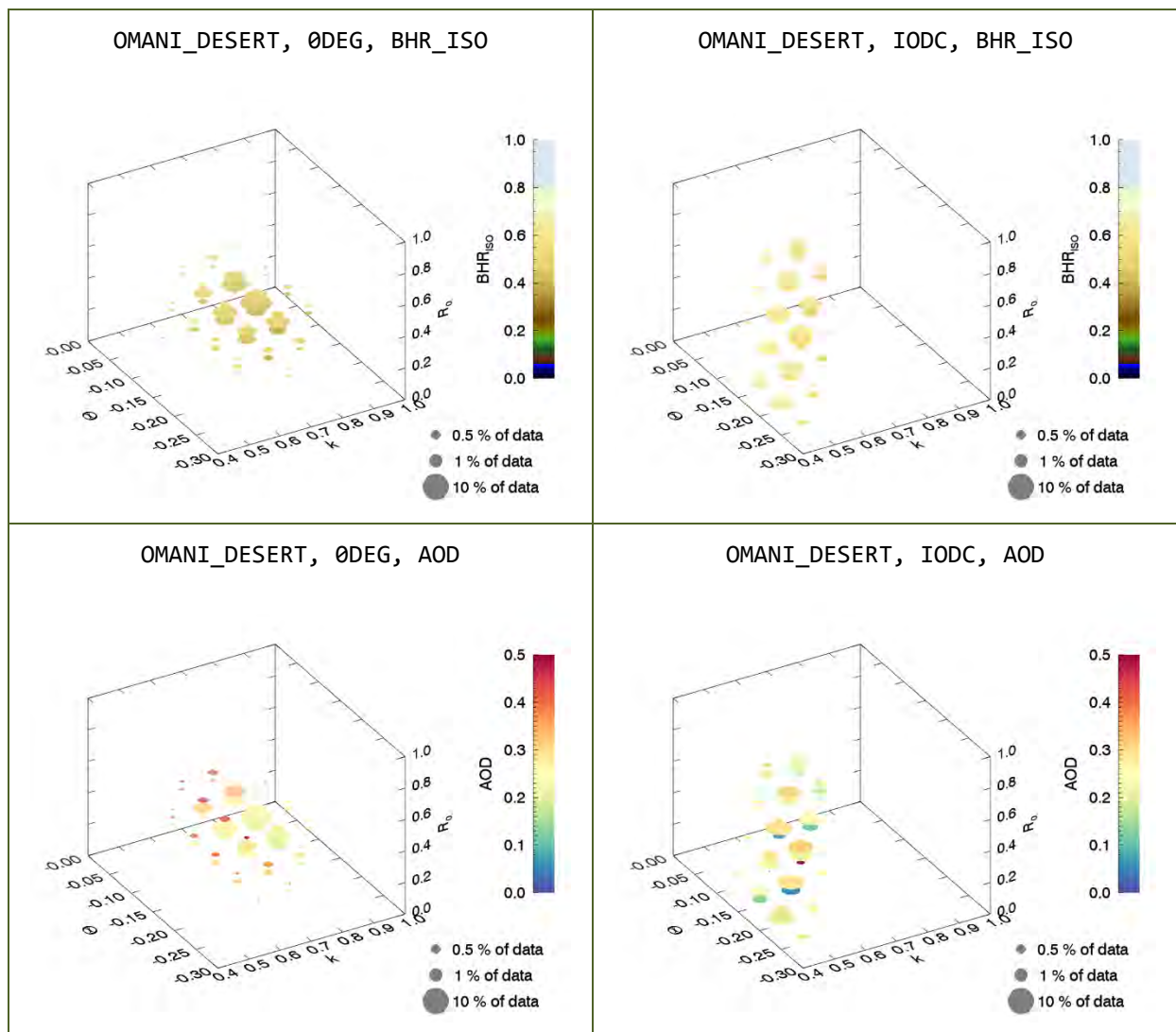
Figure 20: Same as Figure 19 but for OMANI_DESERT.

The case of the two rainforest sites shown in Figure 21 and Figure 22 differs from the desert case. For the rainforest sites, the retrieval appears to be only weakly constrained in its choice of anisotropy parameters. In particular, negative values for Θ between -0.1 and -0.3 are almost equally likely to occur and k values smaller than about 0.8 as well.

Unlike the desert cases, the rain forest cases also show a clear dependency of retrieved AOD on some of the parameters with AOD increasing generally toward higher Θ, ρ_0, and k values. This behaviour is likely due to subscale clouds, which the algorithms tries to accommodate by higher aerosol optical thickness retrievals.
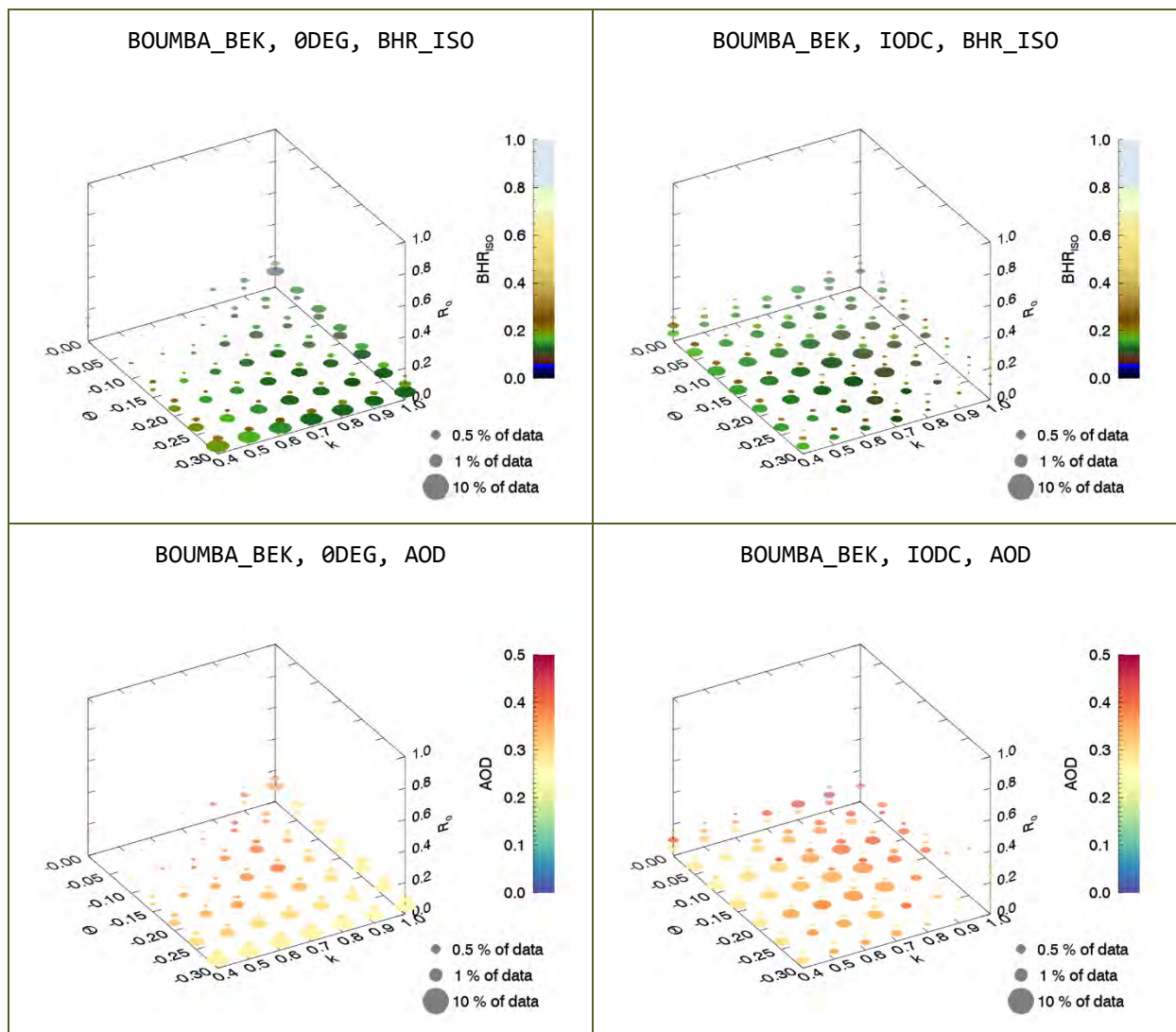
Figure 21: Same as Figure 19 but for BOUMBA_BEK.
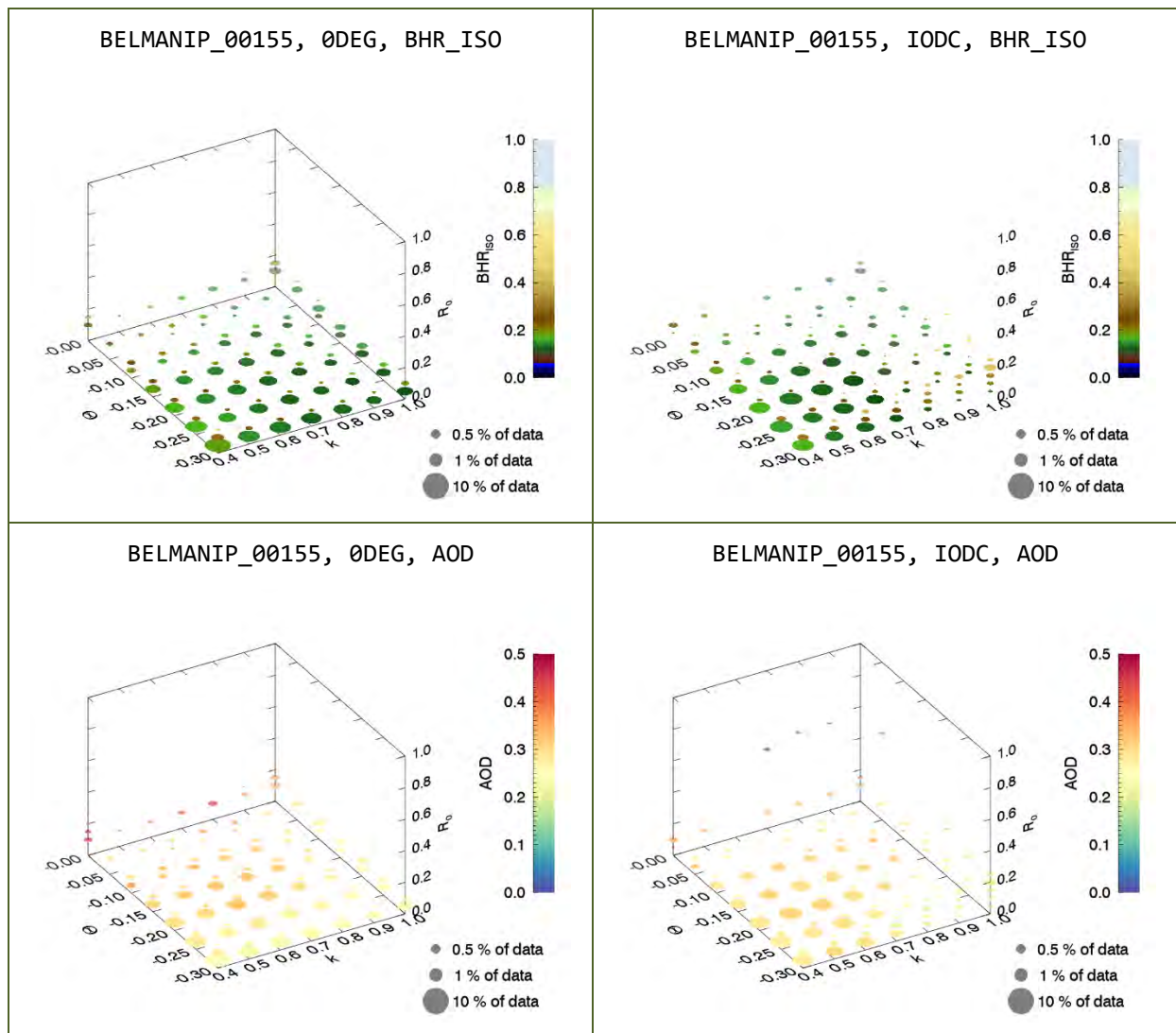
Figure 22: Same as Figure 19 but for BELMANIP_00155.

3.5.4 Bidirectional comparison MISR versus MSA

Figure 23 shows a comparison between the MISR observed reflectances and the BRF reconstructed from the MSA dataset using the BRF parameters from the corresponding MSA auxiliary files and the methodology outlined in Section 3.3. The polar plots give the value of the BRF as function of zenith angle (radial axis) and observer azimuth polar angle). For example, when the satellite is in the north of the surface and sees the scene at a zenith angle of 60 degrees, the corresponding BRF value would be on the y-axis, at location 60 degrees. Results are exemplarily shown for site OMANI_DESERT, which shows the larges deviation between IODC and 0DEG.

The corresponding solar position can be identified from the hot spot, which by example of the upper left panel is identifiable as the brighter area near 20 degrees on the positive x-axis (i.e. the sun being in the east at an angle of about 20 degrees).

The two upper plots in Figure 23 represent 'summer' situations with the sun in the east at about 20 degrees zenith angle. The two lower plots represent 'winter' with the sun in the southeast at about 45

degrees. As mentioned above, Figure 23 does not include the effects of aerosols for the MSA BRF. The following general statements can however already be made:

➢ The BRF correctly represents the larger azimuthal variability in reflectance for a solar zenith angle of 45 degrees as compared to 20 degrees.

➢ The BRF retrieved from 0DEG (left panels) is generally darker than the BRF retrieved from IODC (right panels), consistent with the differences seen between IODC and 0DEG in Figure 17.

3.5.5 Impact of aerosols

For the `OMANI_DESERT` site, the 0DEG retrieval estimates the aerosol optical thickness to be 0.15 (long-term average) whereas the IODC retrieval estimates aerosol optical thickness to be 0.56 (long-term average) at 550 nm. Figure 24 shows the top-of-atmosphere reflectance for clean continental aerosol of this optical thickness (i.e. 0.15 for 0DEG and 0.56 for IODC) with an underlying BRF identical to Figure 23. Increased backscatter by aerosols brightens the observed scene slightly and washes out the signature of the BRF. This is in particular true for IODC, where the aerosol optical depth is nearly four times as high. Figure 25 shows for comparison what would happen if the aerosol was more strongly absorbing (polluted continental). In this case the scene darkens further because of increased absorption with this effect being strongest toward high observer zenith angles. Based on these initial results we find that:

➢ The discrepancy between MISR and the MSA-based estimates is stronger for the IODC case. Figure 25 indicates that the retrieved aerosol optical thickness especially for IODC appears too high.

➢ The comparisons between MISR TOA-reflectances and MSA retrieved BRF parameters remain inconclusive. While aerosols strongly modify the visibility and features of the BRF, the inclusion of aerosols does not lead to a better agreement between the MISR reflectances and the BRF properties modelled based on MSA.

Similar conclusions can be drawn for the case of `BOUMBA_BEK` shown in Figure 26. For the particular case of `BOUMBA_BEK` (and, similarly `BELMANIP_00155`, it can also be seen that the MISR reflectances do not resemble any consistent angular dependency (as could already be observed in Figure 18). Neither 0DEG nor IODC are closer to the MISR-observed reflectances.
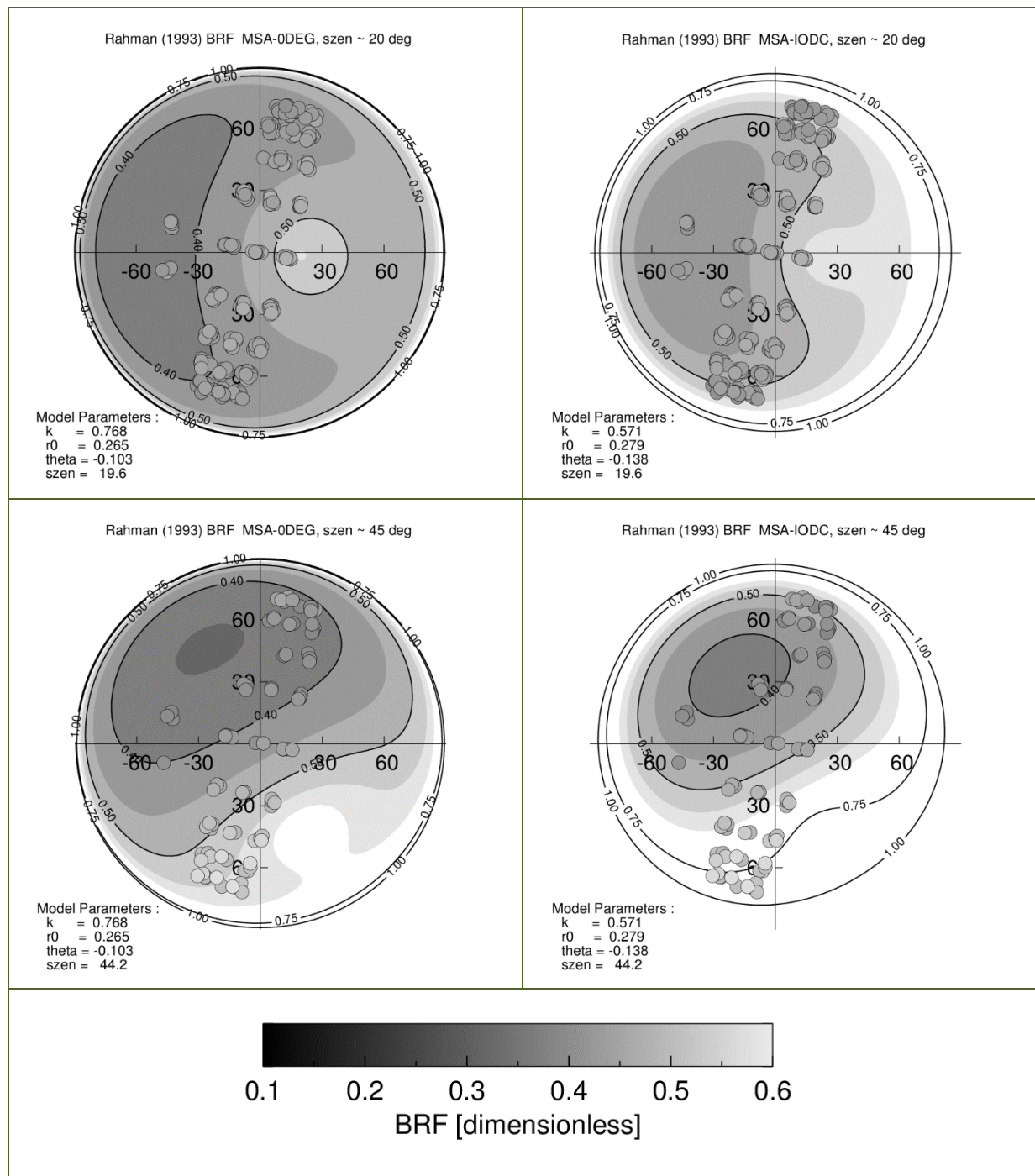
Figure 23: Surface BRF example for RPV parameters characteristic of the OMANI_DESERT site. The values for the model parameters represent the temporal average at this site for 0DEG and IODC, respectively. Top row: 20° solar zenith angle; bottom row: 45° solar zenith angle; left column: 0DEG, right column: IODC. Aerosol effects were not considered in the simulations. The overlaid dots show MISR TOA reflectances.
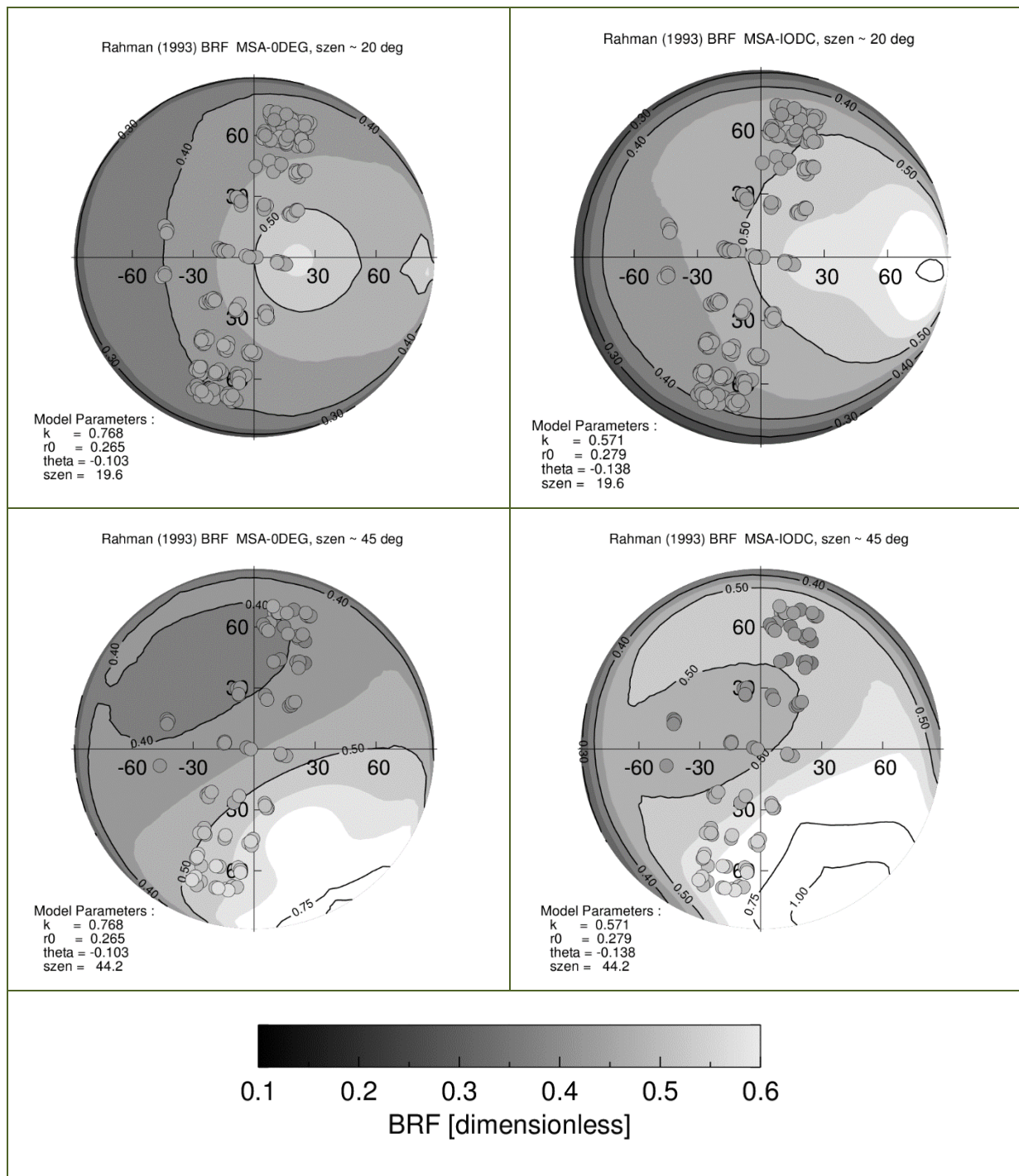
Figure 24: Same as Figure 23, but for overlying clean continental aerosol with optical thickness 0.15 for 0DEG and 0.56 for IODC. Optical thickness values reported at 550 nm. The single scattering albedo for the clean continental aerosol is 0.965.
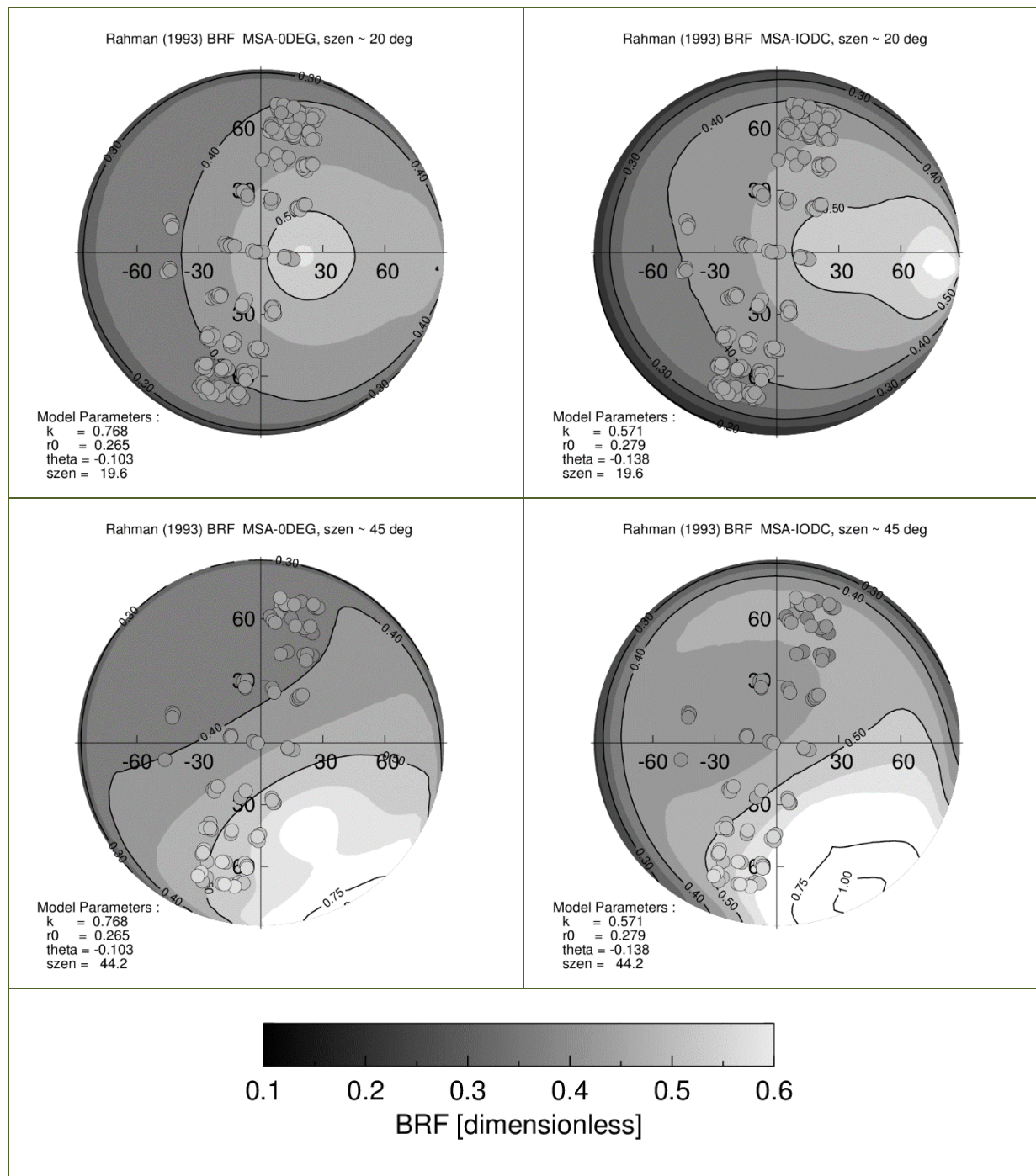
Figure 25: Same as Figure 23, but for TOA BRF for overlying polluted continental aerosol. The single scattering albedo for the polluted continental aerosol is 0.881 as compared to 0.965 for the clean continental case.
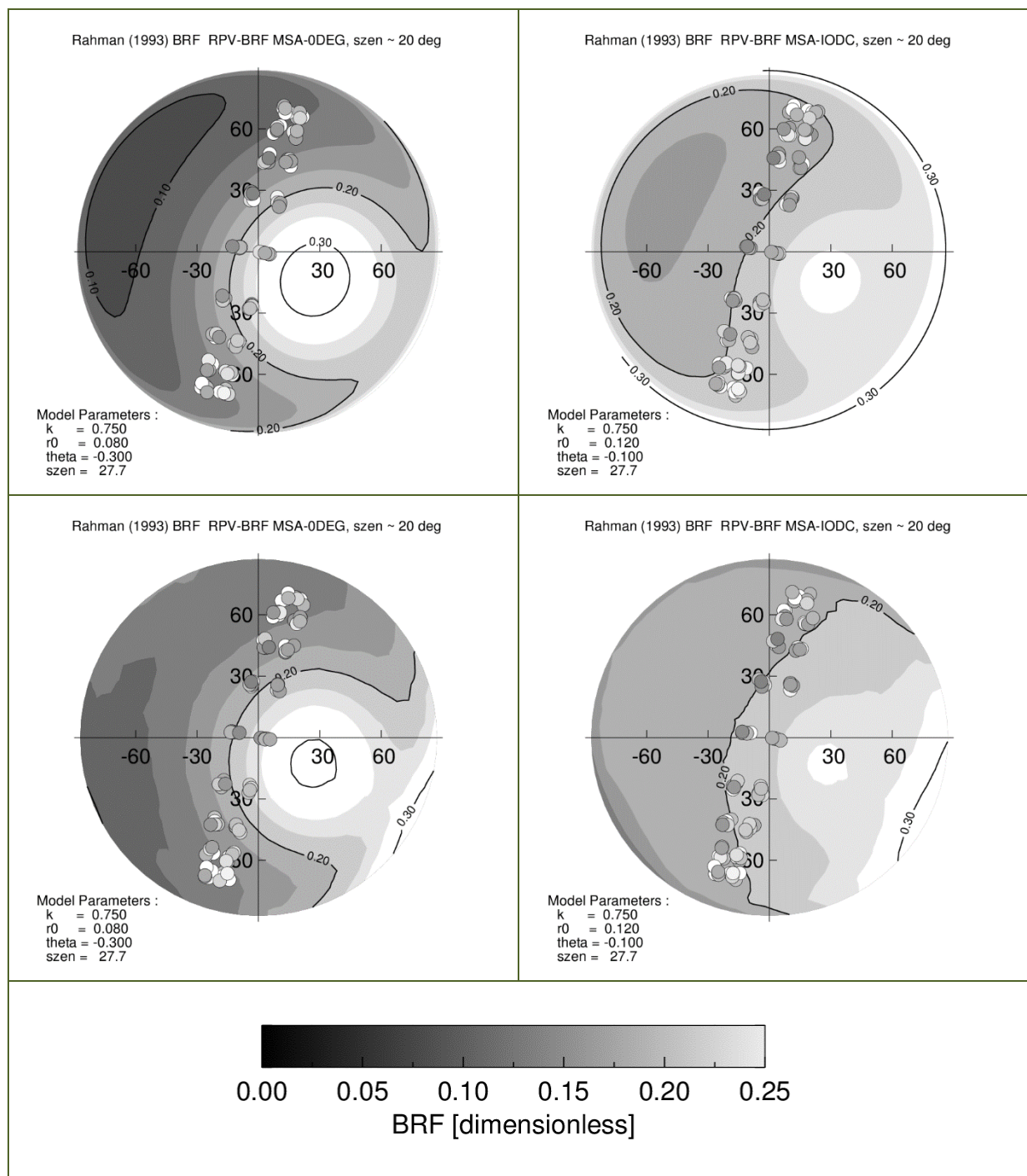
Figure 26: Similar to Figure 23, this figure shows the TOA BRF for site BOUMBA_BEK and the corresponding MISR top-of-atmosphere reflectance. The upper two plots show the BRF value, while the lower two plots show the top-of-atmosphere reflectance assuming an aerosol optical thickness of 0.2.

3.5.6   DHR_30 versus BHR_ISO

Figure 27 compares BHR_ISO with DHR _30 values for different solar zenith angles at site `OMANI_DESERT`, where differences between the two are particularly large, for the same RPV model parameters as before (see e.g. inset of Figure 23). The vertical line at 30 degrees indicates the DHR_30 reported in the MSA product. Data are shown again for the two cases 0DEG and IODC. We find the following:

➢ For both IODC and 0DEG, the value of DHR_30 is lower than the BHR_ISO value. This effect is more pronounced for IODC than for 0DEG.

➢ DHR_30 varies much more strongly as function of solar zenith angle for IODC than it does for 0DEG.

➢ The combined effect of both observations explains various features that were observed in the original time series (Figure 17), including the spread between BHR_ISO and DHR_30, the larger variability in DHR_30, and the larger variability in general for IODC.

The observed differences between the 0DEG and IODC retrievals for the same reference site are caused by inaccuracies in the MSA retrieval process. More accurate retrieval of the anisotropy parameters and the AOD should lead to a reduction of these differences. However, the observed differences between DHR_30 and BHR_ISO appear plausible and are supported by in situ observations (see e.g. Figure 38).
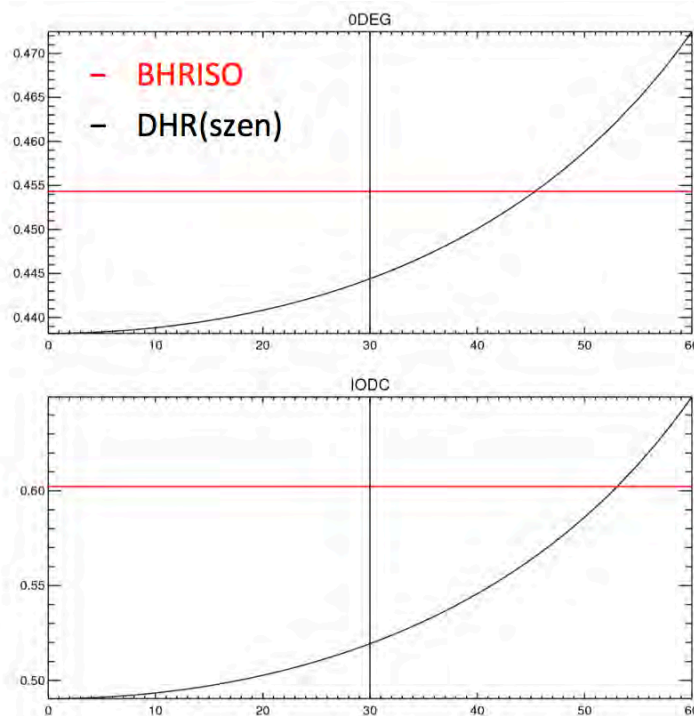
Figure 27: MSA BHR_ISO (red) and DHR_30 as function of solar zenith angle for site `OMANI_DESERT` for 0DEG (upper panel) and IODC (lower panel). The corresponding RPV model parameters are shown in the insets in Figure 23.

3.6 Conclusions and recommendations

We have analysed the BRF model underlying the MSA retrieval in order to evaluate potential avenues for improving the methodology. We have further compared simulated top-of-atmosphere reflectance based on retrieved RPV parameters with MISR observations. The results indicate the following:

➤ The GSA method optimizes a four-dimensional solution space consisting of AOD, Θ, ρ_0, and k,. Optimal choices for these parameters are determined freely within a range of allowed values. It appears the anisotropy parameters are not closely enough constrained for various surfaces.

➤ Retrieval deviations in RPV model parameters between IODC and 0DEG are significant for both the desert and the rainforest sites.

  o As already shown in ALBEDOVAL-1, differences in retrieved parameters between IODC and 0DEG for desert sites appear mainly to be correlated with differences in observation geometry.

  o The rainforest cases show a particularly large variability of retrieved anisotropy parameters indicating the retrieval to be insensitive to the actual surface conditions and possibly being rather influenced by subscale variability of cloudiness, aerosols, and other parameters.

➤ This last result is corroborated also in the relative insensitivity of MISR to observation geometry for the rainforest areas. Variability between cameras is as large as the interannual variability with no discernible anisotropy effect.

➤ In most cases over dark surfaces the product is also strongly affected by clouds. Other studies have shown that additional cloud screening efforts do have a positive impact *[Lattanzio et al., 2015]*. However, subscale cloudiness might still adversely affect retrievals and might partly also account for the large spread in anisotropy values seen especially over dark surfaces.

➤ The MSA retrievals are self-consistent, that is, reported deviations between MSA-derived BHR_ISO and DHR_30 for individual sites are consistent with underlying retrieved parameters. Typically deviations between BHR_ISO and DHR_30 are strongest for very high or for very low zenith angles, because of the solar zenith angle dependency of DHR_30.

In addition to the cloud-screening issues which are already being addressed *[Lattanzio et al., 2015]*, the findings presented here give rise to the following top level recommendation regarding future development and algorithm improvement:

➤ It is recommended to further constrain allowed choices especially of the anisotropy parameters Θ, and k.

  o Such a constraint could be implemented via a full optimal estimation (OE) algorithm that provides background values for all retrieved parameters and background error covariances that allow constraining the accepted range of these parameters to physically plausible values for different surface types.

- o Obviously, a full OE requires increased computational resources such that a trade-of between computational speed and numerical approximations would have to be made.

- ➤ Additionally, other quantities such as AOD and ρ_0 could be constrained too, but in a weaker manner, so that the algorithm would be able to optimize the overall albedo better at the cost of providing tighter constraints on the anisotropy.

  - o In a full OE framework, the background error covariance matrix determines how strongly a retrieved parameter can vary relative to the other retrieved parameters. By allowing AOD and possibly ρ_0 to vary more strongly, the optimal estimation would be able to adjust overall scene brightness better at the expense of keeping the anisotropy parameters Θ and k closer to their background values.

  - o The latter could for example be derived from previous retrievals and be allowed to only deviate by a certain amount from this background.

The implementation of such improvements could be incremental on top of the existing algorithm. Background values of anisotropy parameters as well as corresponding background error covariance could be derived from the observed variability for different surface types and from MSA existing retrievals.

4. Assessment of MSA performance over snow (Task 4)

4.1 Expected outcome

The expected outcome [of Task 4] is an improved assessment of the amount of wrongly classified snow pixels and what the impact of negligence of snow cover in the GSA data record is.

4.2 Method

Snow covers large areas over significant periods of time within the field of view of geostationary instruments. This is especially true for instruments observing large landmasses in Eurasia and North America. In the current MSA version, however, most snow-covered surfaces are filtered out by the cloud screening procedure currently applied: pixels where the BRF at TOA is above 0.6 are not considered for the retrieval *[EUMETSAT, 2014-B]*. This means that neither the MSA retrieval parameters (AOD, ρ_0, Θ, k) nor the derived surface albedo values DHR_30 and BHR_ISO are available for such pixels. This is not only the case for very bright snow surfaces (e.g. snow on grassland or snow on a frozen lake) but also for most cases of snow on vegetation, thawing snow, or glacier ice. Consequently, it is not possible to conclusively study MSA performance over snow and ice with the current MSA product. This is illustrated in Figure 28 showing DHR_30 values at two sites characterised by frequent and lasting snow cover in winter. No MSA product is provided during the first three months of 2005 at reference sites LAKE_CILDER (Eastern Anatolia, Turkey) and ADAMOWKA (Orenburg district, Russia), while it is obvious from other data sources (e.g. IMS, see section 4.3.1) that continuous snow cover was prevalent at both sites for the indicated period.
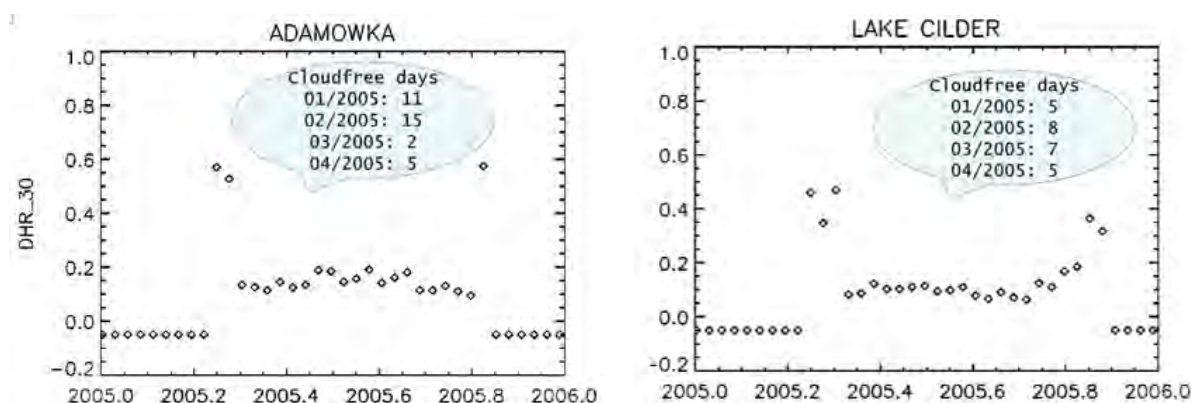
Figure 28: MSA DHR_30 time series for the year 2005 for the two reference sites ADAMOWKA (Russia) and LAKE_CILDER (Turkey), both from IODC observations. The number of cloud free days was obtained from visual inspection of MODIS RGB images.

In order to exclude the possibility of data loss due to unfavourable observation conditions, MODIS Terra RGB images were visually inspected indicating that a sufficient number of cloud free days occurred in early 2005 at both sites to allow for the retrieval of surface properties. Only at the end of the winter, a number of relatively high DHR_30 values above 0.4 are observed at both sites, probably representing melting snow or a broken snow surface, *i.e.* conditions when surface properties are unstable and not suitable for validation purposes.

In the following, it is attempted to quantitatively estimate the loss of information in the MSA data record due to the erroneous removal of bright snow surfaces. With a view on a future improved MSA version with potentially reduced loss of information above snow covered surfaces, a number of additional analyses have been made:

➤ A strategy to identify suitable reference targets for MSA validation above snow surfaces has been devised.

➤ Information on the reflective properties of pure snow has been collected from the scientific literature to support future analysis MSA performance above snow.

➤ The spectral shape of snow reflectance (which differs significantly from that of most other surface types) has been analysed in terms of the MSA spectral to broadband conversion.

These preparatory steps should support a more thorough analysis of MSA performance over snow once such product becomes available.

4.3 Distribution of snow cover

4.3.1 Snow cover reference information

In this study, the *Interactive Multisensor Snow and Ice Mapping System (IMS) Daily Northern Hemisphere Snow and Ice Analysis* product[12] at 24 km spatial resolution has been used to regionally quantify the importance of snow cover on the surface albedo. The IMS product specifies for each grid cell one of the four states "snow", "sea ice", (snow-free) "land", (ice-free) "water".

The choice of using IMS as snow reference data was motivated by a systematic study done by *Struzik et al. [2012]* who investigated the performance of four snow products (GlobSnow Snow Extent[13], MODIS MYD10C1[14], EUMETSAT H-SAF SN-OBS-1[15], and IMS) for a two-year period in Poland. They found IMS to provide the overall best performance (see Table 4): *"The best results were obtained for IMS products. Obtained POD [probability of detection] = 0.9 and FAR [false alarm rate] = 0.09 with complete coverage each day is encouraging."* These findings are supported by our own limited testing for a selected number of dates and reference sites where IMS performed better in terms of availability and accuracy than MODIS MYD10C1 or ESA's GlobSnow.

The good performance of IMS can be explained by the fact that this is a product combining automated retrieval procedures with expert visual inspection of satellite imagery and information from in situ networks. In contrast to that, the other products mentioned above are entirely based on automated retrieval schemes.

---

[12] The IMS product comes at 4 km and 24 km resolution and is available under http://nsidc.org/data/G02156.

[13] http://www.globsnow.info/se/

[14] http://nsidc.org/data/MYD10C1

[15] http://hsaf.meteoam.it/description-sn-obs-1.php

Table 4: Validation of selected satellite snow cover products against synoptic observations for the period 01.01.2009-31.12.2010 (* H-SAF since 01.10.2009). Source: *Struzik et al. [2012]*.

Parameter	GlobSnow	MODIS	H-SAF *	IMS
Hits	337	608	1171	10272
False_alarms	163	136	84	1071
Misses	162	175	311	1307
Correct negatives	4482	7480	11945	30422
Total	5144	8399	13511	43072
POD	0.68	0.78	0.79	0.89
FAR	0.33	0.18	0.07	0.09
POFD	0.04	0.02	0.01	0.03
Accuracy	0.94	0.96	0.97	0.94
CSI	0.51	0.66	0.75	0.81
Criteria for snow presence used:	Sn>50%	CI<10 & Sn>50	Flag Yes/No	Flag Yes/No

4.3.2 Snow cover of the northern hemisphere

The number of snow covered days in the northern hemisphere for the year 2005 as derived from the IMS 24 km product is shown in Figure 29. The year 2005 has been chosen as reference period to study snow cover since both IODC and 0DEG data are available for this year, which allows for direct comparisons between the two observation geometries.

Figure 29: Days with snow cover in 2005 in the northern hemisphere derived from the IMS 24 km product (transparent: no snow cover; black: 1 day snow cover; white: 360 days snow cover). Satellite zenith angles for the 0DEG and 57° IODC coverages are shown by the yellow and blue contours in steps of 15°.

Results may differ for other years, especially locally, but the main overall conclusions should remain unchanged. Due to the coarse resolution of the chosen IMS product (24 km), snow occurrence is probably underestimated in regions where snow and ice predominantly occur in areas of limited

extension (for example high mountains at lower latitudes). In the context of this study, such minor errors are deemed negligible and do not affect the main conclusions.

The zonal distribution of snow and sea ice has been calculated for the entire GeoRing for zones of 5° latitudinal extension, starting with the zone 25° N to 30° N. No significant snow coverage is found in the IMS analyses for latitudes lower than 25° N. The areas covered by the individual geostationary instruments were delineated by local satellite zenith angles $\theta_{SAT} < 75°$ (see e.g. Figure 29 for 0DEG and IODC). Calculation of the actual snow distribution is fully automated such that other latitude zones or satellite observation thresholds can easily be considered.

The globally varying land-sea distribution causes significant differences in the average snow and ice coverage per latitude zone for the different GeoRing instruments, with 0DEG showing the lowest and IODC showing the highest total average snow cover (Figure 30, left panel). The latter is mainly caused by the fact that IODC comprises by far the largest amount of land surfaces of all GeoRing observation geometries.

Significant ice coverage within the latitude range covered by geostationary satellites is only observed for GOES-E, where e.g. more than 10% of the total area between 55° and 60° has on average been covered by ice in 2005. For all other GeoRing instruments, ice cover is only locally relevant. For example, GMS shows about 2% average ice coverage in the latitude range 50°N to 55°N (Figure 30, right panel) which is mainly due to the typically four months lasting ice coverage of Lake Baikal.
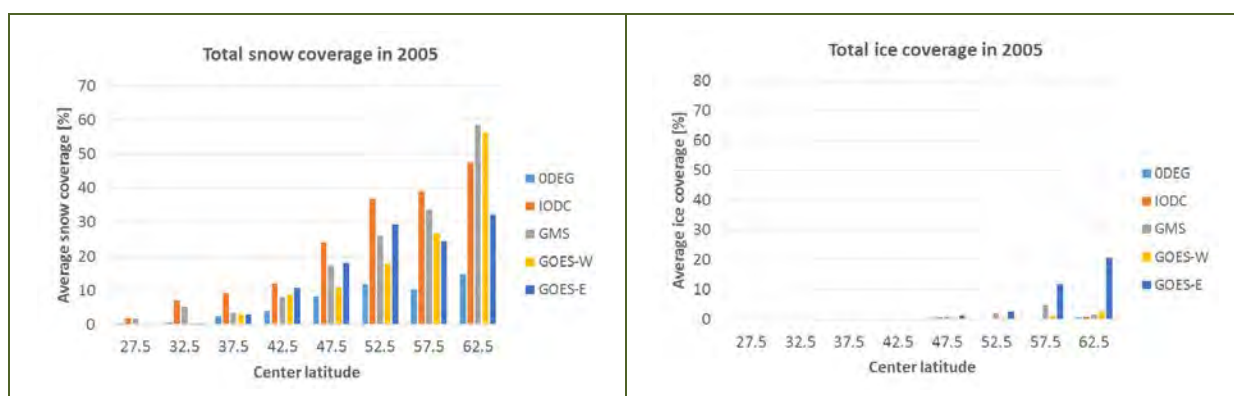
Figure 30: Total average snow and ice coverage per GEO ring instrument and latitude zone for the year 2005. Only areas with $\theta_{SAT} < 75°$ were considered.

When only considering land surfaces, climatologically driven differences in snow coverage become apparent. Normalising total snow coverage values by actual land areas gives the average snow coverage for land surfaces. Here, 0DEG consistently shows again the lowest values in average snow cover because many of the observed land surfaces in higher latitudes are characterised by rather mild ocean-influenced climates. Average snow cover for all other GeoRing instruments is significantly higher, with GMS and GOES-E often showing the highest average snow cover approaching e.g. 50% in the latitude range 50° N to 55° N.
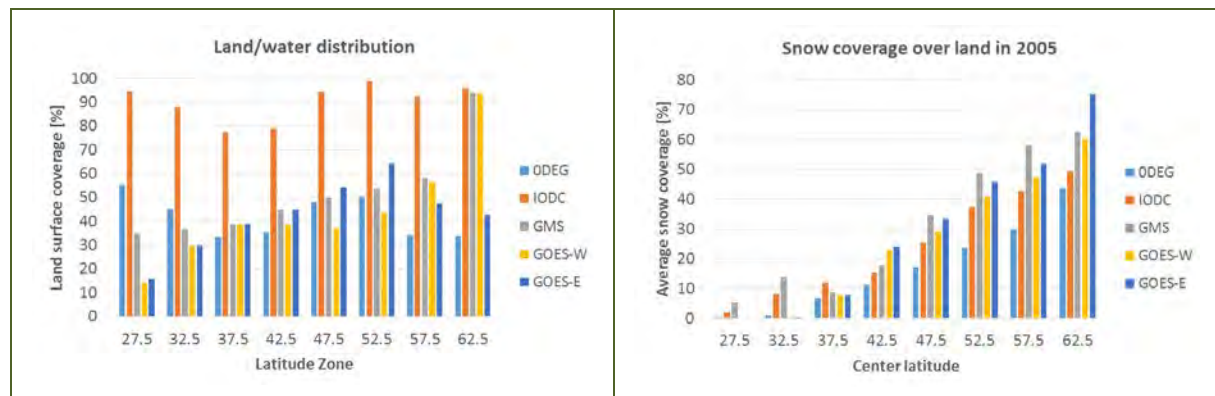
Figure 31: Land/water distribution (left panel) as well as average snow coverage over land per GeoRing instrument and latitude zone for the year 2005. Only areas with $\theta_{SAT} < 75°$ were considered.

It is worth mentioning that a number of areas at rather low latitudes are characterised by a significant average annual snow coverage. Such areas play a significant role in the climate system as they reflect large amounts of the incident solar radiation back to space in the winter months. The most important such case concerns the Tibetan haut plateau, as evidenced by significant average snow cover for the 30° to 35° N zones of the GMS and IODC coverages.

4.3.3 MSA information loss due to snow cover

The upper limit of snow-related data losses in the current MSA product is equivalent to the total snow coverage over land. The actual data losses will be somewhat lower since MSA provides albedo values above snow covered surfaces under certain conditions: snow in forest stands, especially when viewed under large satellite zenith angles, or thawing, broken or thin snow cover at the beginning and the end of the winter. However, as shown by the examples above, no MSA retrieval takes place during most of the winter in snow-rich areas.

IMS data are only available for the northern hemisphere. We do not consider this as a significant drawback for the estimation of snow-related GSA product losses, since the amount of land surfaces affected by temporary snow cover within the field-of-view of geostationary satellites is comparably small south of the equator. The largest such area (Patagonian Andes) can be roughly compared to the Alps in terms of extension and annual snow cover.

4.4 Selecting sites for future evaluation of GSA performance over snow

A number of criteria were developed in order to identify reference sites potentially suited for the evaluation of the MSA performance above snow:

➢ The local climate shall ensure sufficient snow cover (on average more than ca. 90 days per year) to allow for meaningful statistics.

➢ Satellite zenith angles shall preferably be smaller than ≤ 60° to ensure reasonable MSA pixel size (≤ ca. 5 km diameter) and atmospheric path length (≤ ca. 2 air masses) *[Capderou, 2006]*.

➢ Local landscapes shall cater for homogeneous and undisturbed snow fields over areas covering at least 3 by 3 MSA pixels (e.g. large grasslands).

> Local climates shall allow for a sufficient likelihood of clear sky conditions during snow cover periods.

> Ancillary information, e.g. from operational nearby meteorological observations, shall be available to enable the identification of cloud-free cases.

> Landmarks allowing a clear distinction between snow and clouds from visual inspection of satellite imagery shall be available in the vicinity of a reference site.

> A reference site shall preferably be covered by two geostationary instruments (e.g. 0DEG and IODC) to support analysis of anisotropy effects.

The number of areas meeting all the above criteria including the last one demanding coverage by two instruments is very limited for 0DEG and IODC: in fact, only one region in central Anatolia strictly meets all of the above criteria (see Figure 32).

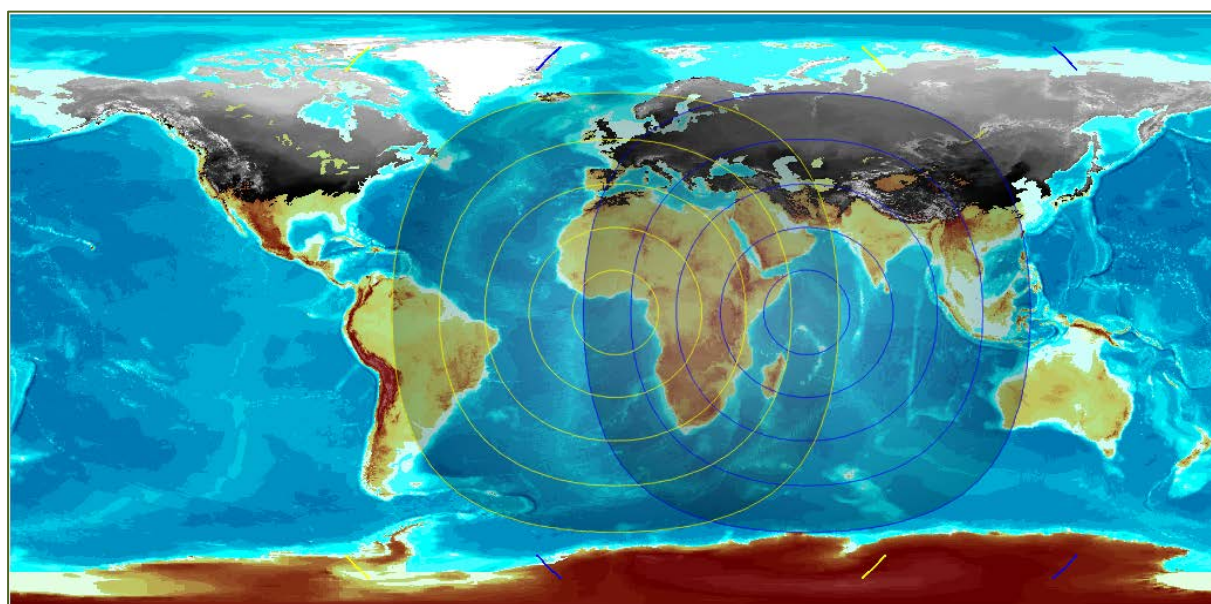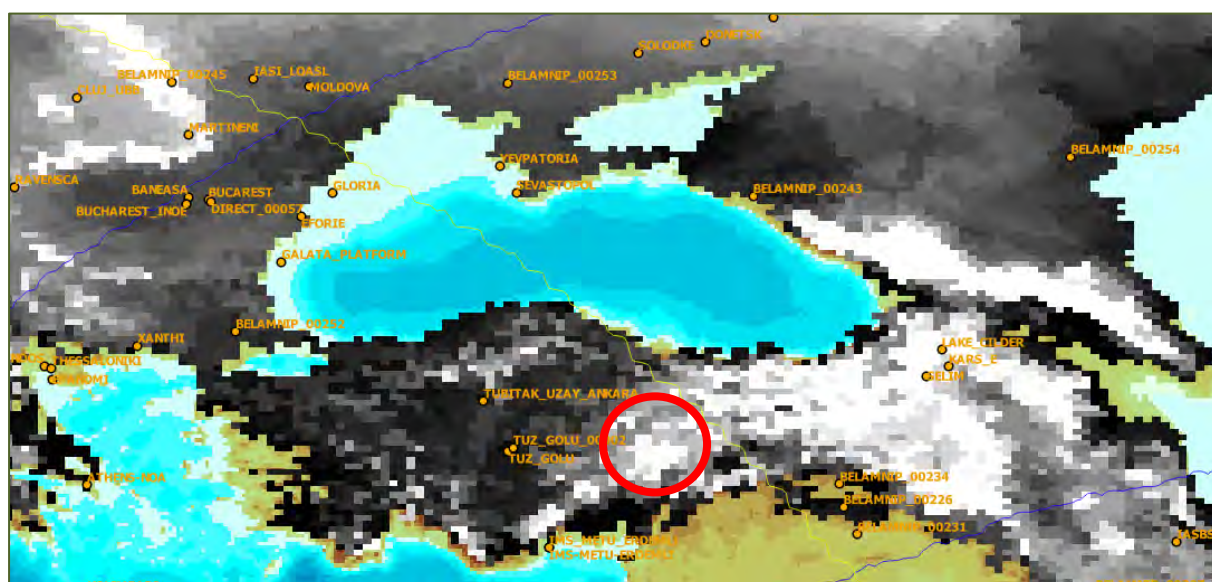**Figure 32: Days with snow cover in 2005 in the Black Sea area derived from the IMS 24 km product (transparent: no snow cover; black: 1 day snow cover; white: ≥ 120 days snow cover). Orange dots indicate GSAVALDB reference sites. The red circle indicates the only area with more than 90 days snow cover and local satellite zenith angles ≤ 60° for both 0DEG and IODC.**

Relaxing on the criterion to have the reference site covered by two instruments increases the number of potential reference sites significantly, especially in the IODC coverage (see the sites listed in Table 5). These and other sites can be identified through the GSAVALDB.

Site	Days w/ snow cover in 2005	θ_{SAT}. 0DEG	θ_{SAT}. IODC	Landscape
MARTINENI (Romania)	96	58.8°	61.0°	Mountain basin, agriculture
LAKE_CILDER (Turkey)	142	64.5	49.5	High plain, grassland, big lake
ADAMOWKA (Russia)	158	80.4	59.3	Agriculture
LAKE_SONG_KUL (Kyrgyzstan)	259	87.7	51.8	High plain, grassland, big lake

Table 5: Selection of sites suitable for studying the performance of MSA above snow.

One example of an area that appears well suited for MSA snow performance analyses is located in Russia near the southern end of the Ural Mountains (Figure 33). The site "ADAMOWKA" listed in Table 5 is located in this area. The final selection of sites for MSA analysis should be made using the IMS 4km product offering a spatial resolution comparable to MSA. The IMS 4km product is available since February 2004, while the IMS 24 km product is available since February 1997.

Figure 33: Southern end of Ural Mountains, Orenburg district, Russia. MODIS L1B image from 23. January 2005, 07:05 UTC[16]. A number of landmarks allow distinction between snow and clouds with good accuracy from visual inspection. Snow cover for more than 150 days in 2005. Often clear sky

---

[16] http://modis-atmos.gsfc.nasa.gov/IMAGES/MOD02/GRANULE/2005_01_23/023.0705.rgb143.jpg

conditions. Operational meteorological stations nearby. Only IODC coverage. The star indicates the approximate location of reference site ADAMOWKA.

4.5   Snow optical properties

The optical properties of snow in its various forms of appearance have been extensively studied. A non-exhaustive literature review covering more than forty scientific articles and technical reports published between ca. 1950 and 2014 has been conducted in the context of this study. Thirty-two of the screened documents describe in situ measurements of snow surface optical properties, predominantly located in the arctic regions of both northern and southern hemisphere:

> Arctic: 14, of which 7 on Greenland Summit,

> Antarctic: 7,

> Europe and Asia: 7 (Finland, France, India, Japan, Russia, Turkey),

> North America: 4.

The following subsections describe the optical properties of snow using a number of representative observations. It can be concluded that snow, especially fresh snow, is among the surface types with best known reflective properties and is as such highly suitable to be used for MSA validation above bright surfaces.

4.5.1   Spectral reflectance

Snow shows a distinct spectral course with very high reflectance values (often above 0.9) in the visible and near infrared up to ca. 800 nm. Between ca. 800 nm and 1,500 nm, the reflectance drops to very small values of about 0.05 and below. Beyond 1,500 nm, snow reflectance remains generally low and only for very dry snow may reach values above 0.2 at wavelengths around 1,800 and 2,200 nm (see Figure 34).
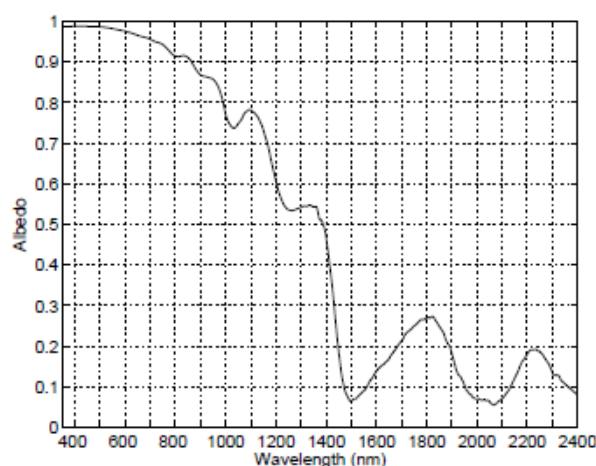
Figure 34: Spectral albedo of the snow surface at Dome C (Antarctica), measured between 23:00 and 23:30 LST on 30. December 2004 under an overcast sky. Source: *Hudson et al. [2006].*

4.5.2   Physical and chemical factors affecting snow albedo

Snow reflectance decreases with increasing water content, grain size and impurity concentration. Figure 35 shows the temporal evolution of a thawing snow surface in Finland with particularly low albedo values due to large grain size and high water content because of intense melting, combined with high soot concentrations resulting from the transport of polluted air into the area of interest.
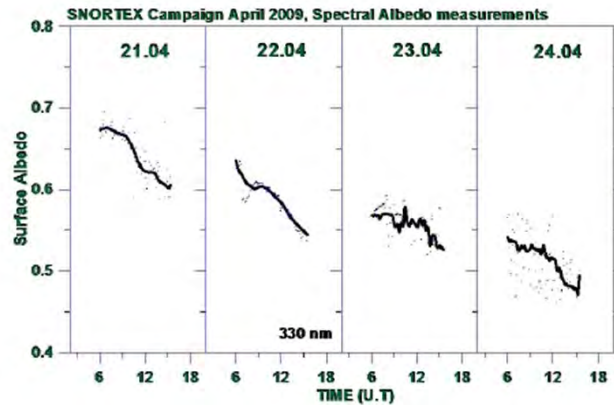
Figure 35: Snow albedo at 330 nm taken during the SNORTEX campaign in Sodankyla (Finland) between 21 and 24 April 2009. Source: *Meinander et al. [2013].*

Ice generally shows a lower reflectance than snow. This applies to glacier ice, lake ice as well as sea ice (see e.g. Figure 36).
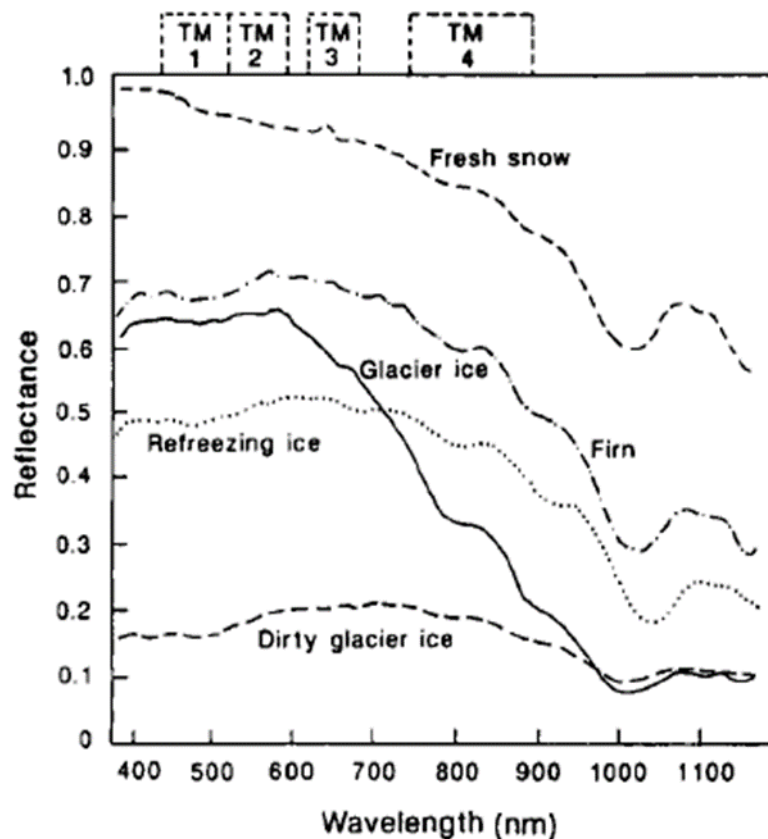
Figure 36: Spectral reflectance curves for snow and ice in different formation stages. Source: *Winther [1993]*, modified from *Zeng et al. [1984]*.

4.5.3 Snow anisotropy

Depending on snow morphology, observation geometry and wavelength, snow surfaces may show strong non-isotropic behaviour. Figure 37 taken from *Painter and Dozier [2004]* provides an example of the hemispherical-directional reflective properties of snow at six wavelengths between 0.55 µm and 2.25 µm. The investigated surface is characterised by significant forward scattering at the given solar zenith of $\theta_{SOL} = 47.3°$.
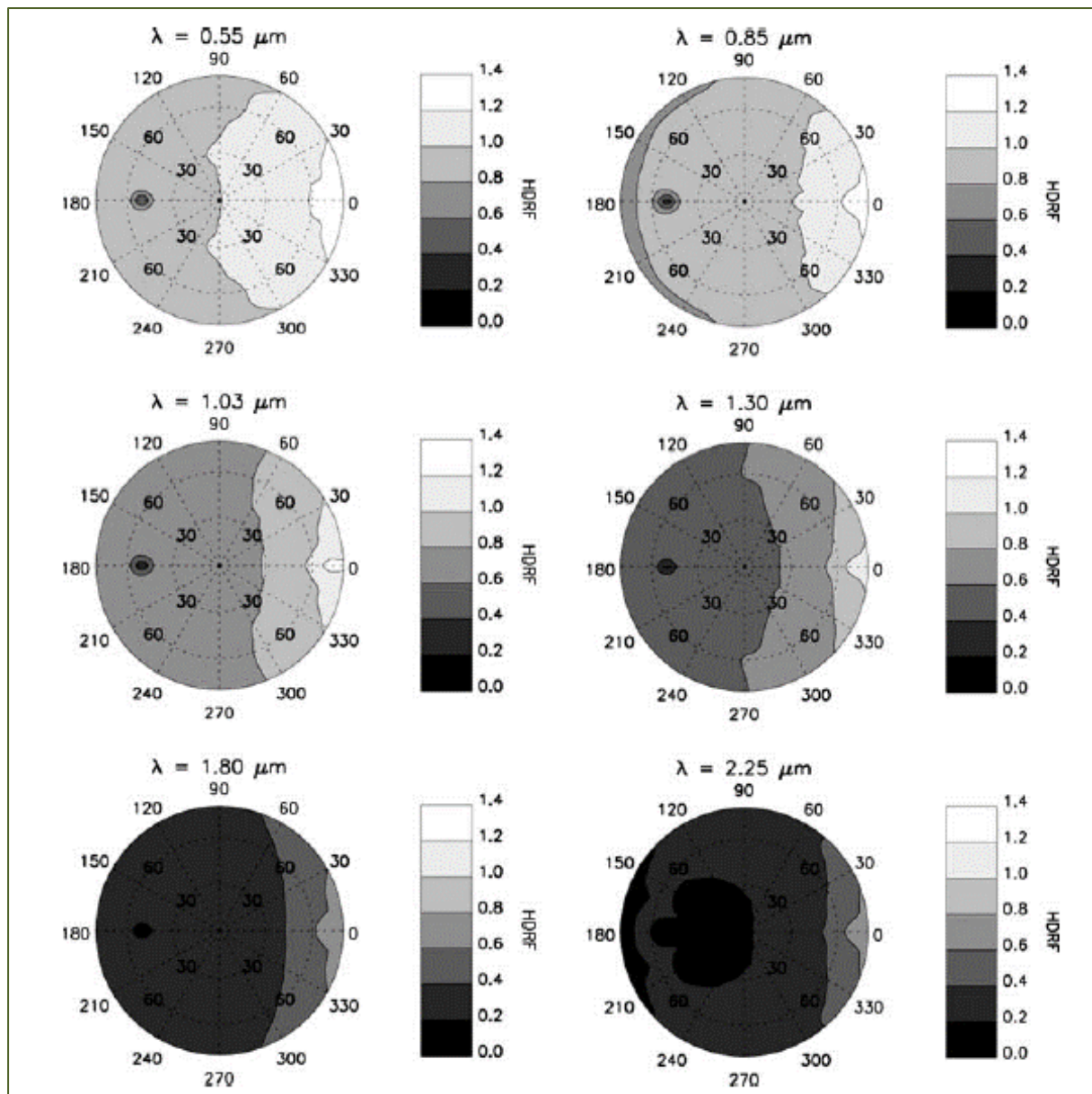
Figure 37: Polar plots of the hemispherical-directional reflectance factor (HDRF), relating the downwelling irradiance (diffuse and direct components) to the upwelling radiance *[Schaepman-Strub et al., 2006]*, for six wavelengths between 0.55 µm and 2.25 µm. Measurements acquired on 23 February 2001 in Sherwin

Meadows, Mammoth Lakes, California, US at a solar zenith angle of 47.3°. An azimuth angle of 0° represents forward scattering. Source: *Painter and Dozier [2004]*.

The anisotropy of snow reflectance triggers significant diurnal courses of the surface albedo (see Figure 38). A key factor here is apparently the structure of the snow surface, shaped and modified e.g. by wind effects.

C. April 2003-2008, Ny-Ålesund, Spitsbergen
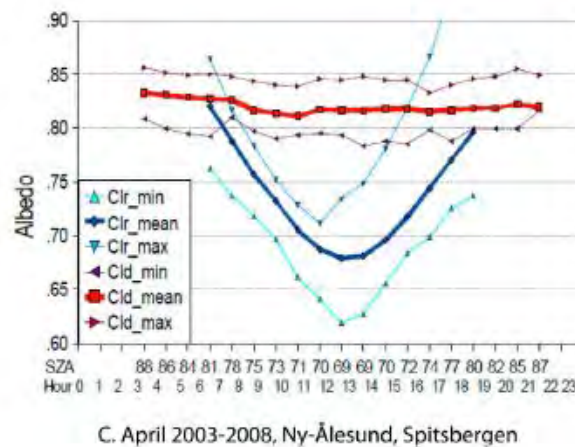
Figure 38: Mean diurnal cycle of snow albedo and air temperature for clear sky (13 cases) and cloudy sky (17 cases) at Ny Alesund, Spitsbergen, Norway, in April 2005 [*Wang and Zender, 2011*].

4.6 Spectral-to-broadband conversion for snow and other surface types

4.6.1 Approach for spectral-to-broadband conversion

MVIRI is not optimally suited to derive the broadband albedo as its spectral response function only covers parts of the visible and near infrared as shown in Figure 39.
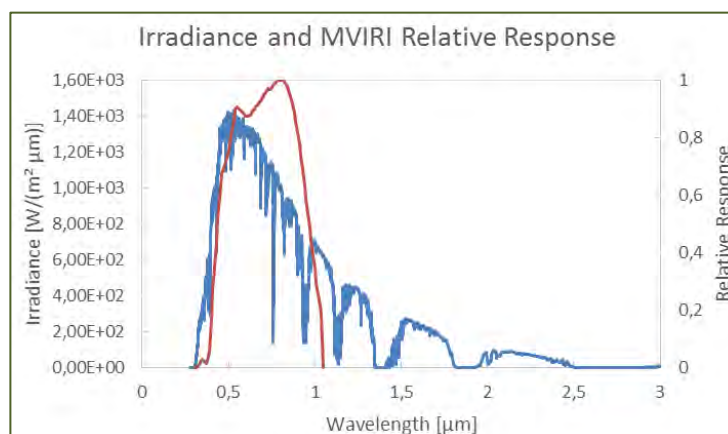
Figure 39: Spectral irradiance on the surface for an air mass of 1.5 (blue) as well as the relative spectral response of MVIRI on Meteosat-7 (red).

Data on the relative spectral response function of Meteosat 7 MVIRI VIS were obtained from the EUMETSAT website (see Figure 39).[17] The solar irradiance spectrum at the surface also shown in Figure 39 has been taken from the *American Society for Testing and Materials* (ASTM) Terrestrial Reference Spectra for Photovoltaic Performance Evaluation[18] and represents the following conditions:

➢ 1976 U.S. Standard Atmosphere specified for 33 vertical layers,

➢ rural aerosol,

➢ absolute air mass of 1.5 (equivalent to a solar zenith angle of 48.19°),

➢ Angstrom turbidity (base e) at 500 nm of 0.084,

➢ total column water vapour equivalent of 1.42 cm,

➢ total column ozone equivalent of 0.34 cm,

➢ "Light Soil" spectral surface albedo from the ASTER Spectral Library (see section 4.6.2.

Govaerts et al. [2006] developed an approach to estimate the broadband albedo between 0.3 µm and 3.0 µm from the MVIRI VIS albedo for a large variety of different surface types. The conversion is based on a 3-rd order polynomial:

$$y = ax^3 + bx^2 + cx + d, \qquad (22)$$

where y corresponds to BHR_ISO_BB or DHR_30_BB and x to BHR_ISO_VIS or $DHR\_30\_VIS,$ respectively. Different polynomial coefficients a to d are required for the different Meteosat satellites. *Loew and Govaerts [2010]* have subsequently provided updated coefficients minimising temporal inconsistencies between the different MVIRIs (Table 6).

Table 6: Polynomial coefficients for the conversion of the albedo in the MVIRI VIS channel to the broadband albedo. Copied from *Loew and Govaerts [2010]*.

---

[17] http://www.eumetsat.int/website/home/Data/Products/Calibration/MFGCalibration/index.html

[18] http://rredc.nrel.gov/solar/spectra/am1.5/#about

satellite	channel	a	b	c	d
2		7.43798614e-01	-8.48408699e-01	9.81895685e-01	-2.85976712e-05
3		9.11732554e-01	-1.07471538e+00	1.09896255e+00	-2.85976712e-05
4	$BHR_{iso,bb}$	6.47315860e-01	-6.55005634e-01	1.00361478e+00	-2.85976712e-05
5		7.47902989e-01	-7.66418219e-01	1.04928327e+00	-2.85976712e-05
6		9.98916626e-01	-1.13301563e+00	1.15992260e+00	-2.85976712e-05
7		7.00615168e-01	-6.88233614e-01	1.03751910e+00	-2.85976712e-05
2		1.27798259e+00	-1.45464587e+00	1.22636437e+00	-2.95364443e-05
3		1.25365901e+00	-1.52968502e+00	1.32036722e+00	-2.95364443e-05
4	$DHR_{30,bb}$	8.96015048e-01	-1.07426369e+00	1.22655797e+00	-2.95364589e-05
5		8.89843404e-01	-1.09384084e+00	1.25341415e+00	-2.95364443e-05
6		1.05711114e+00	-1.31526375e+00	1.30573940e+00	-2.95364443e-05
7		9.00940299e-01	-1.11476350e+00	1.26273489e+00	-2.95364589e-05

In the following, it shall be investigated how well the spectral-to-broadband conversion works for snow and other surfaces. Note that surface types with an albedo above 0.6 were not considered in *Govaerts et al. [2006]* as well as *Loew and Govaerts [2010]*.

4.6.2 Performance of the spectral-to-broadband conversion for snow and other surfaces

Calculating the broadband albedo using the generalised polynomial approach described in section 4.6.1 leads to errors that depend on the spectral reflectance of the individual surface type: The more the albedo spectrum of a particular surface type differs from the "average" spectrum represented by the polynomial coefficients a to d, the larger become the errors in the estimated broadband albedo.
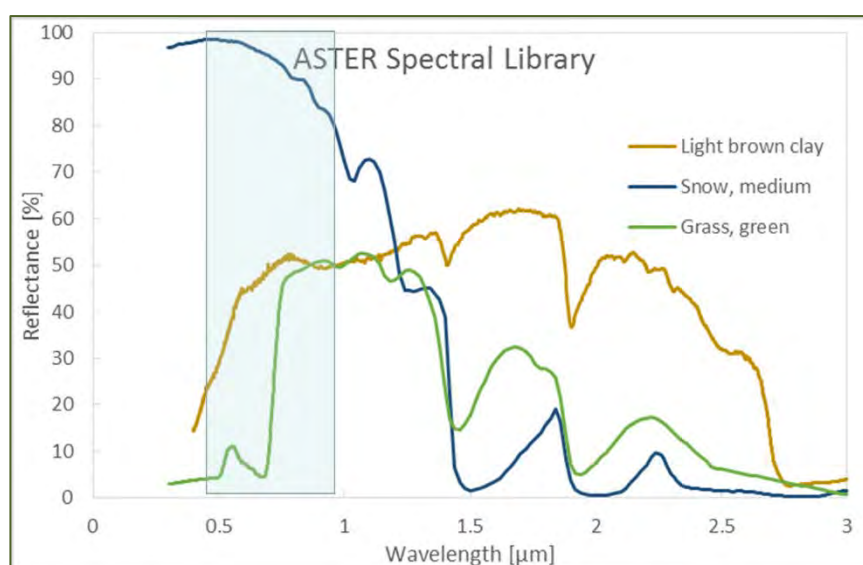
Figure 40: Spectral reflectance of medium granular snow, grass and light yellowish brown clay taken from the ASTER Spectral Library. The half width of the MVIRI VIS channel is indicated by the light blue transparent area.

The spectral reflectance of snow and frost differs significantly from other natural surface types as it shows higher reflectance in the visible and near infrared up to about 1.2 µm, as well as lower reflectance in the SWIR from about 1,5 µm than most other natural surfaces (see Figure 40). This

should lead to significant deviations when applying Equation (18) with the coefficients from Table 6, the latter being derived for an "average" surface type. In order to quantify this effect, the following procedure was applied:

➢ First, the effective albedo in the Meteosat 7 MVIRI VIS spectral channel was calculated for twelve different surface types from the ASTER spectral library[19] *[Baldridge et al., 2009]*, four of which representing various forms of snow and frost, four representing bare soils, and four representing different vegetation cover.

➢ Broadband albedo values were calculated from the MVIRI VIS channel albedos using the recommended procedure for calculating MSA broadband albedo values described in section 4.6.1.

➢ Finally, such determined broadband albedos were compared to reference values of the broadband albedo calculated directly by integrating albedo and irradiance spectra over the spectral range 0.3 to 3.0 µm.

Two different irradiance spectra have been used to represent the spectral distribution of the incoming solar radiation for clear sky (ASTM G173-03, direct plus circumsolar) and overcast conditions (ASTM G173-03, diffuse) when calculating DHR_30 and BHR_ISO, respectively.
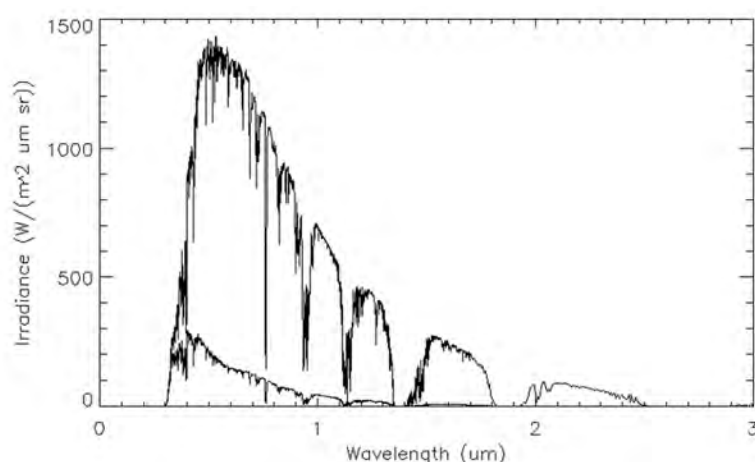
Figure 41: Irradiance spectra used to calculate DHR_30 and BHR_ISO from surface reflectance spectra. Top: ASTM G173-03, direct plus circumsolar; bottom: ASTM G173-03, diffuse.

Calculating the spectral (ρ_VIS) and broadband (ρ_BB) albedo by integrating over the respective spectral ranges, one obtains the results shown in Table 7, graphically represented in Figure 42.

Table 7: Surface albedo in the MVIRI VIS channel (ρ_VIS), derived broadband black sky (DHR_BB) as well as white sky (BHR_BB) albedos for different surface types from the ASTER spectral library. The reference broadband surface albedo (ρ_BB) is provided in the rightmost column.

---

[19] http://speclib.jpl.nasa.gov/

Name of surface in ASTER Library	Inc. irrad.	ρ_VIS	DHR_BB	BHR_BB	ρ_BB
Dark reddish brown fine sandy loam	E0_DIF	0.224		0.206	0.199
Dark reddish brown fine sandy loam	E0_DIR	0.258	0.267		0.300
Light yellowish brown clay	E0_DIF	0.399		0.349	0.332
Light yellowish brown clay	E0_DIR	0.433	0.411		0.437
White gypsum dune sand	E0_DIF	0.717		0.648	0.584
White gypsum dune sand	E0_DIR	0.747	0.696		0.660
Grey/dark brown extr. stoney coarse sandy	E0_DIF	0.092		0.090	0.091
Grey/dark brown extr. stoney coarse sandy	E0_DIR	0.113	0.130		0.160
Dry grass	E0_DIF	0.375		0.329	0.329
Dry grass	E0_DIR	0.418	0.399		0.447
Grass	E0_DIF	0.178		0.167	0.167
Grass	E0_DIR	0.228	0.240		0.254
Conifer	E0_DIF	0.185		0.173	0.170
Conifer	E0_DIR	0.235	0.247		0.249
Deciduous	E0_DIF	0.199		0.184	0.187
Deciduous	E0_DIR	0.251	0.261		0.276
Frost	E0_DIF	0.983		1.020	0.960
Frost	E0_DIR	0.978	1.012		0.885
Fine snow	E0_DIF	0.973		1.003	0.942
Fine snow	E0_DIR	0.965	0.989		0.844
Coarse granular snow	E0_DIF	0.929		0.931	0.885
Coarse granular snow	E0_DIR	0.909	0.904		0.745
Medium granular snow	E0_DIF	0.951		0.967	0.912
Medium granular snow	E0_DIR	0.937	0.945		0.787

As can be inferred from Figure 42, the spectral-to-broadband conversion works rather well for all investigated vegetation types and equally for most bare soil types, except for the very bright white gypsum sand where larger deviations are observed. Deviations are generally larger for the black sky than for the white sky albedo. The largest discrepancies between retrieved and true broadband albedo are observed for the various forms of snow and frost, here again more prominently affecting the black sky albedo, which is significantly overestimated.
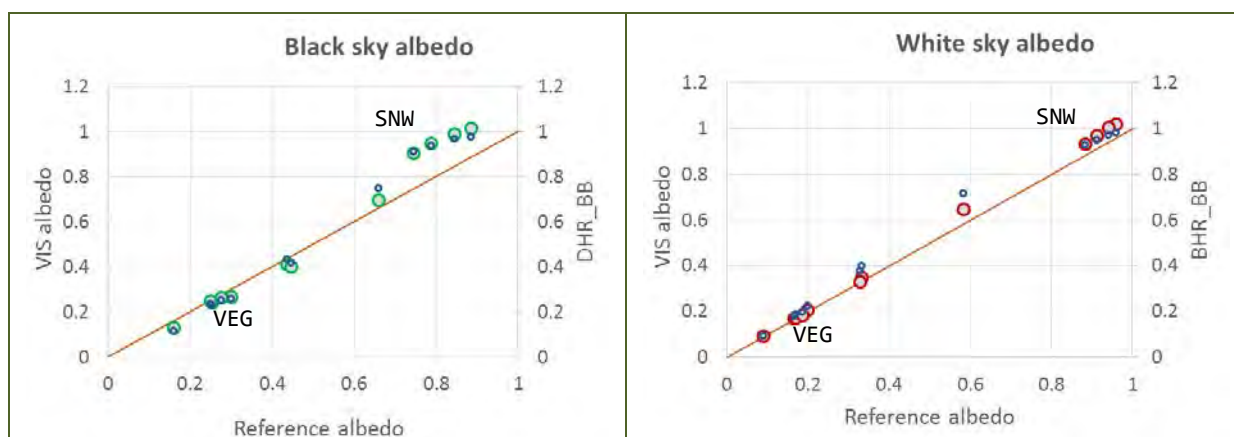
Figure 42: Reference ("true") broadband albedo *vs*. albedo in the MVIRI VIS channel (small circles) as well as derived MSA broadband albedo (large circles). Left: black sky albedo (DHR_30_BB); right: white sky albedo (BHR_ISO_BB). Different types of vegetation (VEG) and snow (SNW) cluster in narrow ranges.

Table 8: Relative and absolute differences between MSA broadband albedo values and the corresponding reference albedo values for three surface types.

Surface	Snow, medium	Grass, green	Clay, light brownish
DHR_30_BB	0.945	0.240	0.411
ρ_DIR_BB (reference)	0.787	0.254	0.437
$\Delta\ DHR\_30\_BB$	+0.158	-0.014	-0.026
$\delta\ DHR\_30\_BB$	+20%	-6%	-6%
BHR_ISO_BB	0.967	0.167	0.349
ρ_DIF_BB (reference)	0.912	0.167	0.332
ΔBHR_ISO_BB	+0.055	±0.0	+0.017
δBHR_ISO_BB	+6%	±0%	+5%

4.7 Conclusions and recommendations

The following conclusions and recommendations can be drawn from the analysis of the availability and potential GSA performance above snow.

Conclusions:

➢ As a consequence of the cloud screening applied, no MSA retrieval is attempted for most snow-covered surfaces. This leads to severe data gaps, amounting to 50% and more in certain areas of Eurasia and North America.

➢ However, snow surfaces are generally well studied which makes then suitable as well characterized bright surface reference targets.

Recommendations:

➢ The MSA retrieval should also be attempted in the case of (assumed) cloud cover. This would provide the information required to study the GSA performance above snow in more detail.

➢ The cloud mask could be provided as an independent data layer. This way, potentially cloud covered pixels could still be masked after the retrieval parameters have been obtained.

➢ It should be considered delivering GSA with an additional (external) information layer on snow cover. This would allow users to comfortably fill many of the GSA data gaps.

➢ A dedicated spectral-to-broadband conversion should be considered for snow, especially for DHR_30. Alternative methods to estimate the broadband spectral albedo of snow should be investigated.

➢ The performance of the spectral-to-broadband conversion should be re-assessed for bright surfaces types other than snow.

5. Probabilistic temporal stability characterization of GSA (Task 5)

5.1 Expected outcome

The expected outcome [of Task 5] is a statistically significant estimate of the temporal stability of the GSA data record in different regions of the data coverage, respective biome types.

5.2 Method

Assessing the temporal stability of a satellite climate data record, such as provided by the GSA method, is a challenging task. It requires either the knowledge of temporally stable reference targets or sites providing accurate reference data over longer time periods of appropriate size. Criteria and an approach for the identification of such sites have been provided in section 2.

The GCOS requirement for the temporal stability of surface albedo (white-sky and black-sky albedo) was originally defined as $MAX \{1\%, 0.0001\}$ *[GCOS, 2011]*. During the ALBEDOVAL-1 study, an inconsistency within that definition has been identified as it was shown that the 0.0001 stability criterion in practice never applies. The modified GCOS requirement as defined in the SoW for the present study was therefore used, which is defined as $MAX \{1\%, 0.0005\}$.

In this context, the following questions need to be addressed:

➢ What is the temporal stability of the MSA record in different regions?

➢ What is the probability that the GCOS criteria for temporal stability are met?

➢ Under which conditions are the GCOS temporal stability criteria (not) met?

➢ Can systematic temporal inconsistencies be identified in the MSA record?

To answer these questions requires a thorough assessment of the MSA dataset and the application of a strict framework of definitions and statistical tools to ensure maximum traceability in the estimates of the temporal stability criteria.

5.3 Theoretical background

Defining the accuracy and stability of the MSA data product requires a comparison with corresponding reference data, collocated in space and time. Let $\{x_1 \pm \delta x_1, x_2 \pm \delta x_2, \ldots, x_n \pm \delta x_n\}$ denote a time series of the MSA surface albedo with n measurements and let $\{v_1 \pm \delta v_1, v_2 \pm v_2, \ldots, v_n \pm \delta v_n\}$ be a collocated time series of validation (reference) data. The bias b between the two datasets is then defined as the mean discrepancy, which is given as *[Merchant, 2013]*

$$bias = b = \frac{1}{n}\sum_{i=1}^{n}(x_i - v_i) = \bar{x} - \bar{v}. \tag{23}$$

The temporal stability β is defined as the change in bias b over a predefined time period Δt as *[Merchant, 2013]*

$$bstability = \beta = \frac{db}{dt} = \frac{b(t + \Delta t) - b(t)}{\Delta t} = \frac{d\bar{x}}{dt} - \frac{d\bar{v}}{dt}. \tag{24}$$

Thus, the stability is dependent on the timescale chosen for its analysis. In the ideal case, the stability would be zero over any timescale. In the Earth observation context, the stability can display long-term trends or periodicity which result from factors such as sensor or satellite drift, changes in the solar constant as well as changes of e.g. algorithms or auxiliary data, like can be observed e.g. in reanalysis datasets.

5.3.1 Absolute temporal stability

The calculation of β requires the knowledge of temporal changes in the surface albedo $\rho(t)$ as well as a time series of collocated validation data $v(t)$. The sites identified in section 2 are used for the temporal stability analysis. In general these might be categorized in the following groups:

➢ Sites with ancillary reference data: $\Delta v/\Delta t$ is known.

➢ Sites for temporal stable targets: $\Delta v/\Delta t = 0$.

For both cases, the GSA bias b can be estimated using (23).

The temporal stability can be estimated as the slope of a linear regression for the bias over time, which is given as

$$b(t) = \alpha + \beta t \tag{25}$$

over a predefined time period Δt. The unknown slope and intercept are obtained using a standard *Ordinary Least Square* (OLS) approach by minimizing

$$\chi^2(a, b) = \sum_{i=1}^{N} \left(\frac{b_i - \hat{\alpha} - \hat{\beta} t_i}{\sigma_i{}^2} \right)^2, \tag{26}$$

where $\hat{\alpha}$ and $\hat{\beta}$ are (uncertain) estimators for the unknown model parameters (α, β) in (25). Note that this approach deviates from a standard linear regression approach which typically assumes unit variance ($\sigma_i{}^2$) for uncertainties of the dependent variable y. As $\sigma_i{}^2$ is dependent on the uncertainties of the individual GSA retrievals, this approach allows to fully exploiting the uncertainty information provided together with the product.

5.3.2 Relative temporal stability

The relative temporal stability γ is defined as

$$\gamma = \frac{\hat{\beta}}{\rho_{ref}} \cdot 100 \ [\%], \tag{27}$$

where ρ_{ref} corresponds to the reference albedo value for the particular location investigated. For a robust estimation of ρ_{ref}, the median value is used in this study.

5.3.3 Robust estimation of the temporal stability

To estimate the temporal stability parameter β, two alternative methods were used:

➢ *Ordinary Least Square* (OLS),

➢ *Weighted Least Square* (WLS).

The OLS approach is the standard approach to fit a statistical model to data. It has already been successfully used in various surface albedo validation studies, including the previous ALBEDOVAL-1 study *[Fell et al., 2012]*. While OLS is widely used, it is also well known that results are sensitive to outliers. A major advantage of the MSA dataset is that it provides quantitative uncertainty information on a per pixel basis. In order to exploit this additional uncertainty information, a weighted least square approach is applied as well.

The MSA uncertainty information is provided in a separate field (DHR_30_ERROR) and corresponds to the error of the DHR_30 product obtained from error propagation (for details see *Govaerts and Lattanzio [2007]*. This error estimate is valid for the retrieval product, which is the spectral albedo. To use the uncertainty information each sample can be weighted by the inverse of its uncertainty variance. This is done through a *Weighted Least Square* (WLS) regression approach. For the WLS regression approach, information of the broadband surface albedo uncertainty is required for both DHR_30 and BHR_ISO.

However, as uncertainty information is currently only available for the (spectral) DHR_30 product, the following assumptions are made to be able to take into account the uncertainties of the individual MSA data samples:

➢ DHR_30 uncertainty is assumed to be equal to BHR_ISO uncertainty.
➢ The uncertainty in the spectral albedo is assumed to be identical to the broadband albedo uncertainty[20].

It needs to be emphasized that the BHR_ISO uncertainty can in principle be reconstructed from the data product. Details can be found in the MSA Product User's Manual *[EUMETSAT 2014-B]*.

5.3.4 Probability of meeting the GCOS criteria

For both the OLS and WLS estimators, the uncertainties of the slope parameters ($\sigma_{\beta,OLS}, \sigma_{\beta,WLS}$) are obtained. The distribution of β is hereby following a Student-t distribution and allows for the calculation of the probabilities of the slope parameter.

The GCOS requirement for the temporal stability of the surface albedo (white sky and black sky) was originally defined as *[GCOS, 2011]*:

$$|\beta| \leq \mathrm{MAX}\,\{1\%, 0.0001\}. \tag{28}$$

---

[20] This assumption is not entirely true due to the nonlinear transformation from spectral to broadband albedo. However, the relative weighting of the samples is still assumed to be in the right relative order.

As discussed before (section 5.2), a revised criterion is used herein which is defined as:

$$|\beta| \leq \text{MAX}\{1\%, 0.0005\}. \tag{29}$$

For each reference site, the two slope parameters and their respective uncertainties ($\beta_{OLS} \pm \sigma_{\beta,OLS}, \beta_{WLS} \pm \sigma_{\beta,WLS}$) are obtained. The probability P that the GCOS stability criterion is met for a particular reference site can then quantified as

$$P\{|\beta| < \tau\}, \tag{30}$$

where τ is a significance threshold. The probability of the parameter is estimated using standard parameter uncertainty estimates for linear regression analysis. A value of $\tau = 0.05$ is used throughout the study. For each site, the probability that either the absolute or relative GCOS criteria is met is reported. Figure 43 shows an example of the cumulated PDF of $|\beta|$ for a selected test site as well as the probabilities of meeting the GCOS criteria.
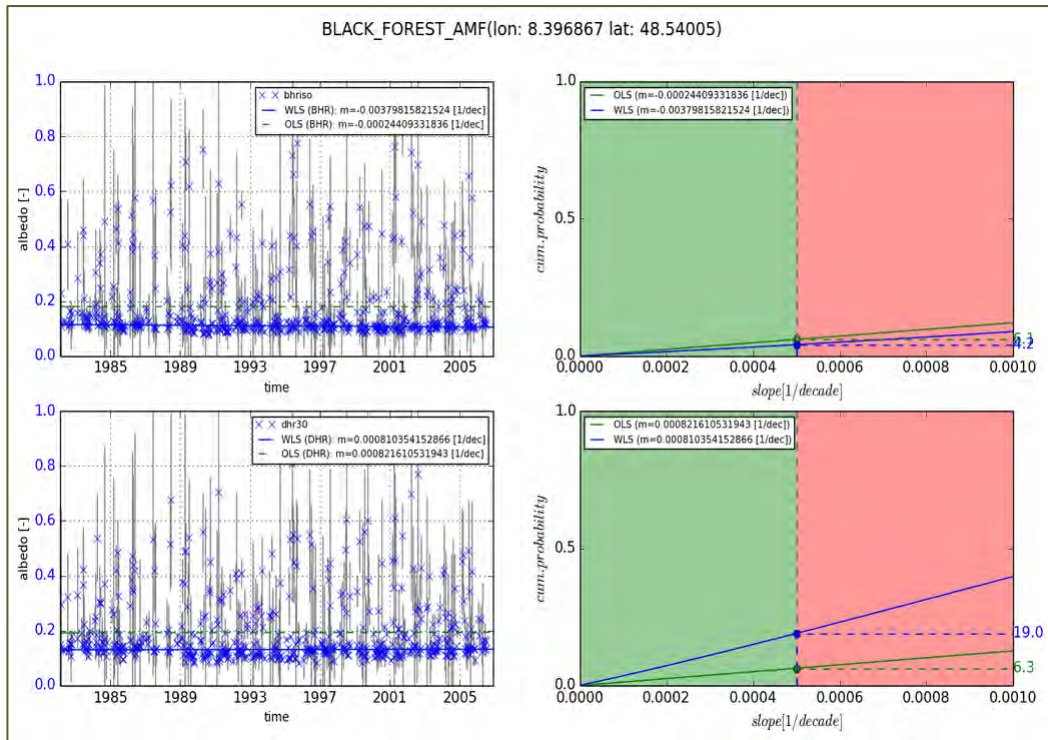
Figure 43: Probability of meeting the GCOS temporal stability criteria for site `BLACK_FOREST_AMF`. Left: Time series of individual retrievals. The uncertainty bars indicate the 1σ standard deviation for individual retrievals as reported in the MSA product. Right: Cumulative probability of temporal slope parameter (β), indicating the probability of meeting the GCOS criteria.

5.3.5 Temporal stability tests

The MSA product provides the bidirectional hemispherical reflectance (BHR_ISO) and the directional hemispherical reflectance (DHR_30). The temporal stability analysis is done for both variables as well as for the 0DEG and IODC coverages and using the two different regression approaches as described

above. This can lead to a maximum of 16 different stability values[21] for a location that is covered by both MSA geometries (0DEG, IODC). In addition, the relative and absolute GCOS criteria are tested.

5.4 Results and discussions

5.4.1 Location of sites meeting GCOS criteria

Of all GSAVALDB sites, 331 were found to meet at least one GCOS criterion. These sites cover a wide range of latitudes and are located in both the 0DEG and IODC coverages (Figure 44). Out of these 331 sites, 148 correspond to locations that were preselected in the GSAVALDB as sites suitable for GSA validation, which corresponds to a fraction of ca. 23% of the 652 potential validation sites identified in section 2.5.3. The remaining 183 sites were not part of the preselected locations, indicating that less homogeneous sites often also show a good long-term temporal stability.
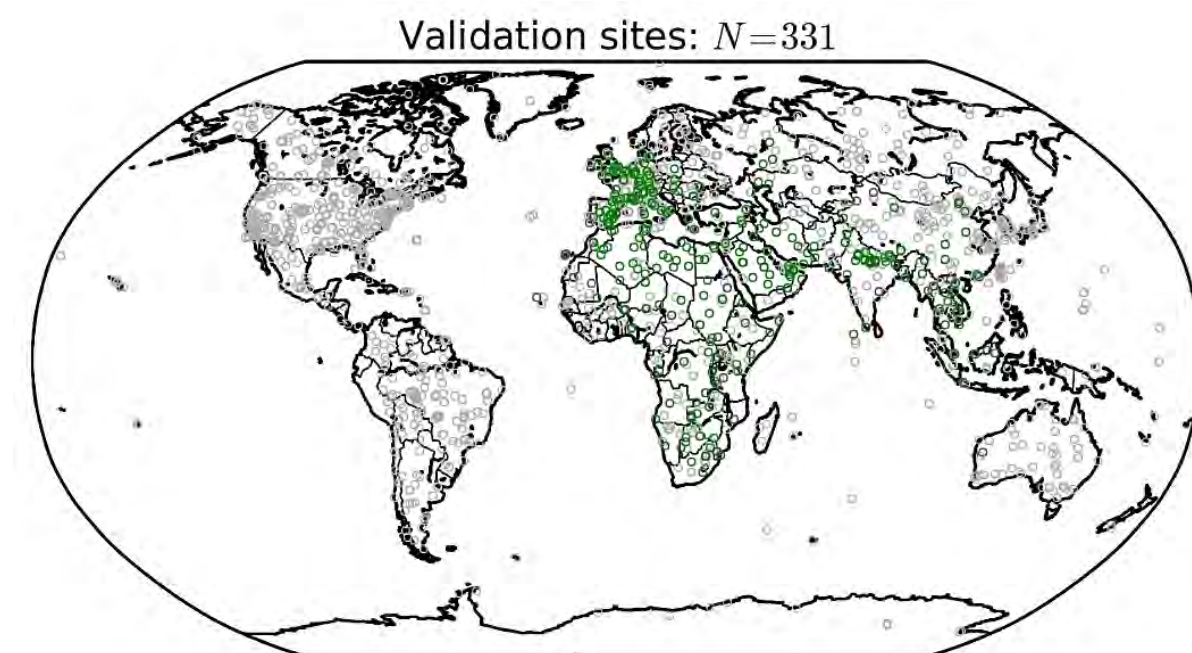
Figure 44: Map showing GSAVALDB sites meeting at least one GCOS criterion. Sites covered by the MSA product are shown in green.

5.4.2 Which GCOS criteria are met?

It needs to be emphasized that none of the sites meets the absolute GCOS criteria defined in section 5.1 at a significance level of 95%, only the relative GCOS criterion is met. Nevertheless, meeting the GCOS criteria means that the probability for the temporal stability is smaller than $\tau = 0.05$. It is thus dependent on the probability threshold chosen and the quality of the uncertainty information in the GSA data product.

---

[21] 2 geometries x 2 channels (DHR_30, BHR_ISO) x 2 variables x 2 methods

Figure 45 shows the cumulated frequency distribution of the estimated long-term stability (β) for all sites where an estimation was possible. However, it was also found that the estimated probabilities for meeting this criterion were above the defined threshold. Using a more relaxed probability threshold might therefore reveal that some sites actually meet the absolute GCOS criteria.

It was therefore investigated how many sites would meet the absolute GCOS criteria without consideration of the probability threshold, as it is not part of the GCOS criteria. Results are summarized in Table 9. Overall, 42 sites would meet the revised absolute GCOS criteria if no probability threshold is applied.

Table 9: Number of stations meeting the absolute GCOS criterion for different stability thresholds of $|\beta|$, separated between DHR_30 and BHR_ISO datasets.

Method / threshold	$|\beta| = 0.0001$	$|\beta| = 0.0005$
WLS	DHR_30: 1 / BHR_ISO: 6	DHR_30: 15 / BHR_ISO: 20
OLS	DHR_30: 7 / BHR_ISO: 5	DHR_30: 26 / BHR_ISO: 16

The WLS-based results show in general lower slope values for more stations, which indicates that the incorporation of the MSA uncertainty information in general helps to obtain more robust slope estimates.
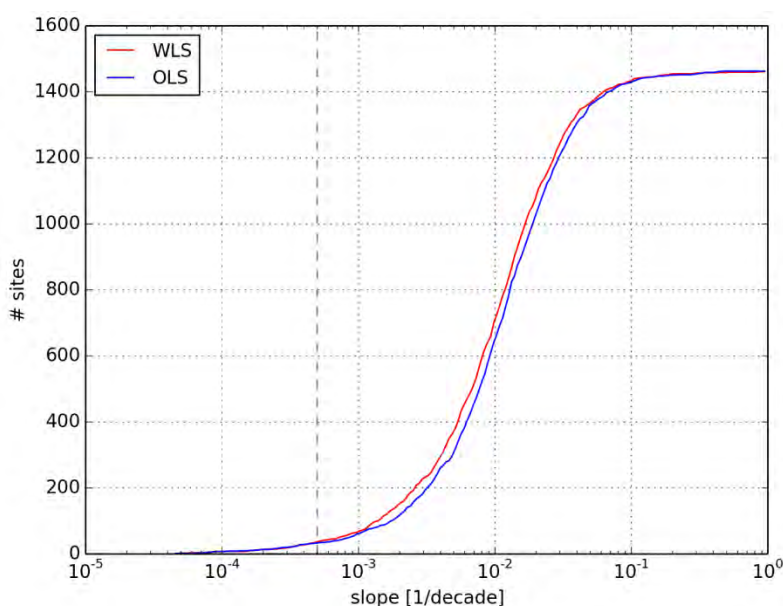
Figure 45: Cumulated frequency distribution of estimated long-term stability for all stations, using the OLS and WLS approaches. The dashed line indicates the absolute GCOS criterion.

5.4.3   Which land cover types meet the GCOS criteria?

Figure 46 shows the frequency distribution of the land cover types of the sites identified to be temporally stable. Most frequently identified land cover types are *Cropland* (#10), *Urban areas* (#190), and *Bare areas* (#200).
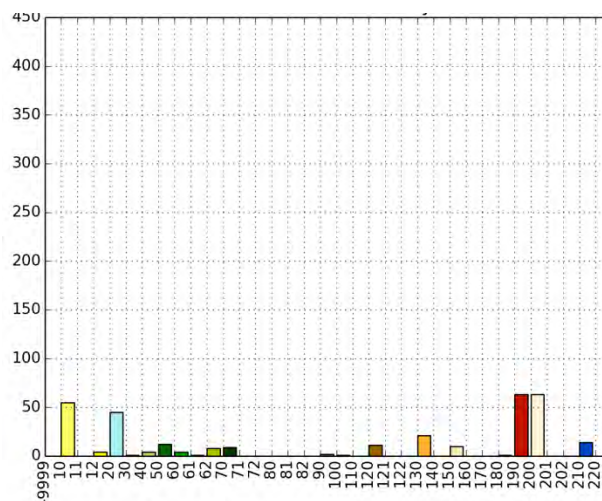
Figure 46: Frequency distribution of land cover types for all sites identified to be temporally stable (see Figure 4 for the land cover legend).

It is interesting to note that urban areas frequently show a temporally stable albedo signal. Can urban areas thus be considered as stable targets? Figure 47 shows results of the temporal stability analysis for Bejing City. Results of the WLS based stability analysis show a rather stable signal. The same is true for other larger urban agglomerations. It was thus found that large urban areas could indeed act as temporally stable reference targets. In particular, the incorporation of the MSA uncertainty information helps to apply a proper weighting to the different individual retrievals (see also section 5.5) and to thus minimise the impact of outliers (e.g. due to undetected clouds).
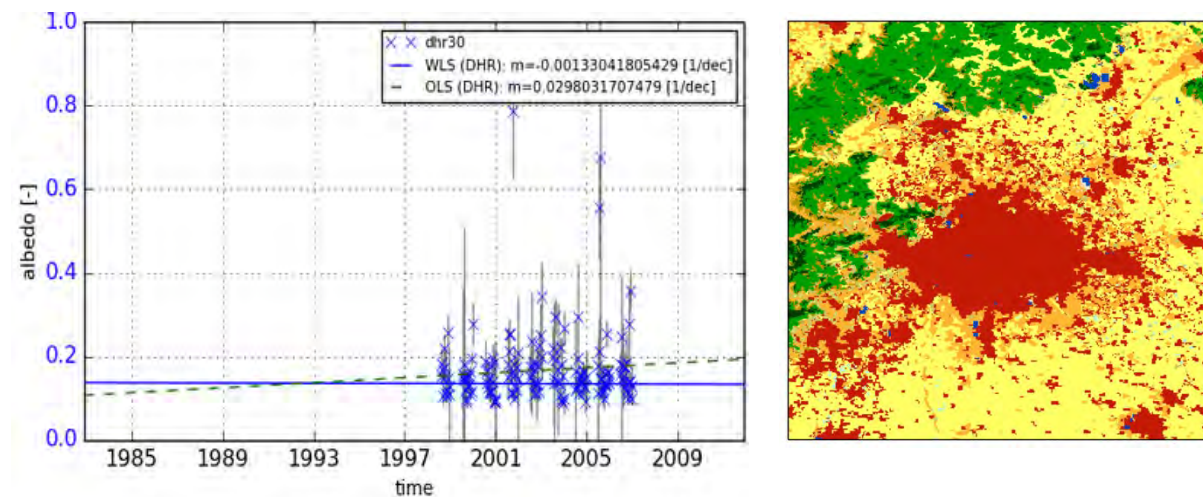
Figure 47: Temporal stability (left) and land cover map (right) for Bejing, China.

5.4.4 Do IODC and 0DEG provide consistent results?

Of the 652 pre-selected GSAVALDB sites (see section 2.5.3), 283 are situated in both Meteosat coverages (IODC, 0DEG). Table 10 summarizes how many of these sites meet at least one of the GCOS criteria for either geometry. It is found that the criteria are met for both coverages at only 15 stations, while the GCOS criteria were met for one coverage but not for the other for a total of 99 stations.

Table 10: Number of sites meeting either the absolute or relative GCOS criterion for IODC and 0DEG geometries.

GCOS met for IODC	GCOS met for 0DEG	# of cases
Y	Y	15
Y	N	41
N	Y	58
N	N	169
Sum		**283**

5.4.5   Why is the GCOS criterion not met for so many preselected sites?

In principle, one would expect that if the GSA validation sites were carefully enough selected, most of them should match the GCOS criteria if the MSA dataset as such had sufficient accuracy. However, as shown before, only a limited number of the selected sites actually seems to meet the relative GCOS criterion. It was therefore investigated why other preselected sites do not meet the GCOS criteria. It was found that MSA data show significant temporal trends in most such cases, resulting in not meeting the GCOS criteria. Reasons for this might be that either the surface conditions have changed over time, that temporal trends are mimicked by undetected clouds or that the MSA dataset itself is not sufficiently stable.

Some sample time series of sites that do not meet the GCOS criteria are shown in Figure 48. For the sites BELMANIP_197 and BELMANIP_209, one observes an increase in the surface albedo. For BELMANIP_209, the albedo values vary much more prior to 1992. In contrast, a decrease in surface albedo is observed for the site AGOUFOU. While BELMANIP_197 and BELMANIP_209 are largely dominated by bare soil, AGOUFOU is mainly covered by grassland. The decline in the surface albedo might be therefore a result of changing surface conditions at decadal timescales.

5.5   Conclusions and recommendations

No decisive conclusion on the reasons why certain sites are not meeting the GCOS criteria can be made at this point. The following conclusions and recommendations can be however made:

➢ The usage of uncertainty information provided within the MSA product helps to get a more robust estimate of the temporal stability of the MSA multi-decadal record.

➢ Revise the spectral to broadband conversion coefficients for bright targets. As the spectral to broadband conversion gets more uncertain towards larger albedo values, it is recommended to include these uncertainties in the overall pixel wise uncertainty budget of the broadband product.

➢ Incorporate the temporal variability of the NDVI temporal variance as an additional filter criterion for site selection to avoid that long-term changes in the vegetation cover affect the temporal stability analysis.
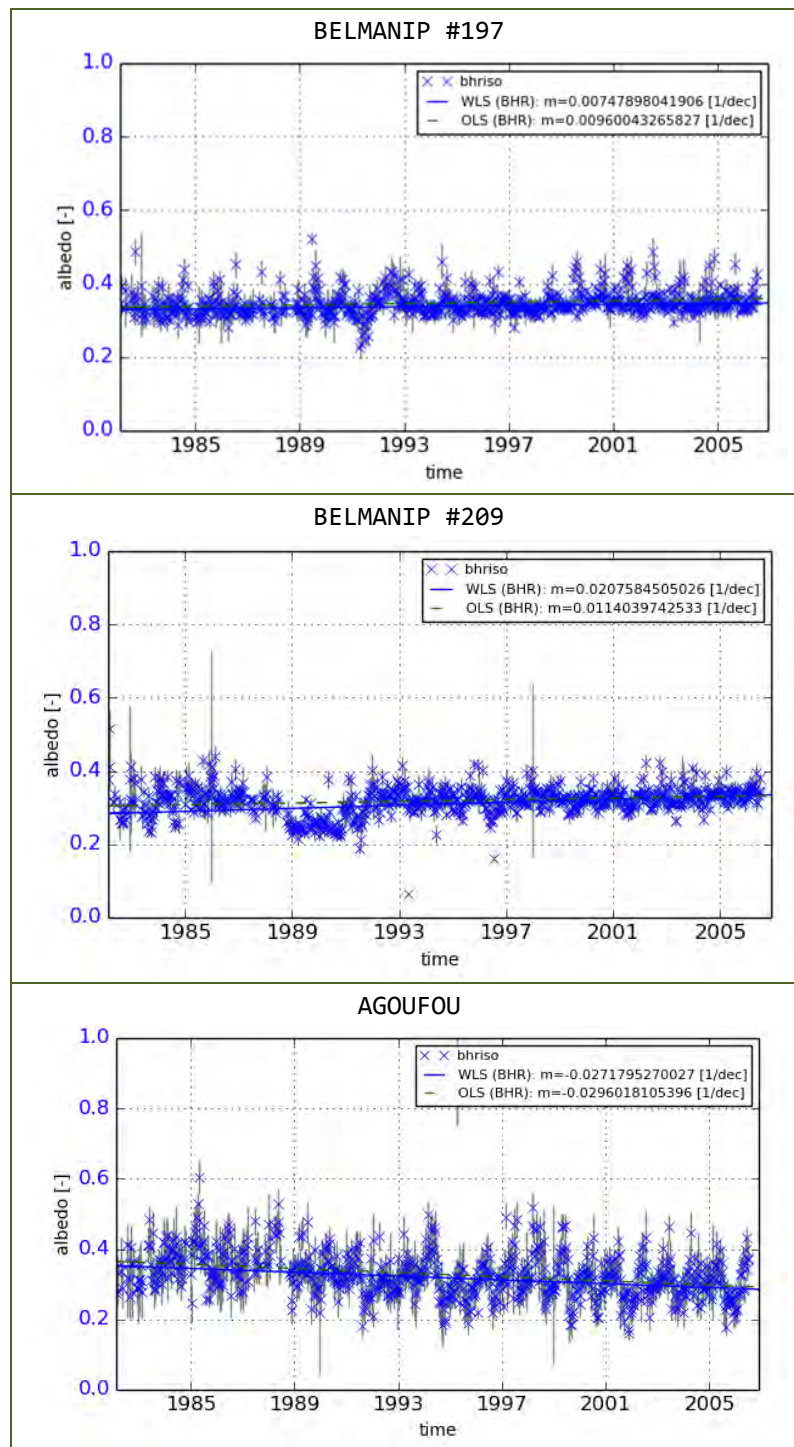
Figure 48: MSA time series at potential reference sites not meeting the GCOS criteria.

6. Comparison of MSA vs. GLASS for the pre-MODIS era

6.1 Expected outcome

The MSA product was compared to an AVHRR-derived albedo product (GLASS). The expected outcome is an assessment of the MSA quality in the pre-MODIS era.

6.2 Introduction

In order to contribute to the quality assessment of the MSA data product in the pre-MODIS era, i.e. before the year 2000, MSA values of the black sky albedo (DHR_30) and white sky albedo (BHR_ISO) were compared to the corresponding Global Land Surface Satellite (GLASS) products for specifically chosen reference sites.

While MSA is a Level-2 product, GLASS applies spatial and temporal merging and represents thus a Level-3 product. A strategy has been devised to specifically account for these differences and to ensure a meaningful comparison.

6.3 GLASS broadband surface albedo

GLASS is a suite of long-term remote sensing products covering the period 1981 to 2010 which has been produced by the *Center for Global Change Data Processing and Analysis* at *Beijing Normal University*. GLASS comprises five product classes relevant for land surface studies: Leaf area index, shortwave broadband albedo, broadband emissivity, downwelling shortwave radiation, and photosynthetically active radiation.

GLASS products are derived using two different data sources undergoing individual data processing streams: AVHRR data are used to generate the GLASS products for the period 1981 to 2000 while MODIS data are applied to the years 2000 to 2012. AVHRR- and MODIS-derived products do not only differ in terms of algorithms applied but also as regards spatial resolution, temporal composition, and geographic projection. The main characteristics of the AVHRR-based GLASS albedo products are listed in Table 11.

Table 11: Characteristics of the AVHRR-based GLASS products.

Scientific datasets	Black sky albedo White sky albedo Quality indicator
Temporal characteristics	Coverage: 18 June 1981 to 2 January 2001 Time step in data set: 8 days Interval applied to statistical temporal filtering: 33 days
Spatial characteristics	Spatial coverage: global Spatial resolution: 0.05°.
Data format	HDF 4.2.

The GLASS albedo product is well suited to contribute to the validation of the MSA, not only because it covers almost the entire MSA period, but also because of the fundamentally different approach in

product generation. Most importantly, GLASS accounts for the surface anisotropy in a different way and applies complex filtering and gap filling techniques in an attempt to enhance product quality.

GLASS surface albedo products are available free of charge through publicly accessible ftp servers, e.g. from ftp://ftp.glcf.umd.edu/glcf/GLASS/ABD/. The size of one individual file of albedo product representing one 8-days period covering the full globe amounts to ca. 30 M; the full archive of AVHRR-based surface albedo GLASS products comprises 886 individual files and amounts to ca. 26 G.

Details on the methods applied to generate the GLASS surface albedo product can be found in *Zhao et al. [2013]* and references given therein.

6.4 Site selection

For a number of reference sites, MSA albedo products have been compared to the corresponding GLASS albedo product. The sites were selected in an attempt to cover a broad range of land surface types and observation geometries while in the same time contributing to the other analyses performed in this study. In particular, we chose the following sites for further analysis

➢ BOUMBA_BEK and BELMANIP_00155, both located in the Congo basin, representing broadleaved evergreen forest, and characterized by a very high likelihood for cloud cover (also analysed through Tasks 2 and 3 herein).

➢ OMANI_DESERT and LIBYA, both representing bright desert surfaces, and characterized by very low likelihood for cloud cover (also analysed through Tasks 2 and 3 herein).

➢ BRIANSKI_LES (400 km south-west of Moscow) and KULGUNINO (Southern Ural Mountains), both representing deciduous forests in a continental climate characterized by regular and lasting snow cover.

➢ ADAMOWKA (near the south-eastern end of the Ural Mountains) and MARTINENI (south-eastern Carpathian Mountains), both representing agriculturally used land surfaces in continental climates characterized by regular and lasting snow cover (also analysed through Task 4 herein).

➢ BELMANIP_00399 (Southern Kazakhstan) and KHAUDUM (Namibia), both representing grasslands in different climates.

➢ DARK_DESERT_00001, DJEBEL_FURURI, ETOSHA_PAN1, QOZ_EL_HARR, and RED_DESERT. These sites located in arid regions have been added to cover surface albedo ranges not represented by the sites above.

Where available, MSA products from both the 0DEG and IODC observation geometries were processed. The analyses presented herein are automated to a large degree such that further sites may be added at a later stage with reasonable extra efforts.

6.5 Comparison approach

There are a number of fundamental differences between the MSA and the GLASS albedo products which need to be taken into account for a meaningful comparison:

> *Spectral characteristics:*
> While MSA provides albedo values representative of the MVIRI VIS channel, GLASS albedo products represent the broadband shortwave spectral albedo.

> *Observation conditions:*
> While the MSA black sky albedo is referenced at a solar zenith angle of 30°, the corresponding GLASS product is provided for the zenith at local solar noon.

> *Spatial resolution:*
> While MSA is given for MVIRI pixels representing ellipsoids of varying size on the Earth surface, AVHRR-based GLASS products[22] are given at a spatial resolution of 0.05°.

> *Temporal resolution:*
> While the MSA albedo products are derived consecutively from individual 10-day observation periods, the GLASS AVHRR-based albedo products are specified every 8 days but are derived from a 33-day interval using a statistics-based temporal filter based on Bayesian theory *[Liou et al., 2012]*.

Table 12: Comparison of MSA versus GLASS-AVHRR surface albedo products.

Parameter	MSA	GLASS-AVHRR
Observation geometry	Geostationary	Polar orbiting, across-track
Spectral resolution	1 channel, MVIRI VIS	2 channels, AVHRR #1 and #2
Provided products	DHR_30, BHR_ISO for MVIRI VIS	0.3-30 µm black sky and white sky albedo
Spatial resolution	Ca. 3 km at SSP, more for larger observation zenith	0.05° globally
Nominal temporal resolution	10 days	8 days
Temporal representation	Most likely value in 10-day period	Complex filtering over 33-day interval
Reference conditions	30° solar zenith angle	Local solar noon
Anisotropy consideration	RPV model of BHR	Observation-based LUT approach
Atmospheric correction	Inherently included in retrieval	Explicit atmospheric correction

The main differences between MSA and GLASS-AVHRR are summarised in Table 12. The following approach was chosen to allow for a meaningful comparison of the two albedo products:

> *Reference observation conditions:*
> Illumination geometries were determined for the chosen reference sites to be able to identify those GLASS values characterized by local noon solar zenith angles around 30°, For this study, the specific interval [20°, 40°] was chosen.

---

[22] MODIS-based GLASS products are given at 1km spatial resolution.

> *Spectral characteristics:* The spectral-to-broadband conversion factors published in Tables 5 and 6 of *EUMETSAT [2014-A]* have been used to convert the MSA products DHR_30 and BHR_ISO to the corresponding broadband values, further on referred to as DHR_30_BB and BHR_ISO_BB.

> *Spatial resolution:*
> In order to compensate for potential navigation errors and to arrive at surface areas of comparable size, product median values of 5×5 grid cells for MSA resp. 3×3 grid cells for GLASS were derived with the actual site contained in the centre cell. This leads to observed surface areas on the order of 20×20 km² for both MSA and GLASS.

> *Temporal representation:*
> The GLASS products are the result of complex temporal filtering and data merging processes to fill gaps, remove cloud affected observations, etc. This filtering strongly smoothes the GLASS albedo time series as compared to MSA. Implementing such filtering techniques for MSA to enhance product comparability is beyond the scope of this project. We herein therefore rely on robust statistical measures when comparing GLASS and MSA products.

> *Quality information:*
> The following quality measures were used to identify values accepted for subsequent analysis:

> > o   MSA: `QUALITYFLAG = 0` (quality is "OK", see *EUMETSAT [2014-A, Annex A2]*).

> > o   GLASS: `quality bit 1 = 0` (quality at least "acceptable") AND
> > `quality bit 15 = 0` (result is "valid").

6.6   Comparison tools

Comparison of MSA with the corresponding GLASS products is done through visual interpretation of specifically tailored graphical data representations as well as automated statistical analyses:

6.6.1   Histograms

Histograms allow for the identification of the most frequently occurring albedo value at a specific location. This information is subsequently used to calculate site-specific representative albedo values.

> Individual histograms have been produced for MSA DHR_30_BB and BHR_ISO_BB as well as for the corresponding GLASS products BSA and WSA at selected sites.

> The considered time range is [01/1981, 12/2000] for 0DEG as well as [01/1997, 12/2000] for IODC observations.

> A value of 0.01 has been chosen as histogram bin size to allow for the resolution of e.g. multimodal surface albedo patterns.

6.6.2   Scatter plots

A scatter plot visualises the degree of correlation between two variables. It may thus contribute to the identification of processes that cause systematic differences between the MSA and GLASS datasets.

> ➢ Scatter plots have been established opposing MSA DHR_30_BB to GLASS BSA as well as MSA BHR_ISO_BB to GLASS WSA, respectively.

> ➢ Only pairs of values (MSA/GLASS) where both MSA and GLASS provide valid values with a maximum delay of 7 days are accepted.

6.6.3 Time series

Time series allow identifying temporal dependencies of observed characteristics, e.g. seasonal effects or long-term trends, but also the ability to resolve short-term processes.

> ➢ Time series of MSA DHR_30_BB vs. GLASS BSA and MSA BHR_ISO_BB vs. GLASS WSA have been established for the considered reference sites.

> ➢ Time series are shown in two versions: one including all values, including NODATA values to indicate the gaps in the individual time series, another one zooming into the most relevant albedo range.

6.6.4 MSA retrieval parameters

Retrieval parameters from the MSA processing comprise the RPV parameters AOD, Θ, ρ_0, and k. It is assumed that numerically induced fluctuations of the retrieval parameters may be a contributing factor to MSA fluctuations. A suitable graphical representation of the MSA retrieval parameters may thus contribute to a better understanding of the MSA retrieval performance.

> ➢ The MSA retrieval parameters AOD, Θ, ρ_0, and k are shown for the reference year 2000.

> ➢ Additionally shown are values for MSA DHR_30_BB as well as GLASS BSA.

6.6.5 Statistical key parameters

Robust statistical parameters allow for a meaningful quantification of systematic differences between MSA and GLASS albedo values. The following parameters have been derived from the albedo values accepted for the creation of scatter plots (see above):

> ➢ Mode (i.e. the maximum of the probability density distribution),

> ➢ Median as well as 5%-, 25%-, 75%-, and 95%-quantiles.

6.6.6 Visual inspection

Visual inspection of the created figures might help to further identify problems with either approach (GSA or GLASS). For example, extreme values in individual time series or opposing trends may hint to fundamental problems in the associated retrieval processes.

6.7 Comparison results

In the following subsections, we show selected results illustrating the comparison approach and pointing to specific issues of the MSA and GLASS albedo products. A compilation of all generated figures is given in the appendix for all considered sites.

The following conventions have been consistently applied when creating the figures:

➢ MSA products are shown in blue, GLASS products are shown in red.

➢ Black sky albedo products (DHR_30 for MSA, BSA for GLASS) are represented by downward pointing triangles.

➢ GLASS BSA products taken at local noon solar zenith angles outside the interval [20°, 40°] are shown in orange.

➢ White sky albedo products (BHR_ISO for MSA, WSA for GLASS) are represented by circles.

➢ Symbols or lines representing median values are shown in gold.

6.7.1 Histograms

Histograms such as shown in Figure 49 for site BOUMBA_BEK (rainforest) and LIBYA (desert) allow deducing fundamental differences between MSA and GLASS products:

➢ Both sites are characterized by surfaces that do not show large albedo variations. This is reflected by the narrow histograms of the GLASS albedo products.

➢ The MSA and GLASS histogram maxima (the modes) agree well, indicating that both methods often derive similar albedo values and that the mode is a good proxy for assigning characteristic surface albedo values.

➢ MSA products are frequently cloud contaminated. A prominent example is site BOUMBA_BEK where MSA values above ca. 0.2 are most likely cloud contaminated.

➢ MSA products are characterised by a broader distribution as compared to the corresponding GLASS products:

    o The temporal filtering applied is obviously one reason for the narrower distribution of the GLASS albedo values.

    o Cloud contamination contributes to the widening of MSA products at site BOUMBA_BEK.

    o Noise introduced through the treatment of anisotropy in GSA could is likely an additional factor contributing to the observed broader MSA distribution.

    o The covered albedo range at site LIBYA is significantly wider for BHR_ISO_BB than it is for DHR_30_BB. This seems implausible and may be a consequence of the way to derive BHR_ISO in MSA.
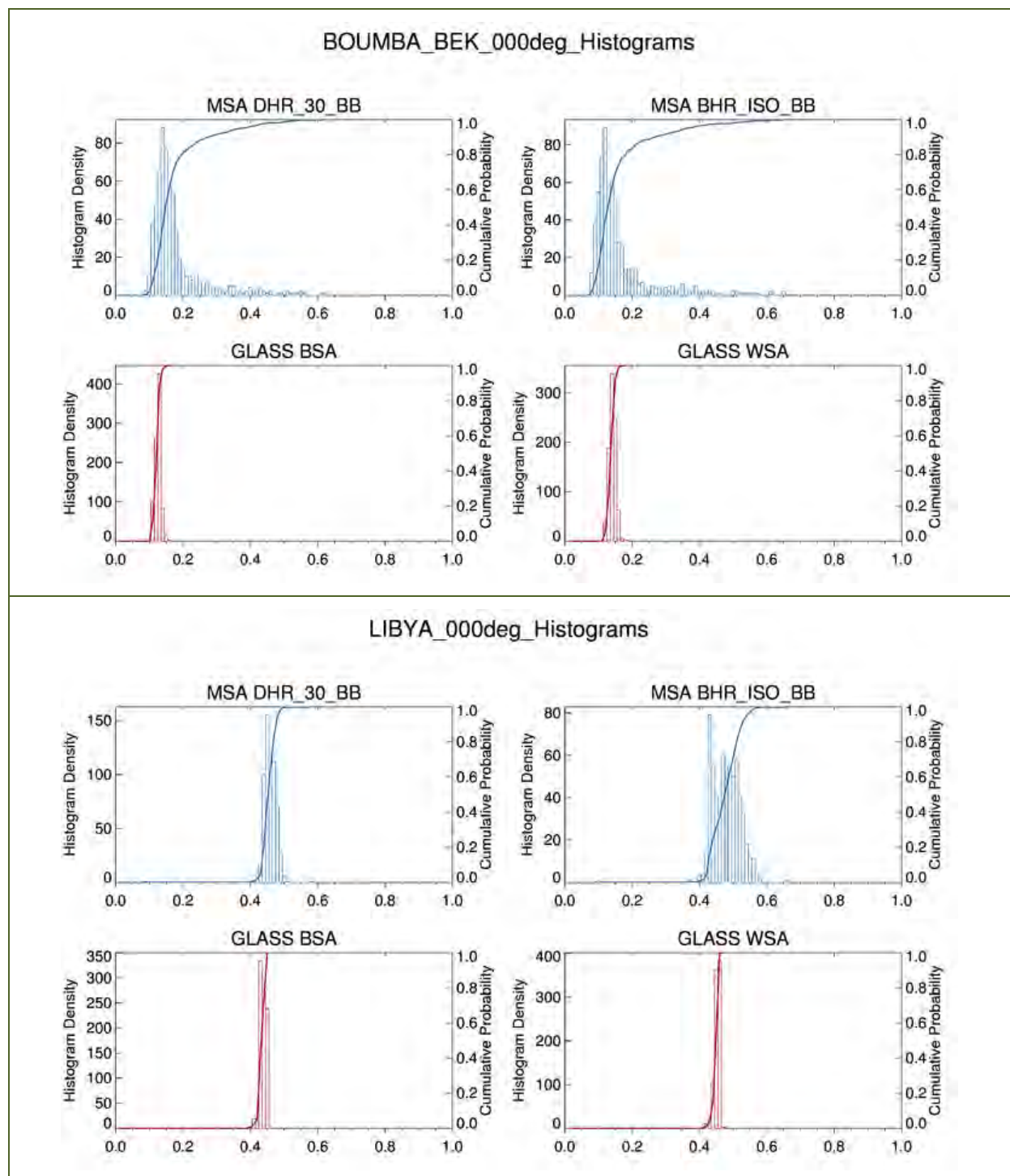
Figure 49: Histograms of MSA and GLASS albedo products for the period 1981 to 2000 (0DEG) for sites BOUMBA_BEK **(top), representing broadleaved evergreen forest, and** LIBYA **(bottom), representing bright desert surfaces.**
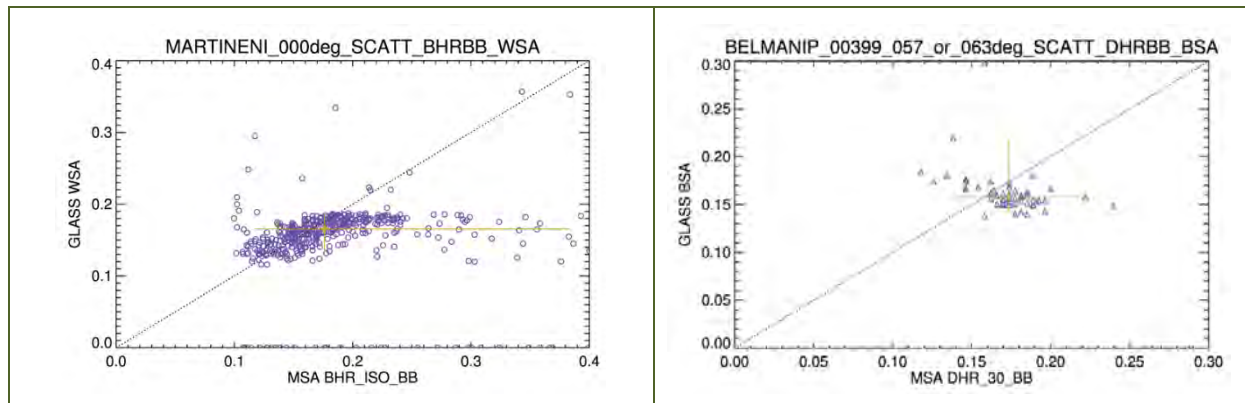
6.7.2 Scatter plots

Figure 50: Scatterplot of MSA BHR_ISO vs. GLASS WSA for site `MARTINENI` (left) characterized by agrarian use (0DEG, 1981 to 2000), as well as MSA DHR_30 vs. GLASS BSA for site `BELMANIP_00399` (right), representing grasslands in Southern Kazakhstan (IODC, 1998 to 2001). The golden cross indicates the median values, and the bars represent the range between the 5% and the 95% quantiles. The 1:1 diagonal is additionally shown as a visual interpretation aid.

The following observations can be made from the scatterplots shown in Figure 50 for sites `MARTINENI` (agriculturally used) and `BELMANIP_00399` (temperate grasslands):

➢ Again, MSA values generally cover over larger albedo ranges than do the corresponding GLASS values.

➢ Cloud contamination is an issue for MSA also above agriculturally used surfaces: values above ca. 0.2 with significantly lower corresponding GLASS values at site `MARTINENI` are most likely cloud-contaminated.

➢ Except for obviously cloud-contaminated MSA values, the albedo is similarly represented by both MSA and GLASS products at site `MARTINENI`, with very similar median values between 0.16 and 0.17 for both MSA BHR_ISO_BB and GLASS WSA.

➢ A slightly larger deviation is observed for site `BELMANIP_00399`, but GLASS BSA and MSA DHR_30_BB median values are still with ±0.02. The smaller MSA albedo values not represented by GLASS may be linked to short-term events (e.g. flooding).
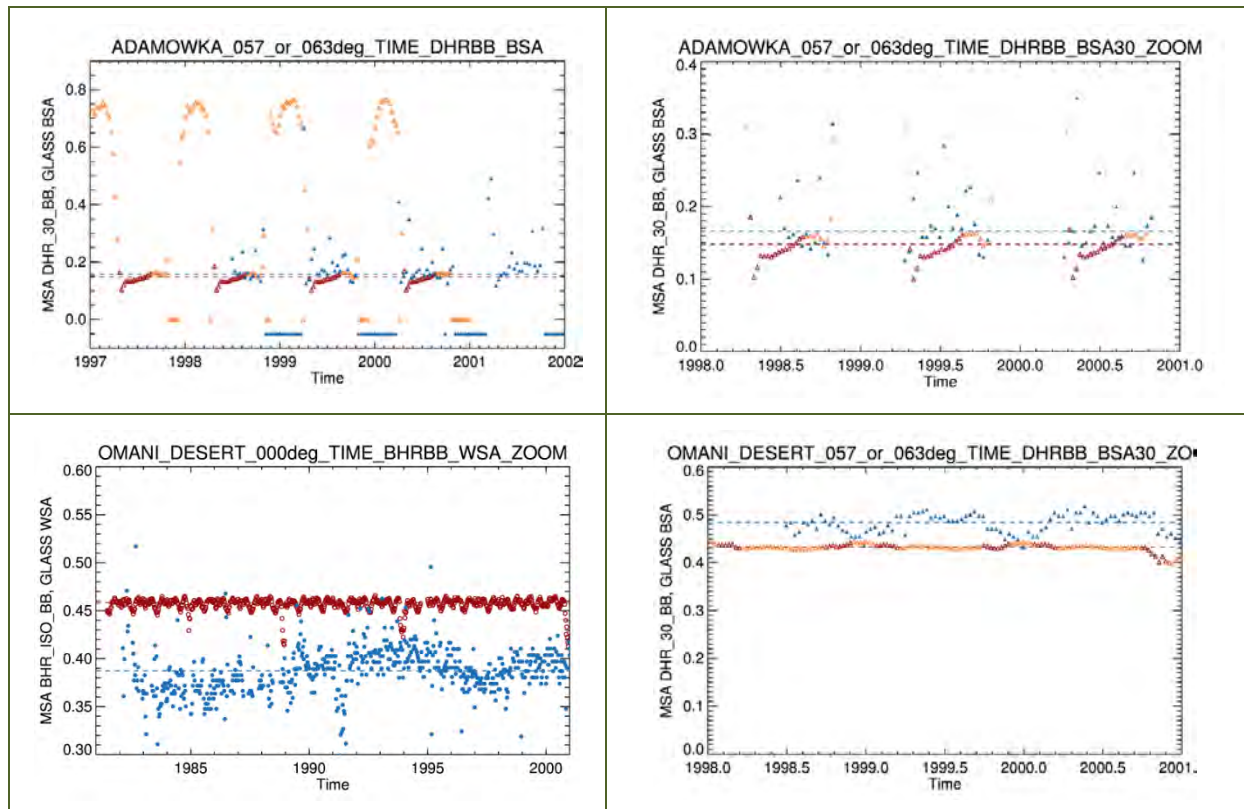
6.7.3 Time series

Figure 51. Top: MSA DHR_30 *vs*. GLASS BSA for site ADAMOWKA (top), characterized by agrarian use, for the period 1997 to 2002 (IODC) as well as MSA BHR_ISO *vs*. GLASS WSA for site OMANI_DESERT, representing bright desert soils in Oman (bottom) for the period 1981 to 2001 (0DEG). GLASS BSA values for solar zenith angles outside the range [20°, 40°] are shown in orange.

Visually inspecting time series of MSA and GLASS albedo products allows deducing further quality aspects of both products. The following conclusions can be made deduced from time series at sites ADAMOWKA and OMANI_DESERT (see Figure 51).

➢ As illustrated for site ADAMOWKA, noise may hide seasonal signals in the MSA products. While a (plausible) regular seasonal cycle is observed in the GLASS products for site ADAMOWKA with values continuously increasing from spring to late summer, a similar cycle can hardly be observed in the corresponding MSA data.

➢ The GLASS statistical temporal filtering introduces significant smoothing. This effect can clearly be observed at site ADAMOWKA, where a regular albedo increase typically lasting between six and eight GLASS time steps (representing 48 to 64 days) is observed in early winter, followed by a short time span of maximum albedo values and a subsequent regular decrease. Such temporal evolution is implausible. There should be a sharp albedo increase in early winter after the first significant snowfall, followed by a long plateau of high albedo values at this site characterized by an average snow cover on the order of 150 days per winter.

➢ Another noticeable feature in the GLASS time series can be observed at the end of the winter at site ADAMOWKA when the albedo values "overshoot" to very low values. Potential natural

causes may include temporary flooding as a result of snow melt, but the feature might also be a result of numerical artefacts.

➢ Of all investigated sites, `OMANI_DESERT` shows the largest differences between the MSA and GLASS albedo values (*e.g.* GLASS WSA on average about 0.07 above MSA DHR_30).

➢ While GLASS products generally show an excellent long-term temporal stability for site `OMANI_DESERT`, the corresponding MSA products show significant long-term fluctuations. Interestingly, the effect appears to be systematically larger for MSA BHR_ISO than for MSA DHR_30. These fluctuations appear not to be caused by MVIRI intercalibration issues, since there are no apparent discontinuities visible in the MSA time series.

➢ In addition to the long-term fluctuations, MSA values also exhibit very strong short-term fluctuations at site `OMANI_DESERT` on the order of 0.05 and more between consecutive values. Considering the very stable nature of the desert surfaces and the low likelihood for cloud contamination, these short-term fluctuations are likely an artefact caused by errors in the anisotropy retrieval parameters.

➢ Boundary effects are frequently observed at the end of GLASS time series (see e.g. the drop in WSA at the end of the year 2000 at site `OMANI_DESERT`.

➢ Opposing seasonal cycles are observed for MSA IODC DHR_30_BB and GLASS BSA for site `OMANI_DESERT`: a slight increase in BSA corresponds to a more pronounced decrease in DHR_30_BB. However, phases are identical again at the end of the GLASS time series, which may indicate fundamental issues with the GLASS temporal averaging scheme.

➢ There are a number of drops in the GLASS time series which are not represented in MSA and vice versa:

    o See for example site `OMANI_DESERT` where GLASS WSA drops significantly in the winters 84/85, 88/89 and 93/94 while similar drops are not observed in MSA BHR_ISO.

    o On the other hand, there is an apparent drop in BHR_ISO in summer 1991 not represented in the WSA time series.

    o More detailed analyses are required to elucidate whether these drops are caused at least partly by real processes (e.g. precipitation events).

6.7.4 MSA retrieval parameters

Graphical representations of the MSA retrieval parameters $k, \Theta, \rho_0,$ and AOD have been produced for each reference site for the reference year 1999.
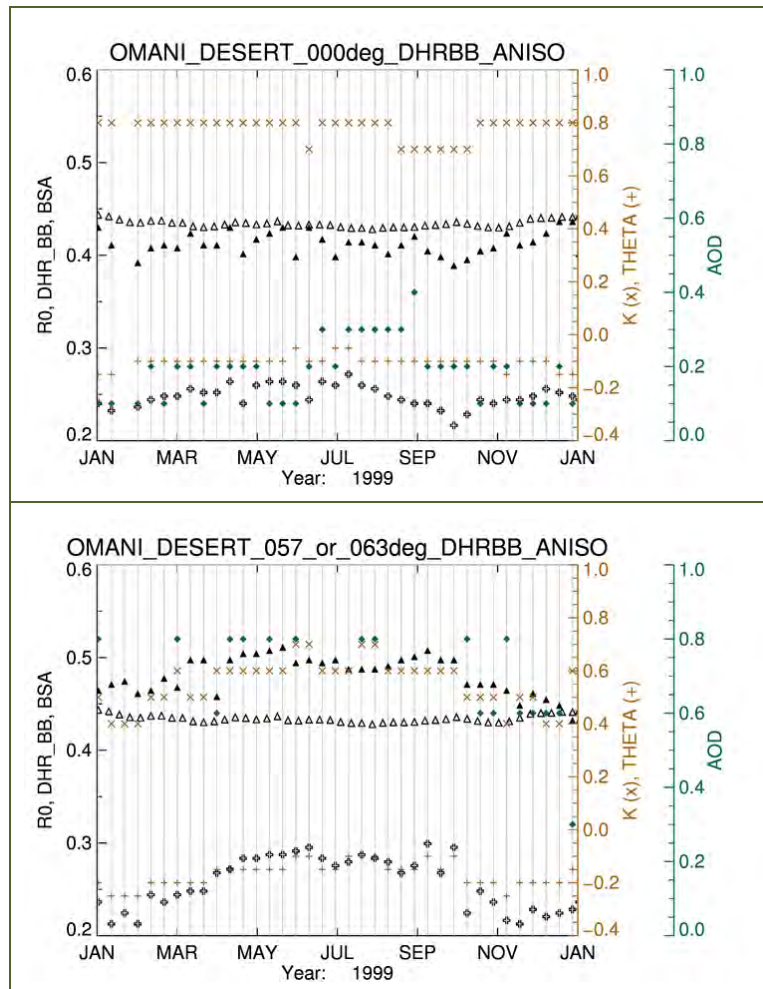

Figure 52: MSA retrieval parameters ρ_0 (black double cross), k (×), Θ (+), as well as AOD (filled diamond) for site `OMANI_DESERT` for observation geometries 0DEG (top) and IODC (bottom) in the year 1999. Additionally shown are MSA DHR_30_BB (solid triangle) as well as GLASS BSA (open triangle).

The following conclusions can be drawn from the example of site `OMANI_DESERT` shown in Figure 52:

➢ The observation geometry has a significant influence on the BRF retrieval parameters:

     o k adopts mostly constant values of 0.8 for 0DEG, while it shows a seasonal cycle with values between ca. 0.4 and 0.7 for IODC.

     o Θ adopts mostly constant values -0.1 for 0DEG, while it shows a seasonal cycle with values between ca -0.25 and -0.1 for IODC.

     o ρ_0 is rather constant with values around 0.25 for 0DEG, while it shows a seasonal cycle with values between ca. 0.2 and 0.3 for IODC.

➢ The retrieved AOD differs fundamentally between 0DEG, where it is retrieved with values between ca. 0.1 and 0.3, and IODC, where it ranges between ca. 0.6 and 0.8.

➢ The differences in the retrieved BRF parameters lead to significantly differing DHR_30_BB values for the two observation geometries: While DHR_30_BB is on average about 0.04 *below* the corresponding GLASS product for 0DEG, it is about 0.06 *above* for IODC with the largest deviation in summer.

➢ There are a number of spikes and drops between consecutive dates, which may provide further insight into MSA retrieval performance. An interesting such case is observed in the last three dates in April and the first date in May for the 0DEG observation geometry: While k, Θ, and AOD are all unchanged over the four consecutive dates, ρ_0 varies significantly from date to date within a 0.05 wide albedo range. As such rapid fluctuations of the surface albedo are rather unlikely (precipitation events to be excluded), they may point to MSA retrieval deficiencies.
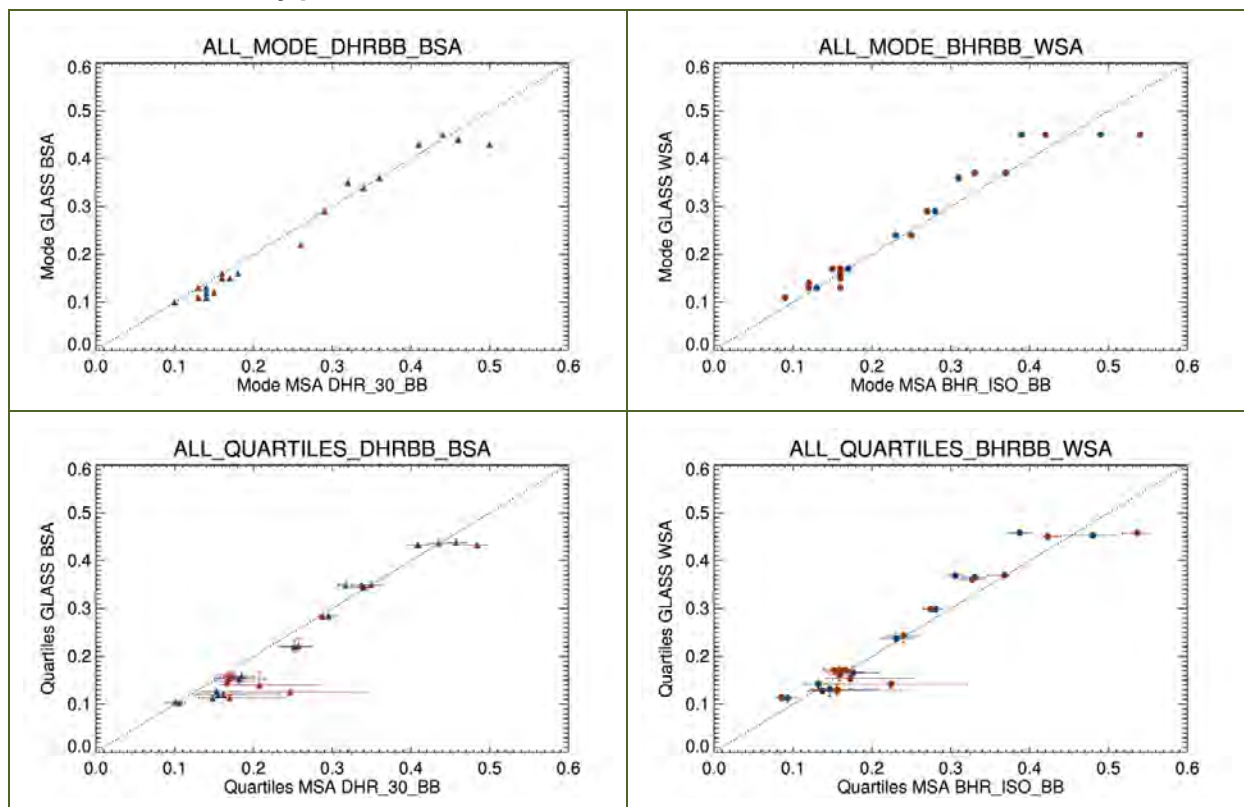
6.7.5 Statistical key parameters

Figure 53: Top left: MSA DHR_30_BB vs. GLASS BSA mode for all sites listed in section 6.4 (0DEG: blue, IODC: red). Top right: Same as top left, but for MSA BHR_ISO_BB vs. GLASS WSA. Bottom left: MSA DHR_30_BB vs. GLASS BSA median. Additionally shown are the 25%-75% quantile ranges. Bottom right: Same as bottom left, but for MSA BHR_ISO_BB vs. GLASS WSA.

For selected sites covering a wide range of surface albedo values, a number of robust statistical key parameters have been derived to allow for a quantitative comparison of MSA vs. GLASS albedo values. These parameters have been derived for those cases where both MSA and GLASS provided valid retrievals within a maximum time difference of seven days. This means that e.g. most snow cover cases

have not been included since MSA does normally not provide data over snow covered surfaces. The following parameters were calculated:

➢ Albedo mode, i.e. most frequently observed albedo value, derived from the histograms presented in section 6.6.1 by applying a three-element boxcar window twice to ensure the existence of a unique maximum. The mode is only marginally influenced by random fluctuations, outliers or occasional cloud contamination and constitutes such a robust method to identify systematic deviations between the two methods.

➢ Median albedo value, representing a robust measure of the "average" albedo at a site. Even though it is more robust than the arithmetic mean, it will still be influenced by e.g. cloud contamination.

➢ 25% and 75% as well as 5% and 95% quantiles, representing the range around the median containing half resp. 90% of all observed albedo values. The quantiles provide information on the distribution of the retrieved albedo values and may help to identify and quantify fundamental differences between the retrieval schemes.

The following conclusions can be drawn from the results shown in Figure 53:

➢ In general, there is a good agreement between the modes of corresponding MSA and GLASS surface albedo values, meaning both methods often agree on the most likely albedo values.

➢ For dark surfaces, the MSA DHR_30_BB values are slightly above the corresponding GLASS BSA values. This could mean that undetected clouds influence even the MSA modes.

➢ Interestingly, this relative overestimation of MSA values is not observed when looking at the white sky albedo modes.

6.8 Conclusions

The comparison of MSA with GLASS data leads to a number of conclusions:

➢ It is confirmed, that Insufficient cloud removal constitutes the biggest MSA quality issue:

    o It may lead to erroneous estimates of average albedo values and trends.

    o It may overshadow relevant effects at the surface (e.g. seasonal course).

    o It renders comparison with other products difficult.

➢ In addition to unidentified clouds, the "unstable" retrieval of anisotropy parameters adds significantly to MSA product scatter.

➢ GLASS products undergo statistical temporal filtering techniques (33-days composition period for the AVHRR product) causing a number of quality issues:

    o Noise is reduced, but rapid natural temporal changes (e.g. onset of snow cover) are filtered out or temporally distributed in an unrealistic way.

    o In some cases, statistical temporal filtering appears to lead to temporal shifts in seasonal effects.

> Related to the above, seasonal cycles, if not hidden by noise, are more pronounced in MSA than they are in GLASS.

> Anisotropy effects are likely the main cause for the observed differences of the MSA DHR_30 values between the 0DEG and IODC coverages.

> While the MSA temporal stability appears good for dark surfaces, it is partly problematic for bright surfaces, especially for the early Meteosats. This may point to a problem in the MVIRI instrument calibration or the spectral-to-broadband coefficients applied.

> Related to the above, MSA DHR_30 compares rather well with GLASS BSA for periods obviously not influenced by clouds above dark to moderately bright surfaces.

> A number of implausible MSA values have been observed. These could be used to identify further issues with the MSA retrieval scheme.

A number of recommendations can be drawn from the comparison of MSA and GLASS surface albedo products:

> The urgent need for improving the MSA cloud screening procedures has been confirmed.

> Uncertainties in the retrieval of the anisotropy parameters appear to induce additional noise in the MSA albedo values.

> The Calibration of the early MVIRIs should be reassessed, especially for the upper end of the dynamic range.

> Applying temporal filtering schemes to reduce noise in MSA products should be considered, while in the same time preserving MSA's ability to monitor short-term processes.

7. References

Baret, F., and ten co-authors (2006): Evaluation of the representativeness of networks of sites for the global validation and intercomparison of land biophysical products: proposition of the CEOS-BELMANIP. *IEEE T Geosci Remote*, 44(7), pp. 1794 – 1803, DOI: 10.1109/TGRS.2006.876030.

Baldridge, A. M., S. J. Hook, C. I. Grove, and G. Rivera (2009). The ASTER spectral library version 2.0. *Remote Sens Environ*, 113(4), pp. 711-715, DOI: doi:10.1016/j.rse.2008.11.007.

Capderou, M (2006): Satellites: Orbits and Missions. Springer Science & Business Media, ISBN 2287274693, 9782287274695, 544 pp.

Cescatti, A., and fourteen co-authors (2012): Intercomparison of MODIS albedo retrievals and in situ measurements across the global FLUXNET network, *Remote Sens Environ*, 121, pp. 323-334, DOI: 10.1016/j.rse.2012.02.019.

Diner, D. J., and fifteen co-authors (1998): Multi-angle Imaging SpectroRadiometer (MISR) - Instrument description and experiment overview, *IEEE T Geosci Remote*, 36 (4), pp. 1072-1087, DOI: 10.1109/36.700992.

ECMA (2013.): The JSON data interchange format. URL: http://www.ecma-international.org/publications/files/ECMA-ST/ECMA-404.pdf.

EUMETSAT (2014-A): Meteosat Surface Albedo Retrieval, Algorithm Theoretical Basis Document, EUM/OPS/SPE/12/3367(V2B), 68 pp.

EUMETSAT (2014-B): Meteosat Surface Albedo Retrieval, Product User's Manual, EUM/OPS/MAN/12/2872(V2H), 34 pp.

Fell, F., and eight co-authors (2012): Evaluation of the Meteosat Surface Albedo Climate Data Record (ALBEDOVAL), Final Report, 119 pp.

GCOS (2011): Systematic observation requirements for satellite-based products for climate, 2011 update. WMO GCOS Rep. 154, 127 pp.

Govaerts, Y., B. Pinty, M. Taberner, and A. Lattanzio (2006): Spectral Conversion of Surface Albedo Derived from Meteosat First Generation Observations. *IEEE Geosci Remote S*, 3(1), pp. 23-28, DOI: 10.1109/LGRS.2005.854202.

Govaerts, Y., and A. Lattanzio (2007): Retrieval Error Estimation of Surface Albedo Derived from Geostationary Large Band Satellite Observations: Application to Meteosat-2 and -7 Data. *J Geophys Res-Atmos*, 112, DOI: 10.1029/2006JD007313.

Hess, M., P. Koepke, and I. Schult (1988): Optical Properties of Aerosols and Clouds: The Software Package OPAC, *B Am Meteorol Soc*, pp. 831–844, DOI: 10.1175/1520-0477(1998)079<0831:OPOAAC>2.0.CO;2.

Hudson, S. R., S. G. Warren, R. E. Brandt, T. C. Grenfell, and D. Six (2006): Spectral bidirectional reflectance of Antarctic snow: Measurements and parameterization, *J Geophys Res-Atmos*, 111, D18106, DOI: 10.1029/2006JD007290.

Lattanzio, A., F. Fell, R. Bennartz, I. F. Trigo, and J. Schulz (2015): Quality assessment and improvement of the EUMETSAT Meteosat Surface Albedo Climate Data Record, *Atmos Meas Tech Discuss*, 8, pp. 7535-7571, DOI: 10.5194/amtd-8-7535-2015.

Lattanzio, A., Y. Govaerts, and B. Pinty (2006): Consistency of Surface Anisotropy Characterization with Meteosat observations. *Adv Space Res*, 39 (1), pp. 131-135, DOI: 10.1016/j.asr.2006.02.049.

Lattanzio, A., and eight co-authors (2013): Land Surface Albedo from Geostationary Satellites: A Multiagency Collaboration within SCOPE-CM., *B Am Meteorol Soc*, 94, pp. 205–214, DOI: 10.1175/BAMS-D-11-00230.1.

Liu, N., and six co-authors (2012): Mapping Spatially-Temporally Continuous Shortwave Albedo for Global Land Surface from MODIS Data. *Hydrol Earth Syst Sc Discuss*, 9, pp. 9043–9064. DOI: 10.5194/hessd-9-9043-2012.

Loew, A., and Y. Govaerts (2010): Towards Multidecadal Consistent Meteosat Surface Albedo Time Series. *Remote Sens*, 2(4), pp. 957–967, DOI: 10.3390/rs2040957.

Meinander, O., and fourteen co-authors (2013): Spectral albedo of seasonal snow during intensive melt period at Sodankylä, beyond the Arctic Circle. *Atmos Chem Phys*, 13, pp. 3793-3810, DOI: 10.5194/acp-13-3793-2013.

Merchant, C. J. (2013) Thermal remote sensing of sea surface temperature. *In: C. Kuenzer, C. and S. Dech (Eds.), Thermal Infrared Remote Sensing: Sensors, Methods, Applications*. Remote Sensing and Digital Image Processing, Vol. 17 2013. Springer Netherlands, Dordrecht, pp. 287-313. ISBN 978-94-007-6638-9, DOI: 10.1007/978-94-007-6639-6_15

Painter, T. H., and J. Dozier (2004): Measurements of the hemispherical-directional reflectance of snow at fine spectral and angular resolution. *J Geophys Res-Atmos*, 109, D18115, DOI: 10.1029/2003JD004458.

Pinty, B., and seven co-authors (2000-A): Surface Albedo Retrieval from Meteosat: Part 1: Theory. *J Geophys Res-Atmos*, 105, pp. 18099-18112, DOI: 10.1029/2000JD900113.

Pinty, B., and seven co-authors (2000-B): Surface Albedo Retrieval from Meteosat: Part 2: Applications. *J Geophys Res-Atmos*, 105, pp. 18113-18134, DOI: 10.1029/2000JD900114.

Pinty, B., and eight co-authors (2005): Coupling Diffuse Sky Radiation and Surface Albedo. *J Atmos Sci,* 62, pp. 2580-2591, DOI: 10.1175/JAS3479.1.

Rahman, H., M. M. Verstraete, and B. Pinty (1993): Coupled Surface-Atmosphere Reflectance (CSAR) Model .1. Model Description and Inversion on Synthetic Data. *J Geophys Res-Atmos*, 98(D11), pp. 20779-20789, DOI: 10.1029/93jd02071.

Román, M. O., and eighteen co-authors (2009): The MODIS (Collection V005) BRDF/albedo product: Assessment of spatial representativeness over forested landscapes. *Remote Sens Environ*, 113(11), pp. 2476–2498, DOI: 10.1016/j.rse.2009.07.009

Schaepman-Strub, G., M. E. Schaepman, T. H. Painter, S. Dangel, and J. V. Martonchik (2006): Reflectance quantities in optical remote sensing - definitions and case studies. *Remote Sens Environ*, 103(1), pp. 27-42. DOI: 10.1016/j.rse.2006.03.002.

Struzik, P., M. Pajek, and M. Struzik (2012): Snow Cover Monitoring From Space for Use in Hydrological Modeling. *Proceedings of the EUMETSAT Meteorological Satellite Conference 2012*, Sopot, Poland.

Wang, X., and C. S. Zender (2011): Arctic and Antarctic diurnal and seasonal variations of snow albedo from multiyear Baseline Surface Radiation Network measurements. *J Geophys Res-Earth* 116(F3), DOI: 10.1029/2010JF001864.

Winther, J. G. (1993): Landsat TM derived and in situ summer reflectance of glaciers in Svalbard. *Polar Res,* 12(1), pp. 37 - 55. DOI: 10.1111/j.1751-8369.1993.tb00421.x.

Zeng, Q., and five co-authors (1984): A study of spectral reflection characteristics for snow ice and water in the north of China. Hydrological Applications of Remote Sensing and Remote Data Transmission, *Proceedings of the Hamburg Symposium (August 1983)*, IAHS publication 145, pp. 451–462.

Zhao, X., and thirteen co-authors (2013): The Global Land Surface Satellite (GLASS) Remote Sensing Data Processing System and Products. *Remote Sens.*, 5 (5), pp. 2436-2450; DOI: 10.3390/rs5052436.

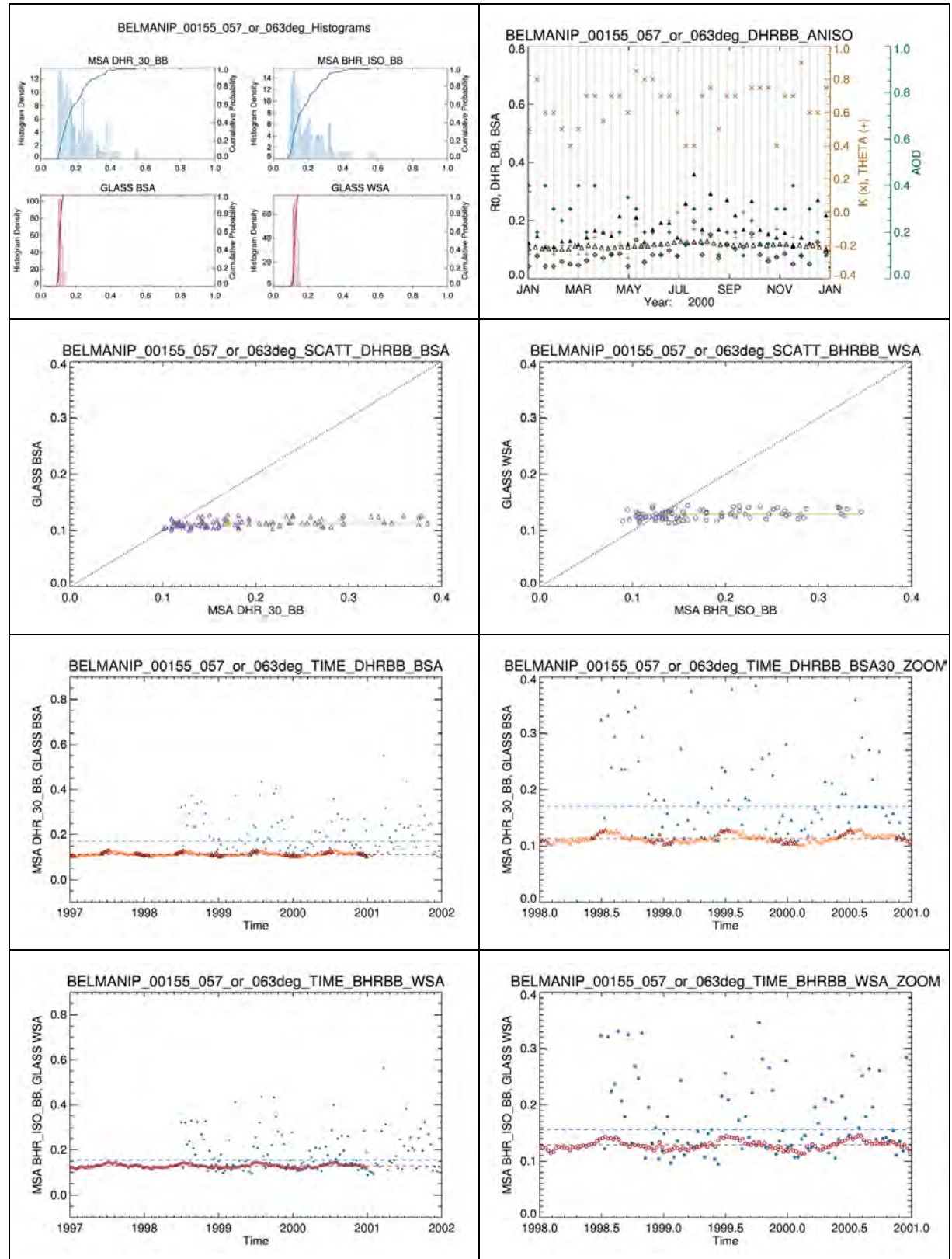# 8. Annex A: Site specific analyses (MSA vs. GLASS)
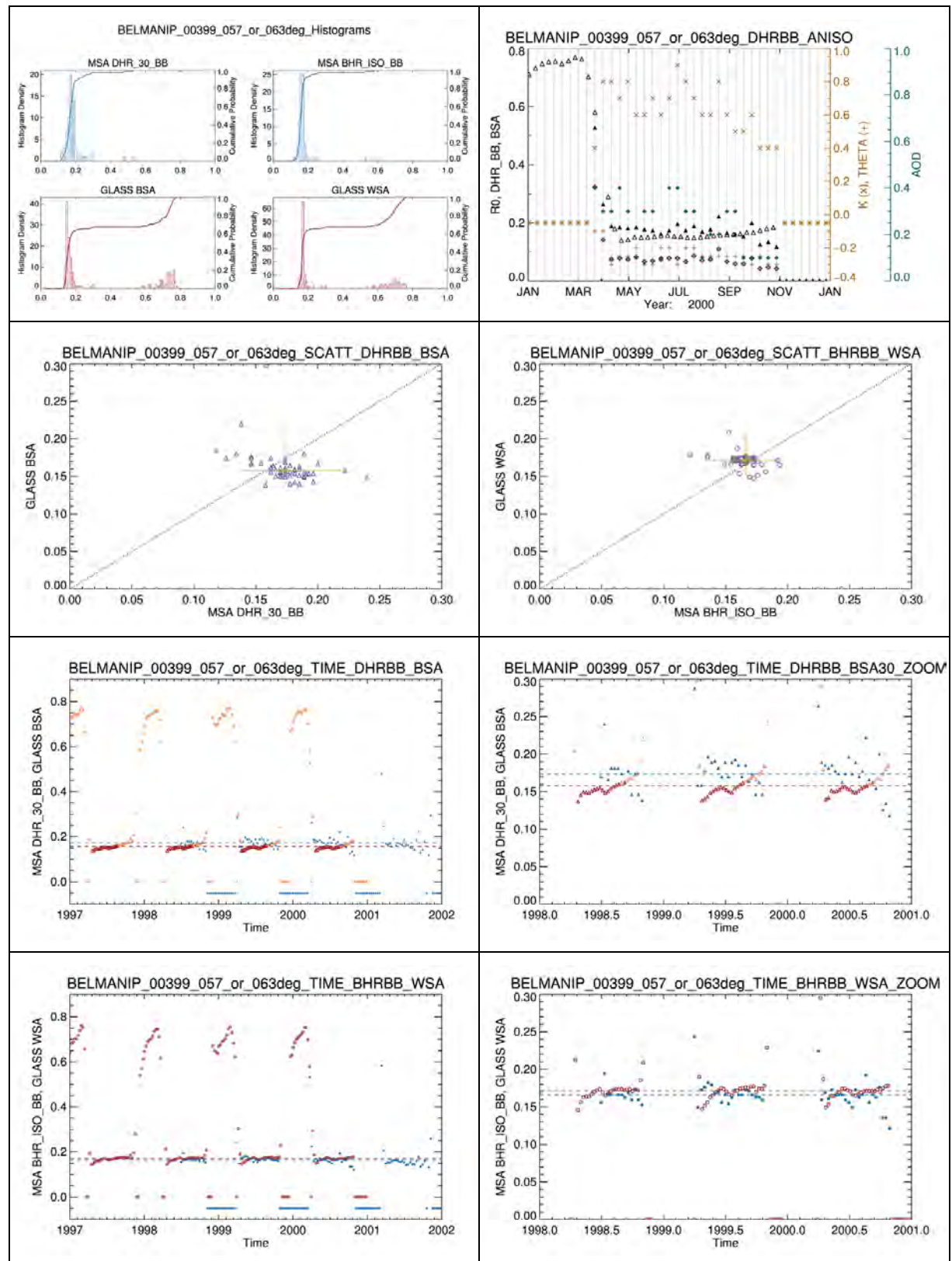
8.1 ADAMOWKA - IODC
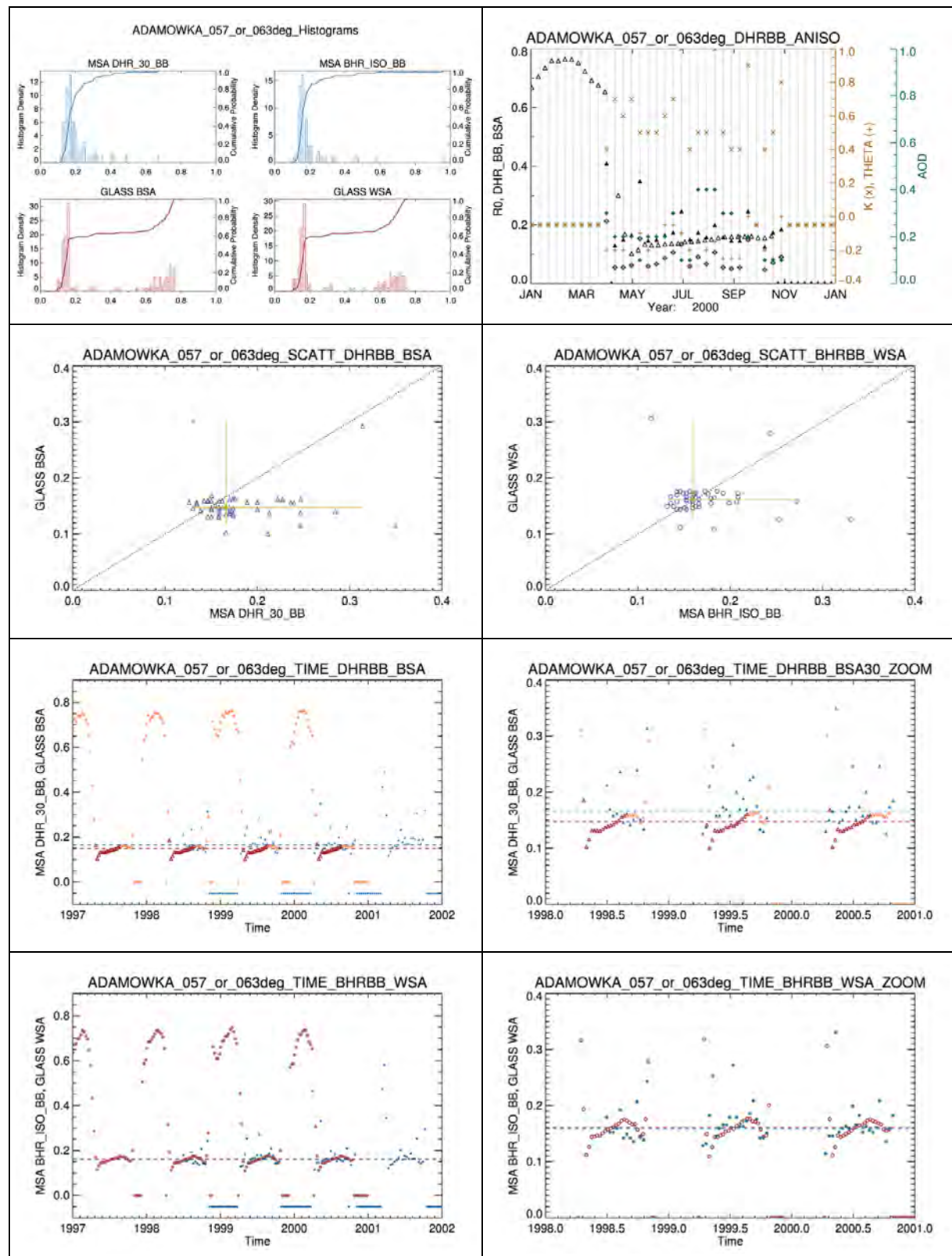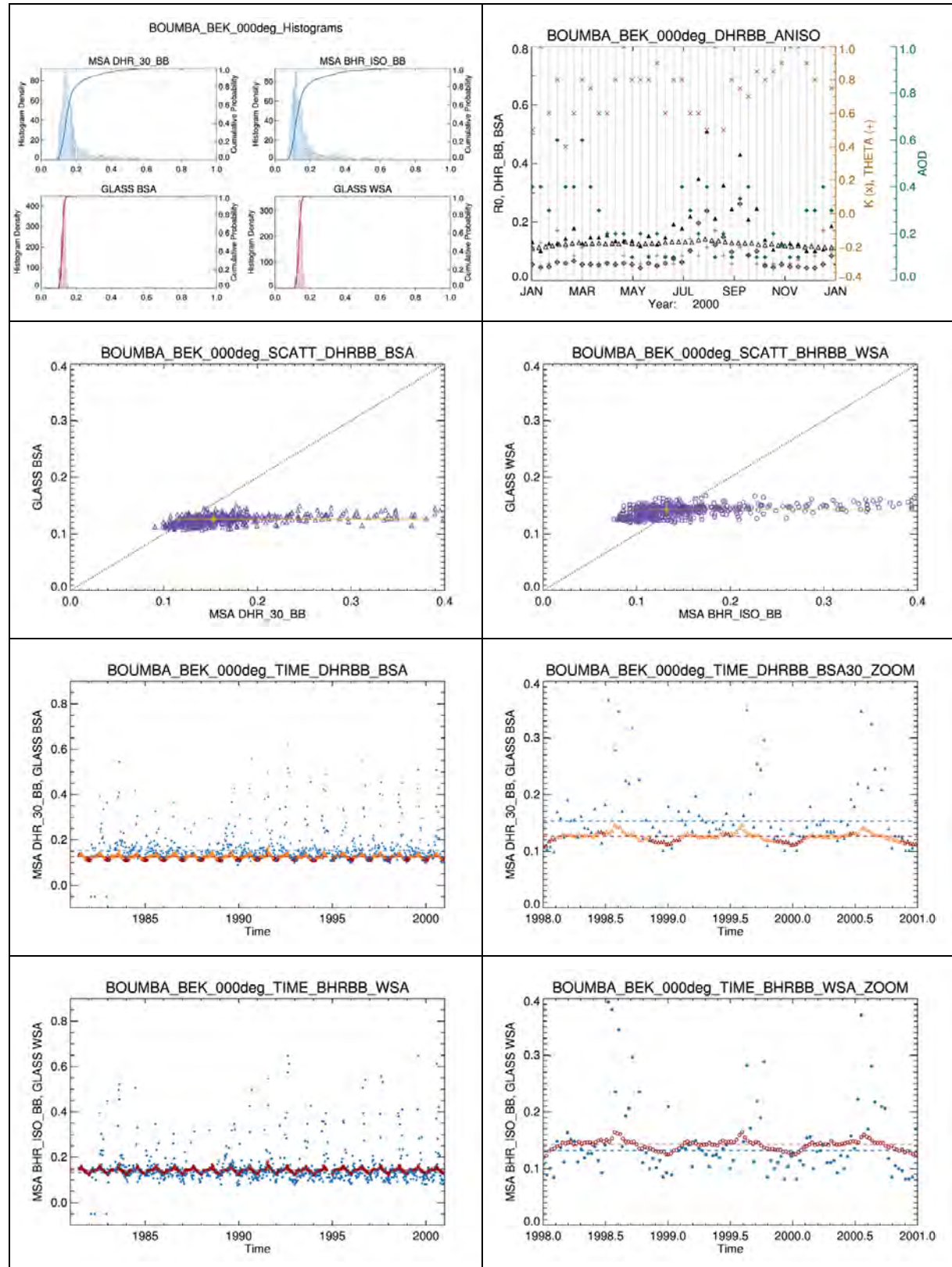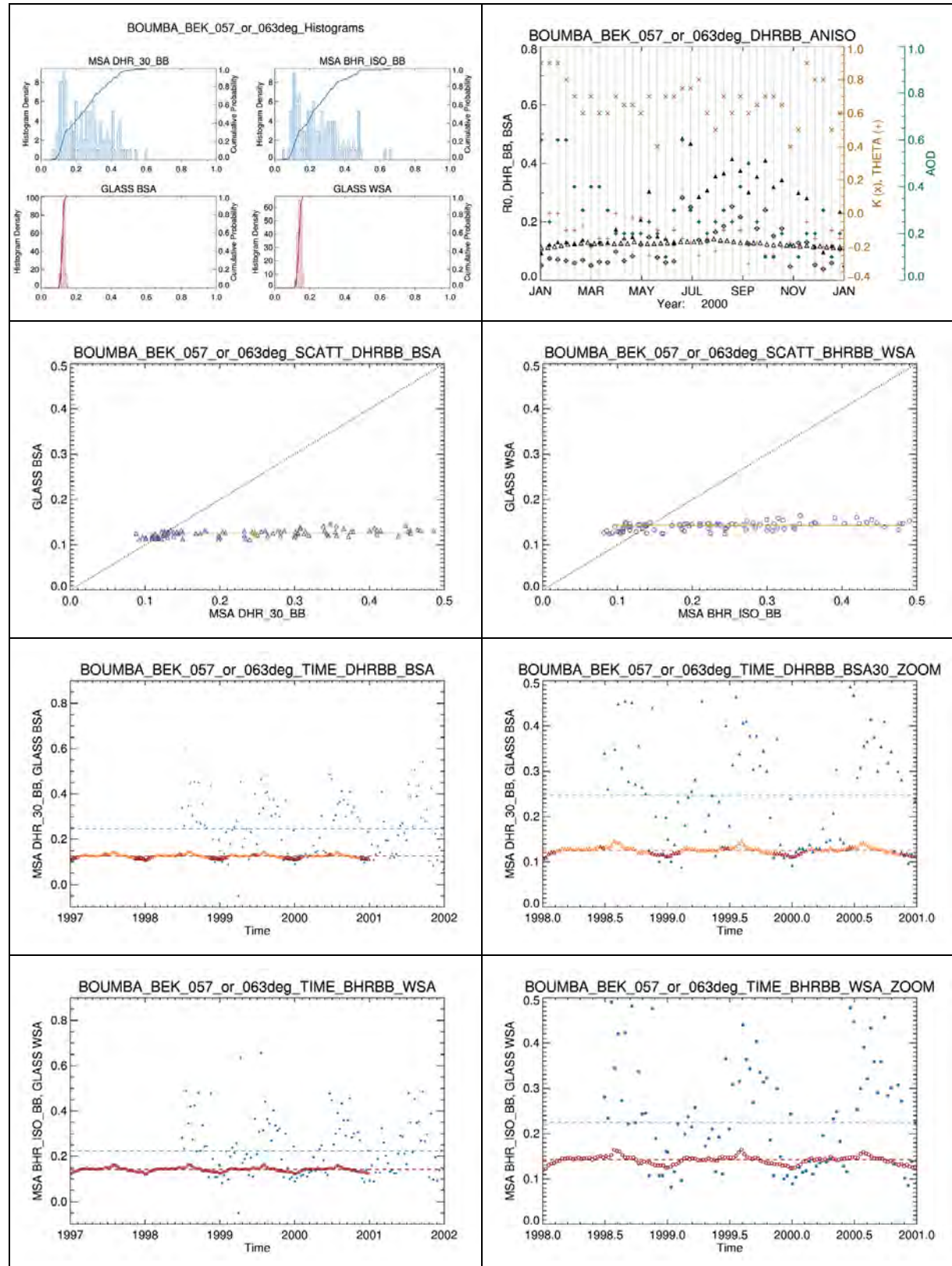
8.2 BELMANIP_00155 – 0DEG
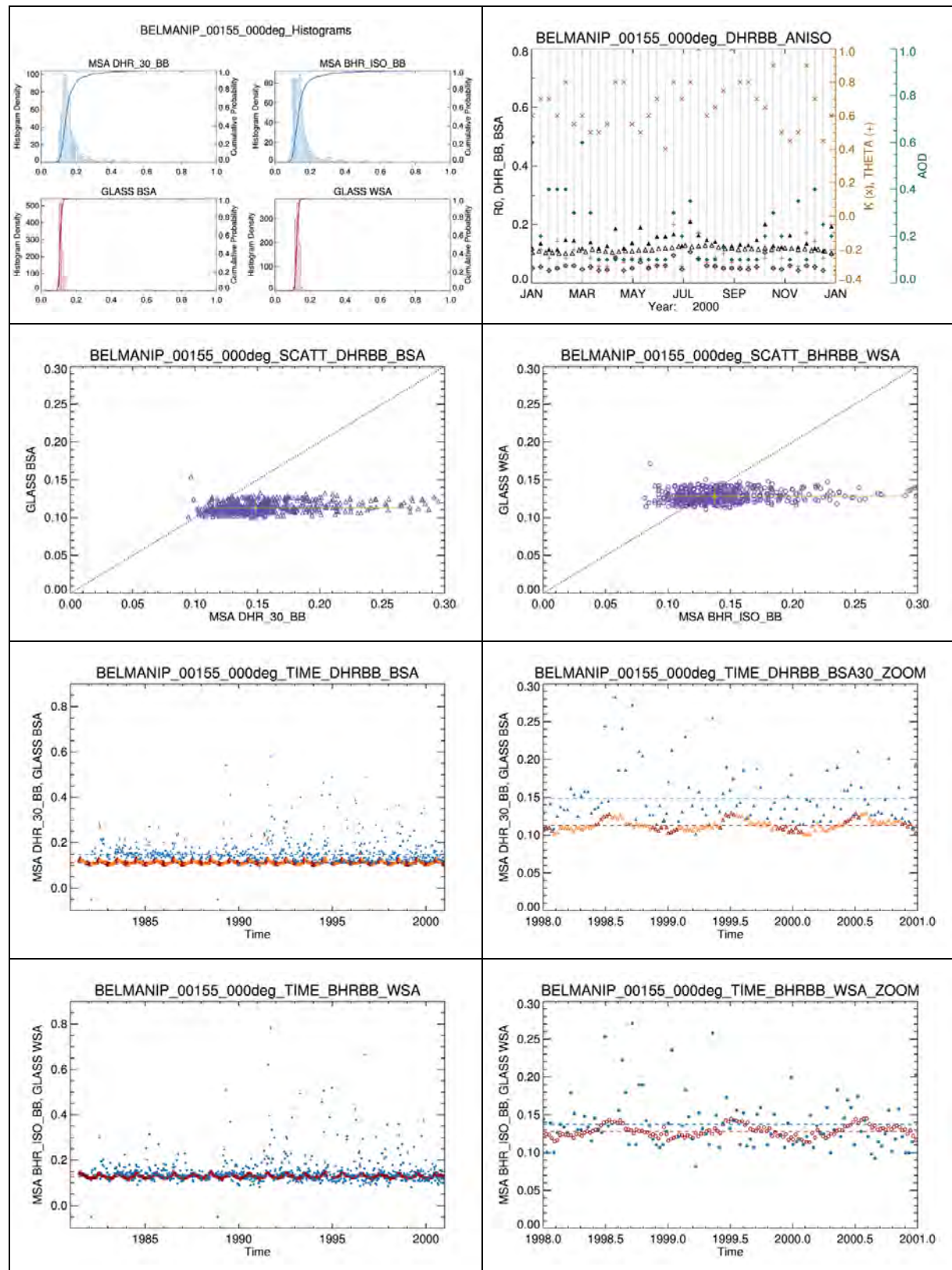
8.3 BELMANIP_00155 – IODC
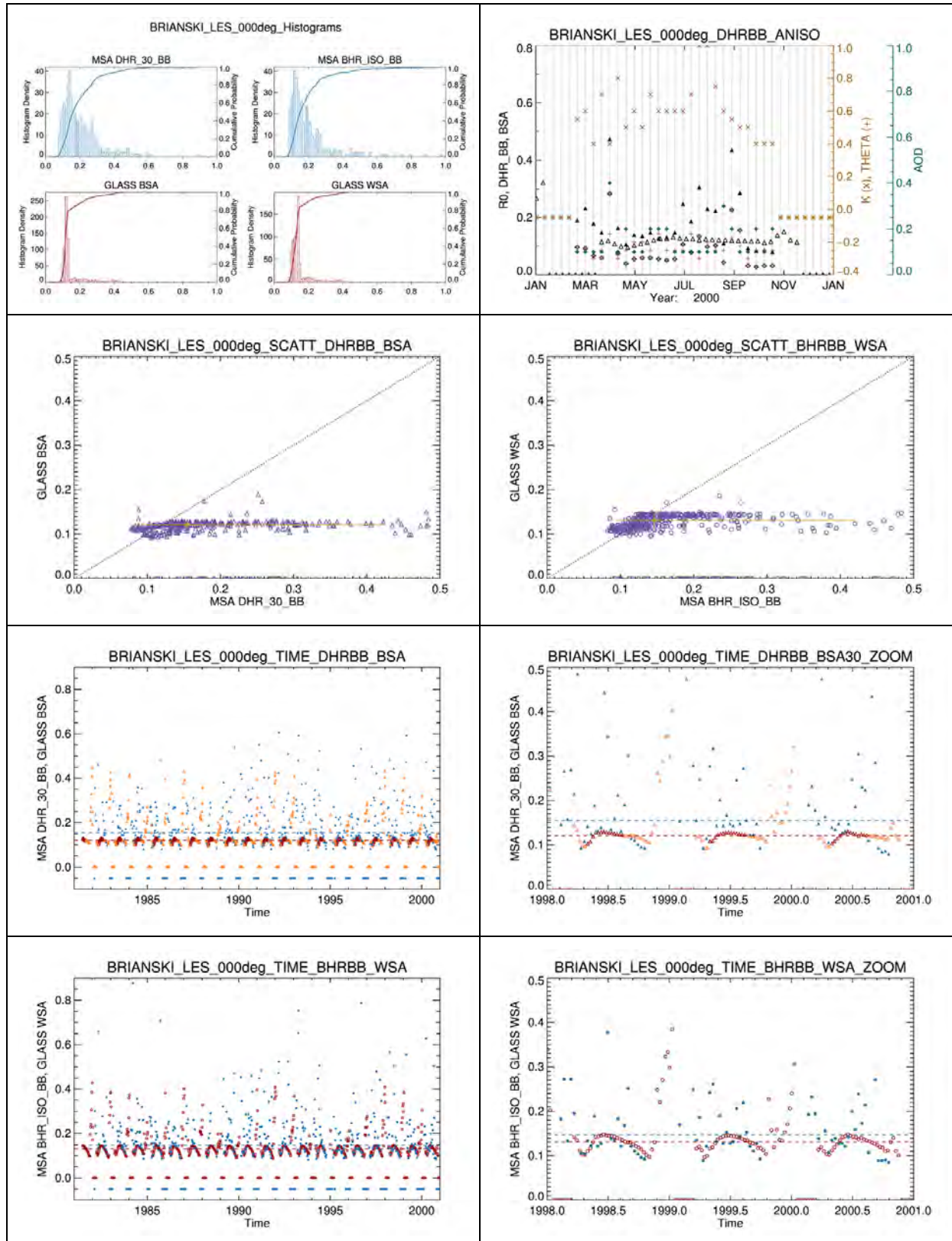
8.4 BELMANIP_00399 – IODC
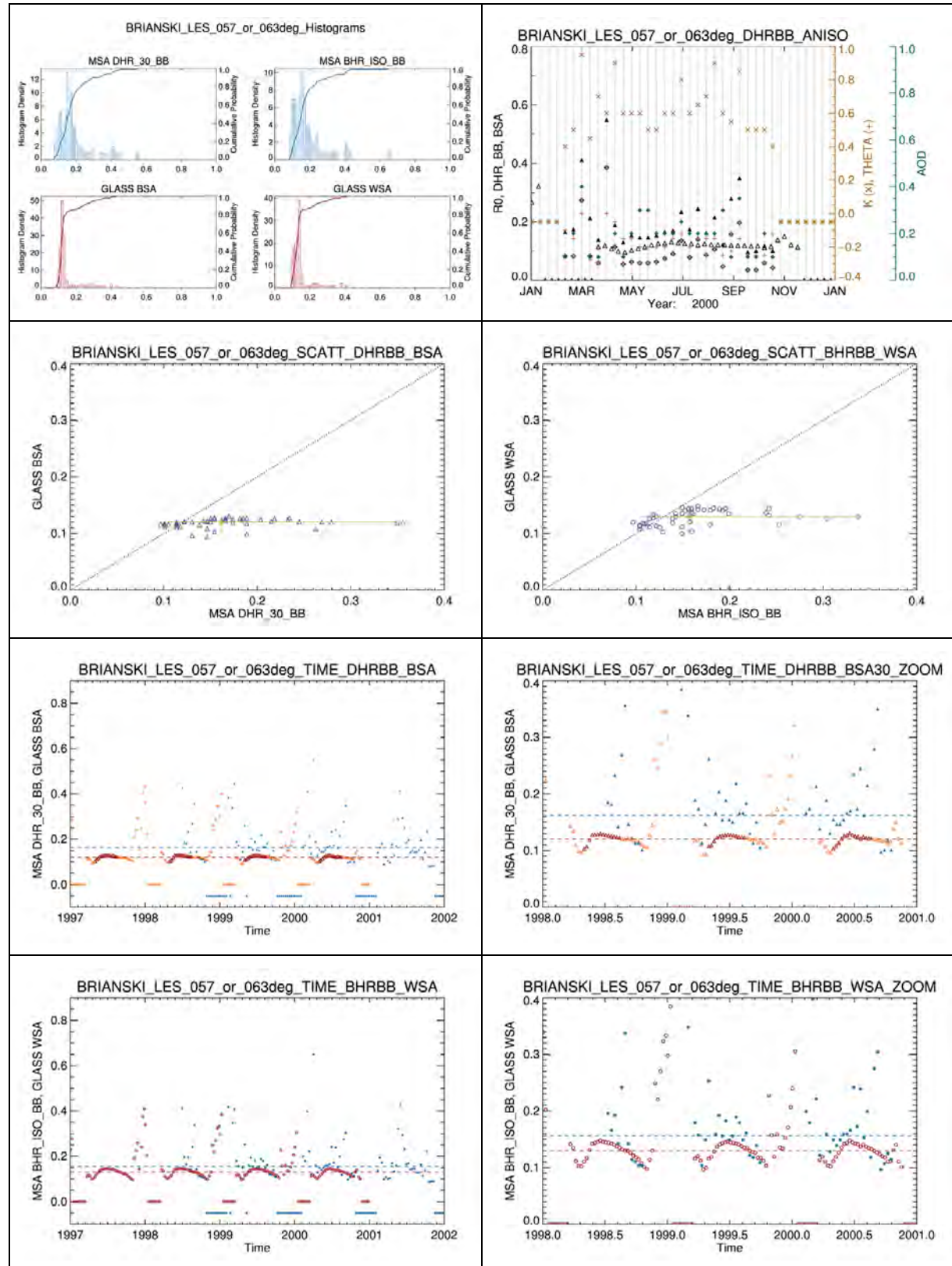
8.5 BOUMBA_BEK – 0DEG
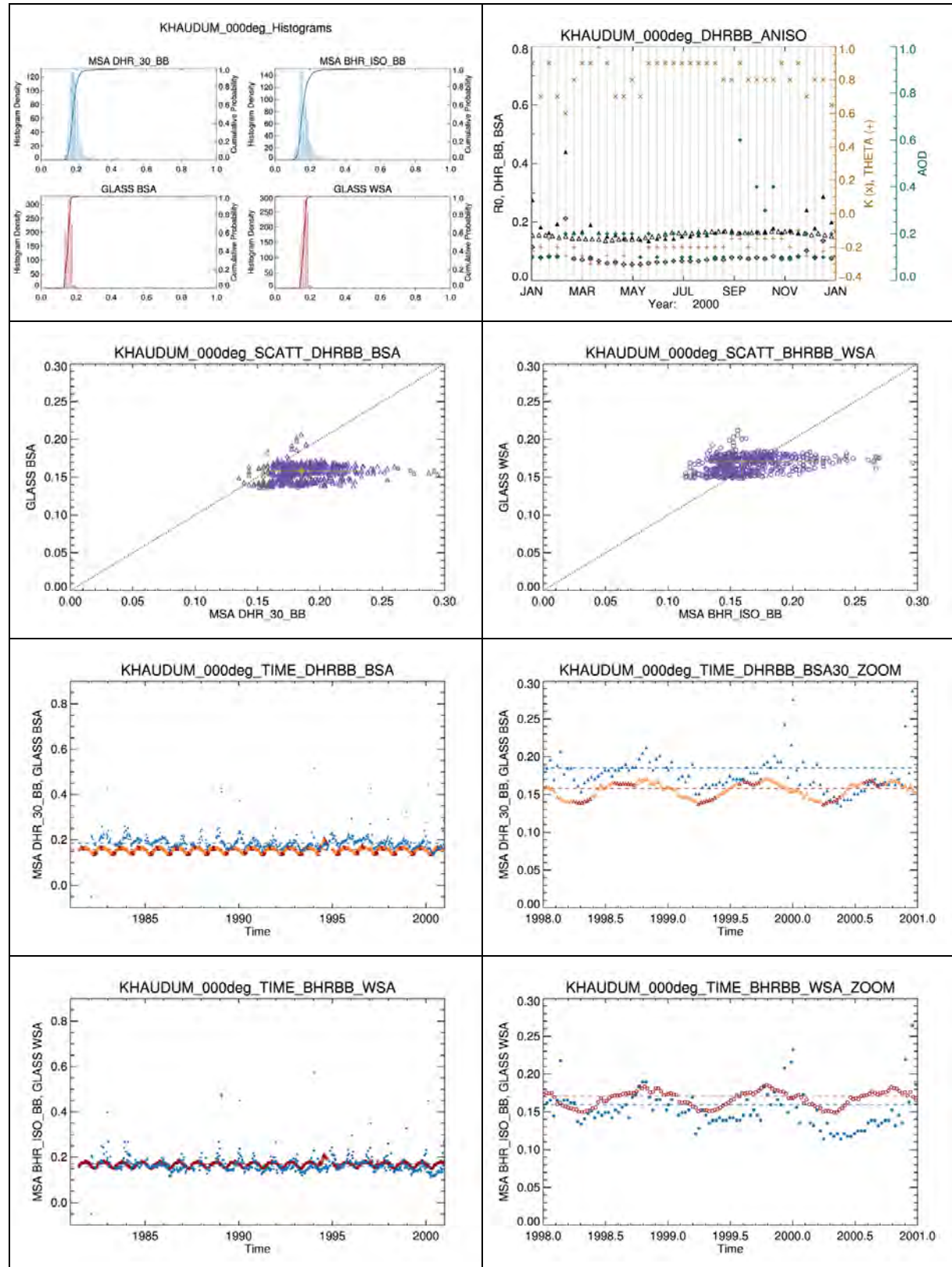
8.6 BOUMBA_BEK – IODC
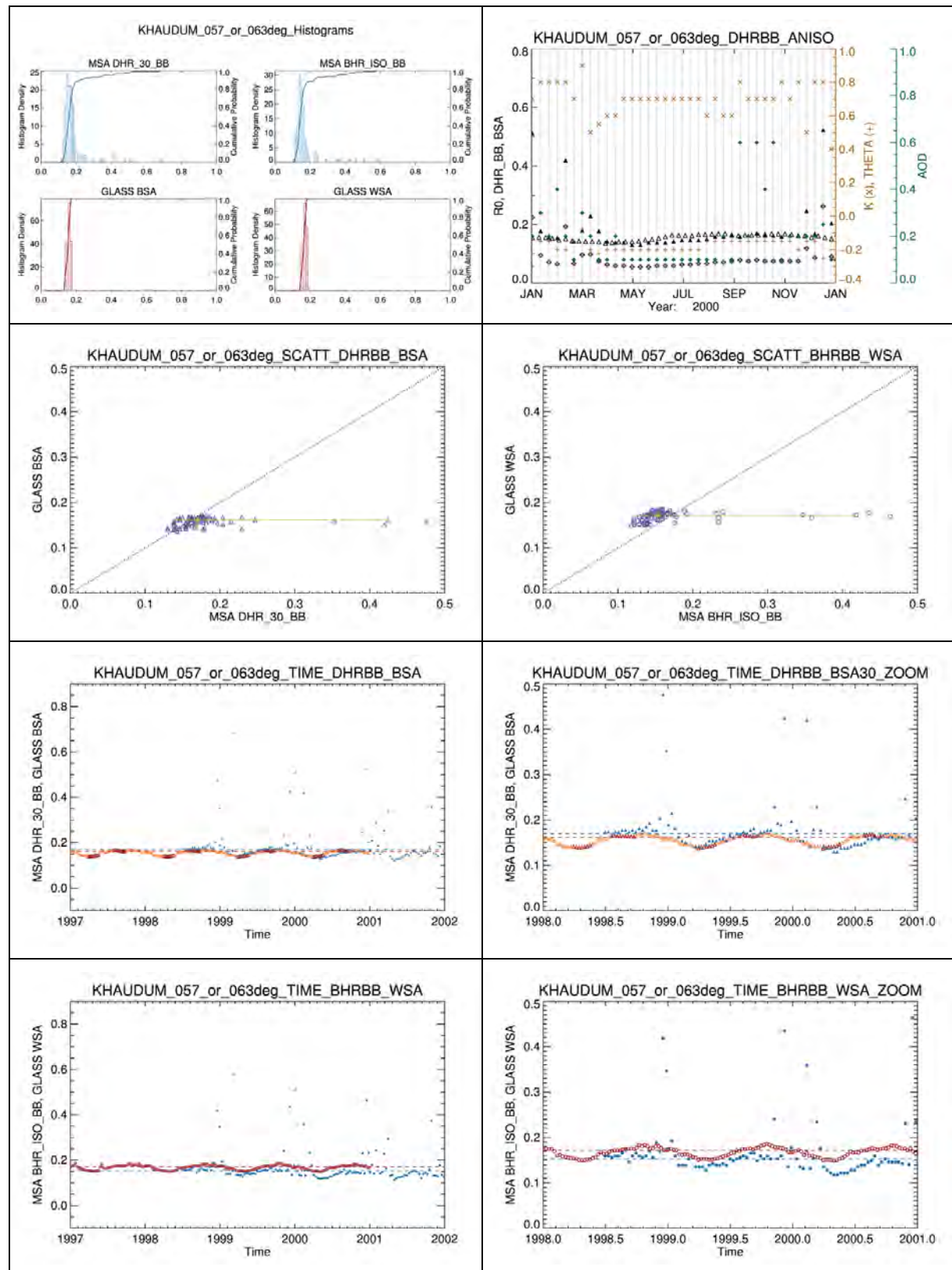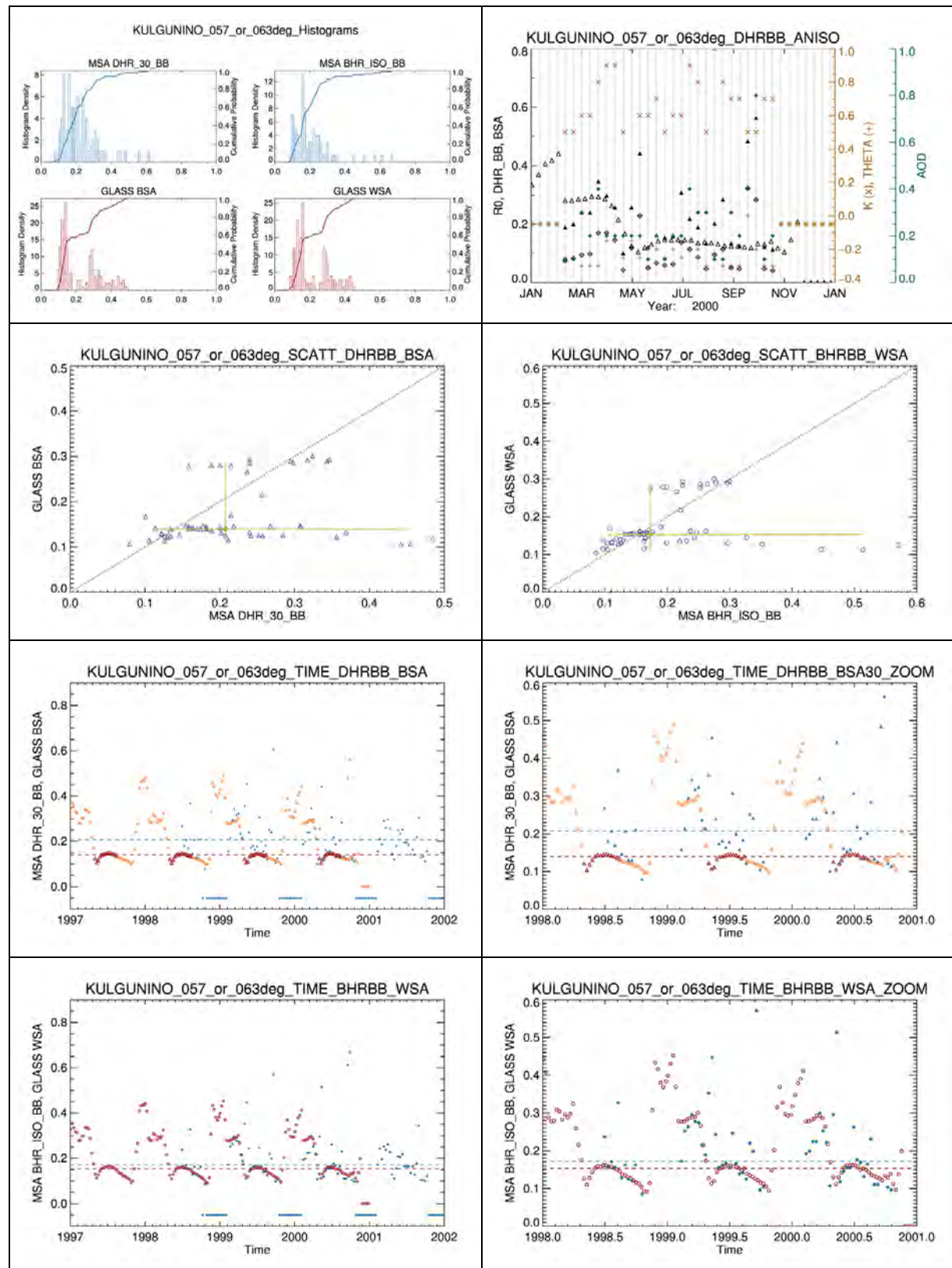
8.7 BRIANSKI_LES – 0DEG
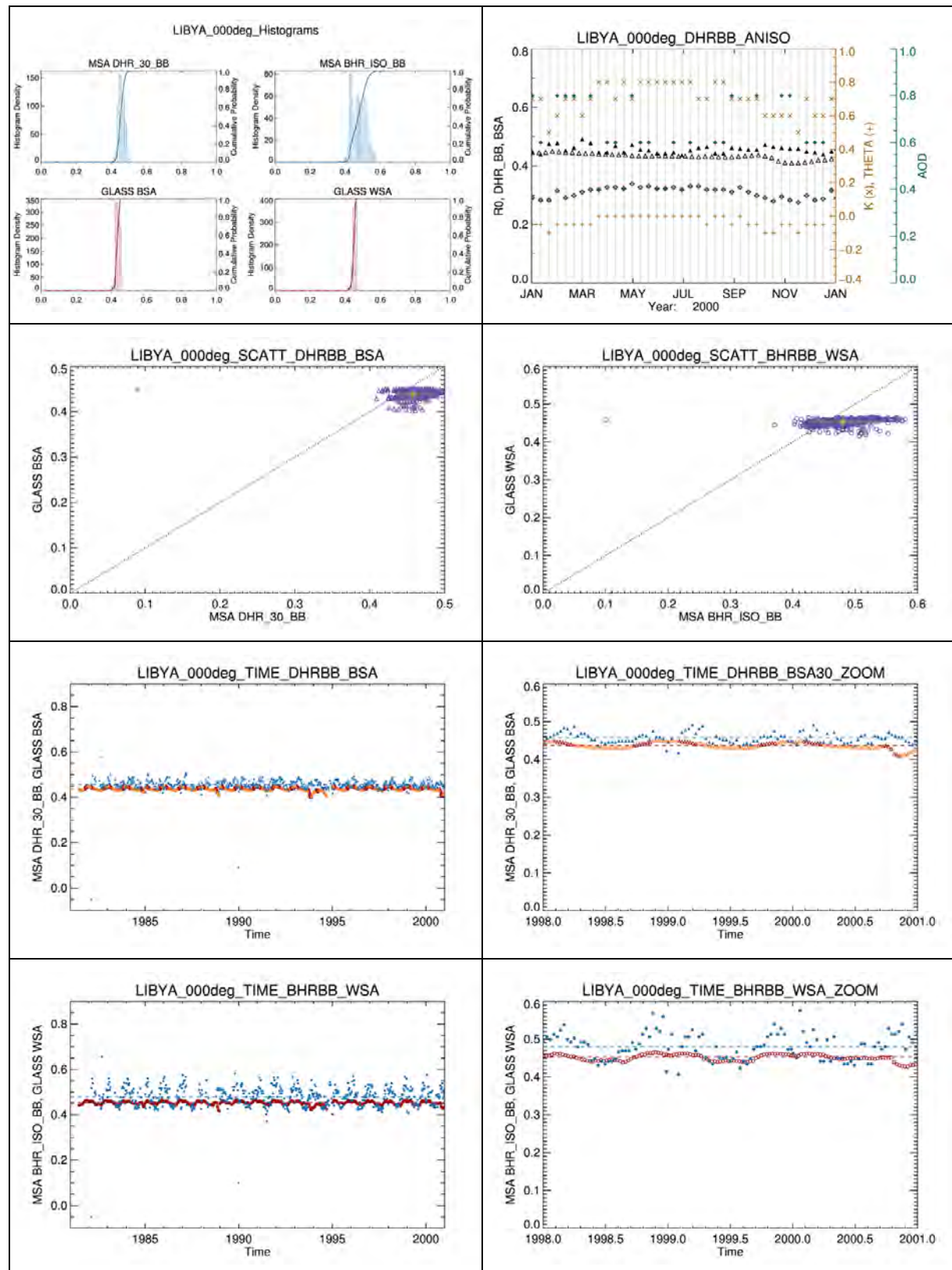
8.8 BRIANSKI_LES – IODC

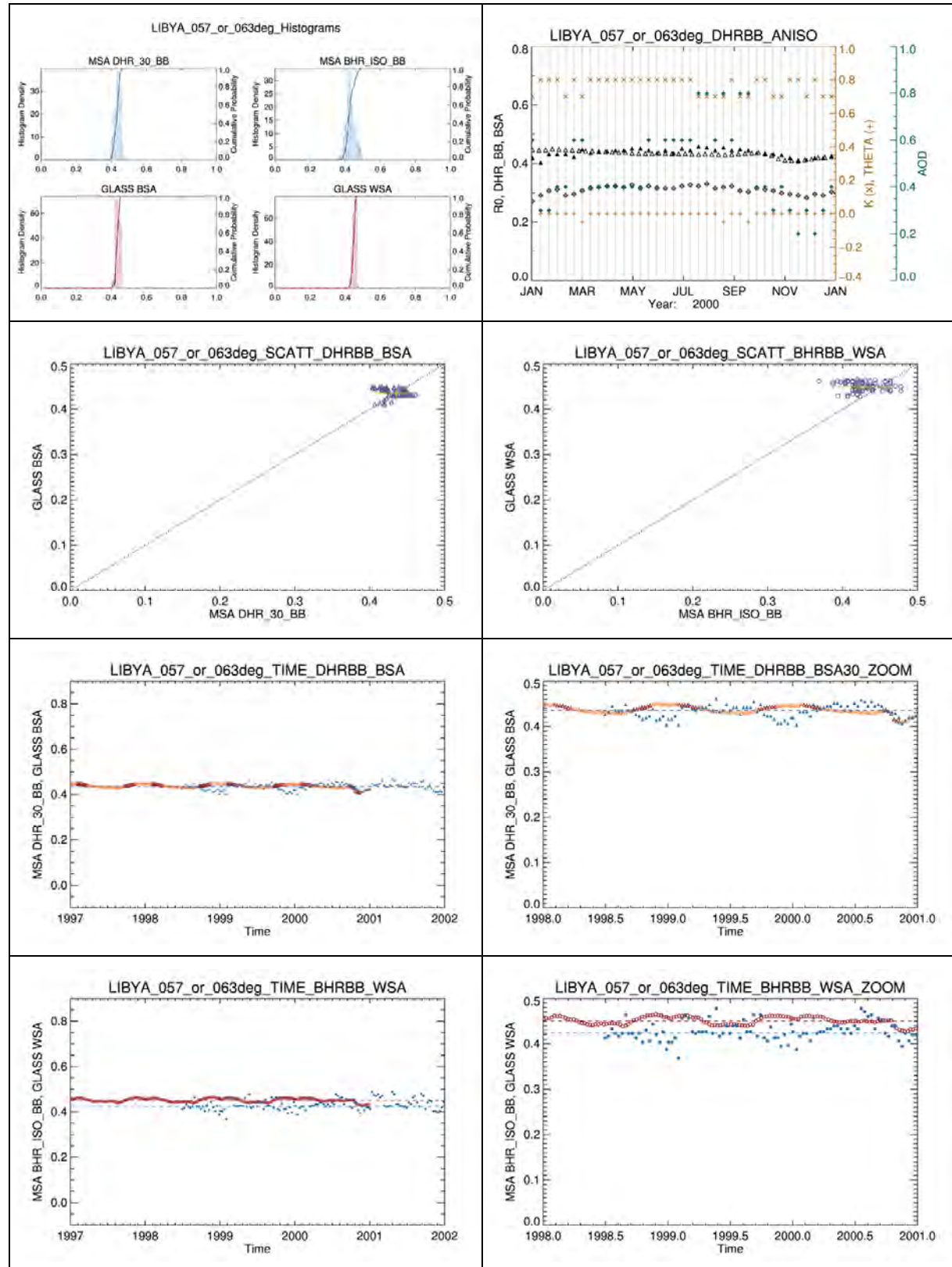## 8.9 KHAUDUM – 0DEG

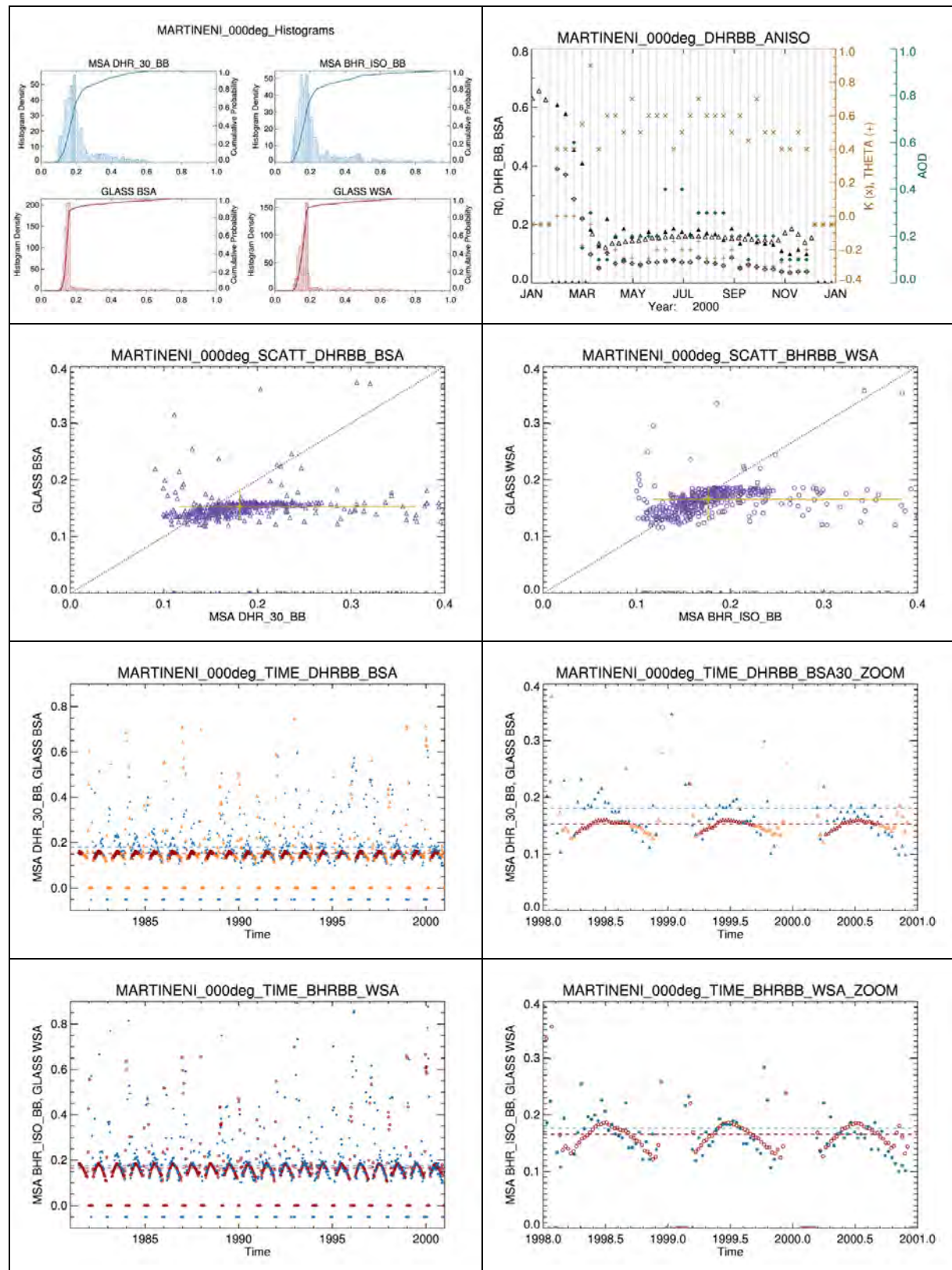## 8.10 KHAUDUM – IODC

8.11 KULGUNINO- IODC
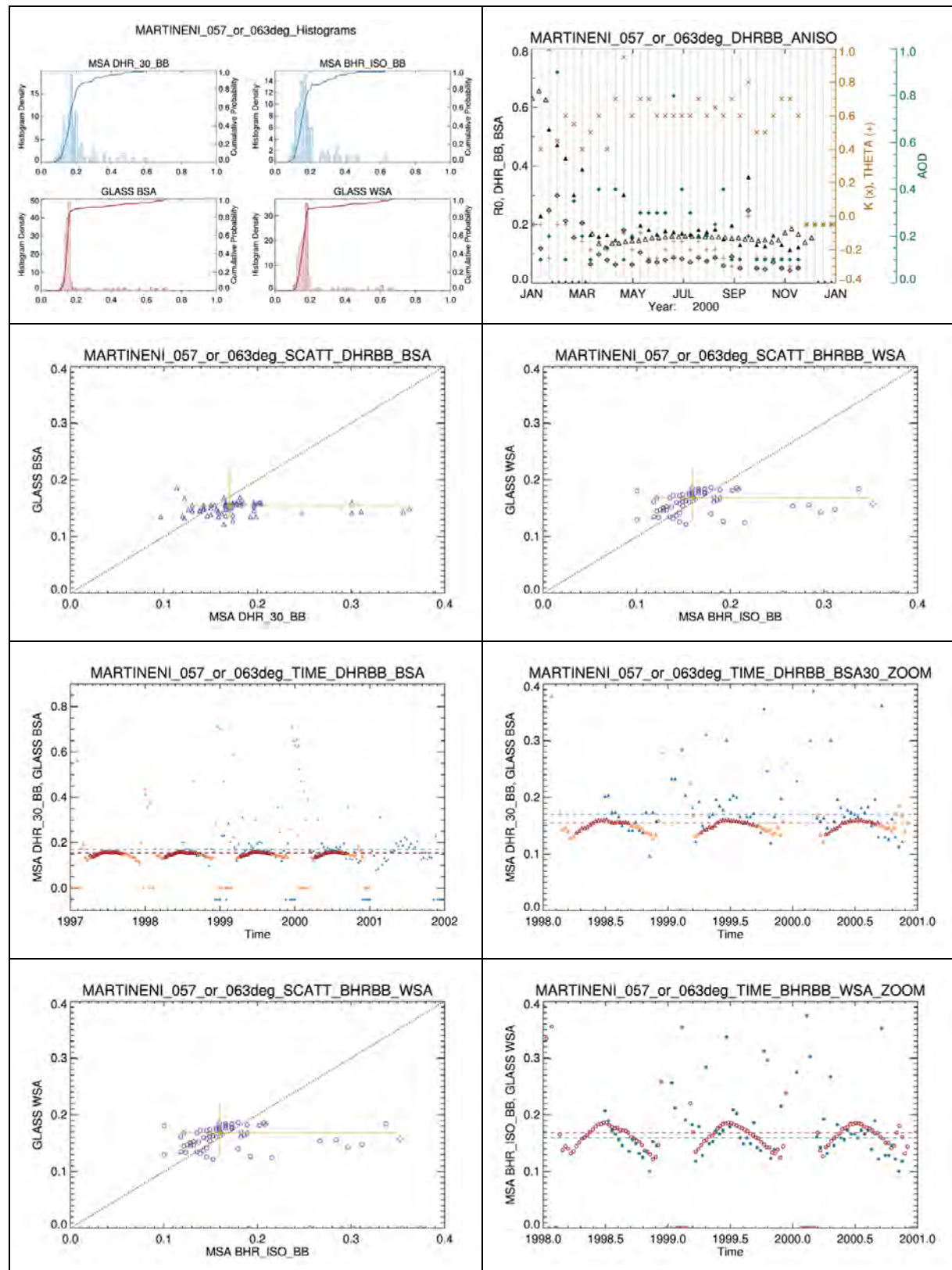
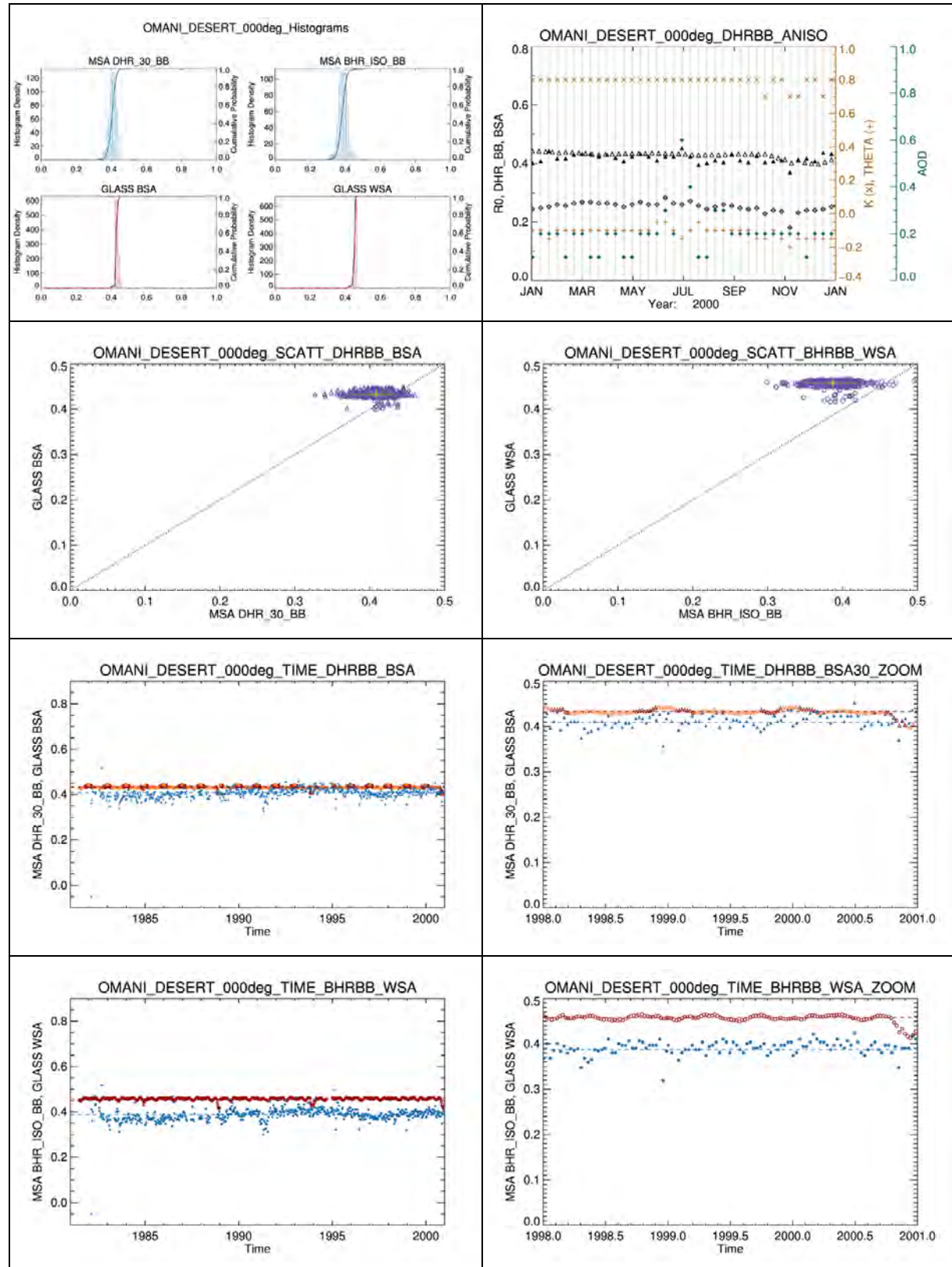## 8.12 LIBYA – 0DEG

8.13 LIBYA – IODC

8.14 MARTINENI – 0DEG

8.15 MARTINENI – IODC

8.16 OMANI_DESERT – 0DEG

8.17 OMANI_DESERT – IODC